MIAMI UNIVERSITY
The Graduate School

Certificate for Approving the Dissertation

We hereby approve the Dissertation

of

Brittany Allison Cymes

Candidate for the Degree

DOCTOR OF PHILOSOPHY

_____
Mark Krekeler, Director

_____
Claire McLeod, Reader

_____
John Rakovan, Reader

_____
Peter Heaney, Reader

_____
Catherine Almquist, Graduate School Representative

ABSTRACT

CATALYTIC PROPERTIES OF NOVEL MICROPOROUS MINERALS

by

Brittany A. Cymes

Modern civilization as we know it today could not exist without heterogeneous catalysis as it underpins all development in applied chemistry, materials science, and environmental geochemistry. Catalysts allow important chemical reactions such as the production of agricultural fertilizer, the formation of petrochemicals, and the breakdown of environmental pollutants to occur with lower energy thresholds. Catalysts comprise a diverse group of materials but none quite as important as porous solids, which optimize surface area, facilitate catalyst recyclability, and impart important selective properties. Many porous materials are naturally occurring minerals such as transition metal oxides, phyllosilicates, zeolites or complex compounds of minerals. This dissertation relates efforts to create and explore novel mineral catalysts whose catalytic properties are directly related to their microporosity, that is, minerals whose pores are less than 2 nanometers in diameter. In the first project, cryptomelane – a manganese oxide with a square tunnel-based framework – was synthesized in the absence and presence of an aqueous growth medium and doped with europium during and after crystallization to investigate Eu's effects on cryptomelane's physical, chemical, and catalytic properties in a temperature-dependent oxidation reaction. It was determined that the position of Eu in the cryptomelane framework strongly affected its catalytic activity. In the second project, sepiolite – a phyllosilicate mineral with a ribbon-like crystal structure and high specific surface area – was modified with manganese and europium prior to in-situ growth and deposition of nanocrystalline titanium dioxide to investigate the effects of support-doping vs. catalyst-doping in a photocatalytic reaction under different ultraviolet radiations. It was determined that phyllosilicate support promoters have variable behavior during multi-step catalyst preparation which ultimately impacted the photocatalytic activity of the primary catalyst. In the third project, cavansite – a phyllosilicate mineral with redox-sensitive vanadium centers in a zeolite-like framework – was investigated for the first time as a catalyst and also for the first time using electron microscopy. It was determined that cavansite may have selective activity for selective partial oxidation of ethanol at elevated temperatures. In addition, unreported cleavage planes were resolved using scanning electron microscopy in two perpendicular directions.

CATALYTIC PROPERTIES OF NOVEL MICROPOROUS MINERALS

A DISSERTATION

Presented to the Faculty of

Miami University in partial

fulfillment of the requirements

for the degree of

Doctor of Philosophy

Department of Geology and Environmental Earth Science

by

Brittany A. Cymes

The Graduate School
Miami University
Oxford, Ohio

2020

Dissertation Director: Mark P.S. Krekeler, Ph.D.

TABLE OF CONTENTS

iv

LIST OF TABLES

LIST OF FIGURES

Chapter 4. Investigation of the catalytic properties of cavansite, a naturally-occurring microporous vanadosilicate, and characterization using electron microscopy

DEDICATION

To Amelia. There are not enough cat treats in the world to repay you for being my steadfast companion along this journey.

ACKNOWLEDGEMENTS

CHAPTER 1

INTRODUCTION

1. Heterogeneous catalysis

Heterogeneous catalysis has underpinned the development of modern civilization as we know it today. It is responsible for important advances such as the production of ammonia for use in fertilizers (the Haber-Bosch process), the production of useful fuels and intermediate chemicals from synthetic gas (Fischer-Tropsch chemistry), and the abatement of combustion engine emissions (three-way catalysis). Heterogeneous catalysts affect the kinetic parameters of a chemical reaction by lowering the position of energy barriers while leaving the properties of the equilibrated state unaltered. Ultimately, they facilitate greater reaction efficiency, saving energy and time – and they perform this function while remaining unconsumed.

 "Heterogeneous" refers to the catalyst existing in a different phase of matter than the reactants. Typically, the catalyst is a solid and the reactants exist in the liquid or gaseous phase. These catalysts make up the majority of those used in industrial settings. Heterogeneous catalysts not only increase the rate of a reaction, but they perform this task selectively, meaning that only desired reactions are sped up rather than every possible reaction. This property is known as *selectivity* and it is a powerful driver behind continual research and development of new catalysts. Selectivity is the reason why the same reactants will yield different products over different catalysts and why catalysis is such an experimentally-driven field; the products of a given reaction over a catalyst are virtually impossible to model without empirical testing.

Heterogeneous interactions ultimately occur at the interface between two different phases. The bonding characteristics of atoms at the surface of a solid are different than those within the bulk and, naturally, these regions have different properties. Surface atoms simply cannot satisfy all of their bonding requirements in the same way as internal atoms and therefore will always react in some way with matter at the interface. Adsorption to the catalyst surface is an essential step in heterogeneous reactions. There are two main types of adsorption interactions: physisorption and chemisorption. In physisorption, weak interactions involving polarization of adsorbates and the surface dominate; these interactions occur without electron transfer. In chemisorption, strong chemical bonds form between the adsorbate and the surface and reactions occur subsequently. In reality, most processes occur by a combination of these two adsorption interactions.

The most common catalytic mechanisms which utilize these adsorption interactions are (1) the Langmuir-Hinshelwood mechanism, (2) the Eley-Rideal mechanism, and (3) the Mars and Van Krevelen mechanism. In the Langmuir-Hinshelwood (L-H) mechanism, reactants adsorb onto the catalyst surface, interact with the surface and each other, and desorb as products. The limiting factor in L-H mechanics is active site availability as reactants must compete for the same sites. In Eley-Rideal mechanics, only one reactant adsorbs onto the catalyst surface, this species reacts with the surface to form an intermediate species which then interacts with the unbonded reactant species to form the surface-held product, which subsequently desorbs; in this reaction there is no site competition. Finally, in the Mars and Van Krevelen (MVK) mechanism, reactants adsorb onto different active sites, forming intermediate products which then interact to form the products, which desorb from the surface; again, there is no active site competition. It is the goal of the researcher to determine which mechanism describes the empirical observations of the reaction and derive the appropriate performance equations. However, once again the reality is that the solution is likely to be a combination of different mechanisms. It is therefore unsurprising that convention in the field of catalysis is to determine the model that *best* fits the experimental data.

Catalytically active materials are as diverse as the chemical reactions they assist. Within heterogeneous catalysts, common materials are multifunctional solids (e.g. zeolites, graphene, and nanoparticles), transition metals and their oxides and sulfides, noble metals, and lanthanide elements. Anatomically, catalysts are not simply comprised of the active material; often, they also consist of supports and promoters. The purpose of a support is to maximize accessibility of catalyst surface to reactants by holding dispersed catalyst particles on its high surface area. Supports can also aid in catalyst recovery efforts, particularly in solid-liquid systems where catalyst particles are extremely small. The role of a promoter (also referred to as a dopant or a co-catalyst) is to assist the catalyst *or* support to perform their functions. Catalyst dopants introduced during synthesis can (1) impact the crystalline structure by introducing defects so as to increase active site density, (2) place limitations on crystal growth so as to control particle size and increase surface area, or (3) introduce exotic reactive ions which can act as charge reservoirs during electron transfer reactions or perform charge-carrier separation, among other functions. Support dopants can help prevent the agglomeration of dispersed catalyst particles and also they can provide catalytic functionality so that the support can act as a 'back-up' to the catalyst.

2.   Research and development in catalysis

Catalysts serve our ever-evolving needs as a society and as a result there is continual innovation within the field. A crucial aspect of developing novel catalytic materials is characterization. Understanding the physical and chemical properties of a new material is key to understanding what mechanisms are occurring at each step of a given reaction for which it is designed. Consider the major steps of a catalytic reaction: (1) the reactants must be transported from the bulk phase to the catalyst surface, (2) those reactants must adsorb onto the catalyst surface, (3) the chemical reaction must occur, (4) the products must desorb from the catalyst surface, and (5) the products must be transported back to the bulk phase. These steps require many simultaneous considerations with respect to catalyst and reaction design.

The morphology of a catalyst has a strong influence on the bulk mass transport of reactants to and from the catalyst. Microscopy techniques such as scanning electron microscopy (SEM) and transmission electron microscopy (TEM) allow for detailed characterization of catalyst morphology. As many catalysts exist as, or are combined with, porous structures, the geometric surface area and pore geometry must also be evaluated. Porosity also influences bulk transport of reactants as these must diffuse through the solid phase to reach active sites – techniques such as nitrogen porosimetry and mercury intrusion allow for the determination of these surface properties. Other physical property determinations must be made, including particle size distribution and catalyst dispersion, in order to fully evaluate the interaction of reactants with the catalyst surface – again, using microscopy techniques or sieving in the former case.

Once reactants reach the catalyst surface, the chemical nature of the catalyst becomes crucial and this will affect adsorption, bonding characteristics, and in some cases the activity necessary to drive the reaction forward (e.g. oxidation reactions). Chemistry can be determined by a variety of bulk analytical techniques; however, sensitivity is important, particularly with dopants which are often present in concentrations less than 0.1%. Techniques such as inductively-coupled plasma optical emission spectrometry (ICP-OES), wavelength dispersive spectroscopy (WDS), or energy dispersive spectroscopy (EDS) are routinely used for this purpose. In addition to bulk chemistry, often in redox reactions the nature of the oxidation state of active transition metals is of interest, and so techniques like electron energy loss spectroscopy (EELS) or X-ray absorption near edge structure (XANES) are used.

Other considerations include the kinetic requirements of the reaction, such as the need for elevated temperatures or specific irradiation. Thermogravimetric analysis (TGA) is used to evaluate the thermal stability of a material so that its ability to withstand reaction conditions can be determined. A wide array of spectroscopic techniques – ultraviolet, visible, infrared, Raman, and X-ray to name a few – are used to determine how materials interact with incident irradiation. These data can be used as indicators of the physical structure of a material, for identifying optical characteristics of specific properties, or as reaction requirements (e.g. photocatalysis). Another property that is often evaluated is the crystalline structure of the catalyst and this is routinely done using X-ray or electron diffraction techniques.

3.   The role of minerals in catalysis

Catalyst research and development is a perennially active area of research. The sky is truly the limit in manufacturing novel catalysts; although completely original materials continue to surface, more often than not, progress is driven by variations of existing material by direct alteration or exotic combinations; and as mentioned above, selectivity is always of interest. A continual source of inspiration and motivation for new catalysts is the natural world; indeed, naturally-occurring minerals are involved in many aspects of modern catalysis (Rocha and Lin, 2005). Traditional mineral catalysts include noble metals (e.g. platinum) and metal oxides (e.g. anatase or TiO_2). Common catalyst support minerals include phyllosilicates (e.g. kaolinite) and zeolites (natrolite). These minerals are very often hybridized and/or modified either through alteration of the naturally occurring material (e.g. clay pillaring) or through primary synthesis (e.g. cerium-doped birnessite).

In addition to altering known minerals, naturally-occurring mineral species are continually being assessed as novel catalytic materials. With the immense variety of industrial chemical reactions in demand of catalysts, diverse mineral groups continue to be explored such as: dolomite and hydroxyapatite as a base catalysts in Knoevenagel reactions (Tamaddon et al., 2013; Sebti et al., 2002) and transesterification reactions (Wilson et al., 2008), natural pyrite and tourmaline as oxidation catalysts in Fenton process reactions (Labiadh et al., 2015; Xu et al., 2009), and magnetic sphalerite as a visible-light photocatalyst (Xia et al., 2013).

4.   Porous mineral catalysts

The International Union of Pure and Applied Chemistry (IUPAC) divides porous materials into macroporous materials which have pores greater than 50 nm in diameter, mesoporous materials which have pores between 2 and 50 nm in diameter, and microporous materials which have pores less than 2 nm in diameter. This dissertation is concerned with mineral-based catalysts with a functional microporosity, that is, minerals whose porosity <2 nm is a key component of their functionality as a catalyst. Porosity can help to disperse a catalyst but it can also impact selectivity. Indeed, selectivity is the hallmark of porous catalysts as they can allow certain reactants to reach active sites while excluding unwanted components. Major mineral groups that fall into the microporous category include zeolites, phyllosilicates, and some metal oxides. Porous catalysts used in commercial settings are often complex mixtures or composites with various components used for different purposes like dispersion, secondary activity, promotion, and inhibition (Suib et al., 2020) and therefore the catalytic activities of these materials could be a function of many aspects of the physical catalyst. The sheer multitude, variety, and complexity of porous catalysts cannot be stressed enough.

Aspects that are often identified in a porous catalyst and used for classification are the global atomic coordination environment, the nature of the bonding types represented, and the directionality of the bond environments. The purpose of identifying these characteristics is to understand where activity occurs on a catalyst surface. Isotropic catalytic activity is uncommon; in many cases reactions occur only along specific directions of a catalyst because electrons transfer more readily or bonding is less satisfied along a given direction. For example, in phyllosilicates, electrons transfer is more kinetically favored laterally within layers than normal to the layers. This concept is quite intuitive as it echoes many of the fundamentals of electronic circuitry. In this dissertation, I consider (1) an octahedral molecular sieve mineral built up entirely of octahedrally-coordinated metal atoms arranged in a 3D framework with 3D covalent bonds, (2) a modulated phyllosilicate mineral built up of octahedrally- and tetrahedrally-coordinated atoms arranged in a 3D framework with 2D covalent bonding, and (3) a zeotype mineral built up of octahedrally-, pentahedrally-, and tetrahedrally-coordinated metal atoms arranged in a 3D framework with 3D covalent bonding.

5.   Catalytic properties of novel microporous minerals

In this dissertation, three aspects of microporous minerals are investigated with respect to heterogeneous catalysis and novel material development: (1) the impact of different methods of direct modification of an unsupported active mineral on its oxidative catalytic properties; (2) the impact of substrate-modification on the activity of a nanocomposite photocatalyst; and (3) an ab-initio exploration of the oxidative catalytic properties of a suspected active mineral.

The first project is on the synthesis, characterization, and catalytic properties of europium doped cryptomelane. The mineral cryptomelane is a well-recognized catalytically-active material due to its having a high surface area, exchangeable tunnel cations, and labile lattice oxygen. The addition of europium is a novel undertaking and was done so by multiple routes with a variety of physical, chemical, and catalytic results. The main finding of this study was the synthesis method has a strong control on europium-incorporation geometry and subsequent catalytic performance, for in only one method was the dopant suspected to have occupied a framework site instead of a tunnel site, thereby contributing to electron transfer across the framework globally in a model oxidation reaction.

In the second project, the magnesium phyllosilicate mineral sepiolite is investigated as a promoted support for an anatase titania photocatalyst in an aqueous organic dye degradation reaction. In this project, sepiolite was cation-exchanged with Mn^{2+} and Eu^{3+} in an attempt to influence the electronic behavior of the titania phase with which it was nanocomposited. Nanocompositing refers to the in situ growth of the catalyst on a support and they therefore coexist in intimate adjacency so as to consider the former of potentially having the ability to electronically influence or be influenced by the latter. In this study, I demonstrated that phyllosilicate support promoters can have variable behavior during a multi-step catalyst preparation which impacted the ability of the primary catalyst to perform under ultraviolet irradiation activation.

In the final project, the vanadium phyllosilicate mineral cavansite is investigated. Cavansite, along with its dimorph, pentagonite, represent the only known naturally occurring vanadosilicate minerals. Vanadosilicate materials were intensely developed during the 1990's and early 2000's for eventual use in catalysis; however, efforts slowed and none of the materials underwent empirical testing as catalysts. In this investigation, I undertook the first electron microscopy investigation of cavansite as well as performed initial catalytic evaluation of the

7

material in a volatile organic compound oxidation reaction. The results of the latter indicate that cavansite may have selective activity for partial oxidation of ethanol at elevated temperatures as well as previously unrecognized microscopic characteristics.

References

Labiadh, L., Oturan, M. A., Panizza, M., Hamadi, N. B., & Ammar, S. (2015). Complete removal of AHPS synthetic dye from water using new electro-fenton oxidation catalyzed by natural pyrite as heterogeneous catalyst. *Journal of hazardous materials*, *297*, 34-41.

Rocha, J., and Lin, Z. (2005). Microporous mixed octahedral-pentahedral-tetrahedral framework silicates. Reviews in Mineralogy and Geochemistry, 57, 173-201.

Sebti, S., Tahir, R., Nazih, R., Saber, A., & Boulaajaj, S. (2002). Hydroxyapatite as a new solid support for the Knoevenagel reaction in heterogeneous media without solvent. *Applied Catalysis A: General*, *228*(1-2), 155-159.

Suib, S.L., Prech, J., Cejka, J., Kuwahara, Y., Mori, K., and Hiromi, Y. (2020) Some novel porous materials for selective catalytic oxidations. Materials Today, 32, 244-259.

Tamaddon, F., Tayefi, M., Hosseini, E., & Zare, E. (2013). Dolomite (CaMg (CO3) 2) as a recyclable natural catalyst in Henry, Knoevenagel, and Michael reactions. *Journal of Molecular Catalysis A: Chemical*, *366*, 36-42.

Wilson, K., Hardacre, C., Lee, A. F., Montero, J. M., & Shellard, L. (2008). The application of calcined natural dolomitic rock as a solid base catalyst in triglyceride transesterification for biodiesel synthesis. *Green chemistry*, *10*(6), 654-659.

Xia, D., Ng, T. W., An, T., Li, G., Li, Y., Yip, H. Y., ... & Wong, P. K. (2013). A recyclable mineral catalyst for visible-light-driven photocatalytic inactivation of bacteria: natural magnetic sphalerite. *Environmental science & technology*, *47*(19), 11166-11173.

Xu, H. Y., Prasad, M., & Liu, Y. (2009). Schorl: A novel catalyst in mineral-catalyzed Fenton-like system for dyeing wastewater discoloration. *Journal of Hazardous Materials*, *165*(1-3), 1186-1192.

CHAPTER 2

EUROPIUM-DOPED CRYPTOMELANE: MULTI-PATHWAY SYNTHESIS, CHARACTERIZATION, AND EVALUATION FOR THE GAS PHASE CATALYTIC OXIDATION OF ETHANOL

1.   Introduction

Cryptomelane is a multivalent, tunnel-structured manganese oxide mineral and 2×2 octahedral molecular sieve (OMS-2) possessing high activity as a catalyst for the abatement of volatile organic compounds (VOCs) such as benzene [1-3], cyclohexane [4-5]; toluene [6-7], ethyl acetate [8-10], and ethanol [11-12]. Cryptomelane's catalytic activity in VOC degradation is largely a function of its high surface area, exchangeable tunnel cations, and mobile and reversible lattice oxygen. In addition to its significant catalytic activity, cryptomelane is a cost-friendly option compared to traditional noble metal-based catalysts. Cryptomelane occurs in a wide variety of geologic environments [13] and is readily synthesized in the lab [14-17]. The general chemical formula for cryptomelane is $K(Mn^{2+}Mn^{4+})_8O_{16}$.

Cryptomelane has been modified extensively with transition metals such as Fe, Co, Ni, Cu, V and Cr [18-24], noble metals such as Pt and Ag [3, 25] and lanthanides such as Ce [26-28] for the purposes of further improving its catalytic activity. Lanthanide group elements like Ce are commonly used in catalysis owing to their high charges, large ionic radii, variable coordination geometry, low electronegativity, and oxophilicity. Europium (Eu^{2+}/Eu^{3+}), another lanthanide group element, has been used as a dopant in VOC degradation over metal oxide catalysts such as TiO_2 for photocatalytic oxidation of rhodamine B and methylene blue [29-30] and $BiVO_4$ for photocatalytic oxidation of methyl orange [31] as well as Pt for electro-oxidation of ethanol [32-33]. In these studies, catalytic activity improvement is shown to be highly dependent upon the preparation method and the distribution of Eu in or on the catalyst.

To date, no investigations of a Eu-modified cryptomelane have been reported. Impetus for attempting Eu-doped cryptomelane stems from studies showing that Ce promotes cryptomelane with respect to thermal stability, catalytic activity, surface area, and pore volume [5, 26-27, 34]. Ce has also been shown to shift the average oxidation state (AOS) of cryptomelane higher or lower dependent upon the synthesis method [34-35]. Cryptomelane AOS manipulation is of interest in VOC degradation as the availability of lattice oxygen in the MnO_6 groups is crucial to catalytic activity.

In order to have a thorough understanding of how Eu affects cryptomelane, this study explored Eu-doping via co-precipitation where Eu was present during crystallization and via ion-exchange, where pre-formed cryptomelane was exposed to a Eu-salt solution. In addition to different Eu-doping methods, two different cryptomelane synthesis methods were explored here

11

due to observed differences in selective oxidation activity as a function of morphology [36]. Here, we made cryptomelane by the reflux method, typified by long, slender nanofibers [14] and by the solvent-free method, characterized by short nanorods [17].

2. Experimental

2.1 Catalyst preparation

Cryptomelane was prepared by the solid state method and the reflux method. Each variety was doped with europium via either co-precipitation or ion exchange. Non-promoted controls for both solid-state and reflux cryptomelane were also produced. The details of each preparation are provided below.

2.1.1 Solid-state method

The protocol for producing the control solid-state cryptomelane (designated SS-CON) was adapted from Ding et al. [17]. Manganese (II) acetate ($Mn(CH_3CO_2)_2 \cdot 4H_2O$) (ACROS Organics) and potassium permanganate ($KMnO_4$) (Fisher Chemical) powders in a 3:2 molar ratio (22.05 g (90 mmoles) of Mn-acetate and 9.48 g (60 mmoles) of K-permanganate) were mixed and ground together in an agate mortar and pestle for 30 minutes until a uniform gray-lavender color was achieved. The resulting mixture was then placed in a capped glass bottle and maintained at 80 °C for 4 hours. The resulting black product was washed several times with deionized water to remove any remaining ions and dried in air at 80 °C in an uncapped bottle overnight. The product was calcined in air at 450 °C for 2 hours (100 °C/hour ramp and 2 hour dwell).

Solid-state Eu-doped cryptomelane was produced via co-precipitation (designated SS-CP) following methodology adapted from Wu et al. [37] who produced Ce-doped cryptomelane. Europium (III) acetate ($Eu(CH_3COO)_3 \cdot xH_2O$) powder (Alfa Aesar) was added to Mn-acetate and K-permanganate in a 0.5:3:2 molar ratio (2.47 g Eu-acetate, 11.025 g Mn-acetate, and 4.74 g K-permanganate). The powders were mixed and ground together in an agate mortar and pestle for 30 minutes until a uniform gray-lavender color. The resulting mixture was then placed in a capped glass bottle and maintained at 80 °C for 4 hours. The resulting black product was washed several times with deionized water to remove any remaining ions and dried in air at 80 °C in an uncapped bottle overnight. The product was calcined in air at 450 °C for 2 hours (100 °C/hour ramp and 2 hour dwell).

The protocol for ion exchange used here follows previous work in Ce-doped cryptomelane. Abecassis-Wolfovich et al. [26] and Jothiramalingam et al. [38] doped cryptomelane with 0.25 M and 0.2 M cerium(III) nitrate, respectfully, with improvement in surface area and no detectable free ceria phase present, indicating successful structural incorporation of Ce. Hapeshi and Theocharis et al. [27] tested 0.01 M, 0.1 M, and 0.5 M cerium(III) nitrate and found that 0.01 M and 0.5 M decreased specific surface area whereas 0.1 M increased surface area. In light of these studies, Eu-doped cryptomelane was produced via ion-exchange (designated SS-IE) by first producing SS-CON as above and then suspending uncalcined material in a 0.25 M aqueous solution of europium(III) nitrate ($Eu(NO_3)_3 \cdot 6H_2O$) (Alfa Aesar) at room temperature for one 24-hour cycle and one 96 hour cycle under gentle stirring with intermediate separation of the solid via centrifuging and refreshment the Eu-nitrate solution before each cycle. SS-IE was then filtered and washed with deionized water several times and dried overnight at 80 °C. The product was calcined in air at 450 °C for 2 hours (100 °C/hour ramp and 2 hour dwell).

2.1.2   *Reflux method*

The reflux method cryptomelane (designated R-CON) was adapted from Luo et al. [1], Frias et al. 39], Valente et al. [40], and Almquist et al. [41]. For this preparation, 11 g of Mn-acetate was dissolved in 40 mL of deionized water and 5 mL of glacial acetic acid was added – this solution was brought to 90 °C under stirring in a round-bottomed flask affixed with a reflux condenser. 6.5 g of K-permanganate was dissolved in 150 mL of deionized water and slowly (dropwise) added to the Mn-acetate solution. The solution was maintained at 90 °C for 24 hours – the flask was suspended in a circulating water bath to ensure even-heating. The resulting precipitate was filtered, washed several times with deionized water, air-dried overnight at 80 °C, and finally calcined at 450°C for 2 hours.

The method for reflux Eu-doped cryptomelane produced via co-precipitation (designated R-CP) was adapted from Ma et al. [35] and Kilmartin et al. [42] who produced Ce cryptomelane. A solution of 1.737 g Eu-nitrate dissolved in 45 mL of deionized water was added to a solution of 11 g of Mn-acetate dissolved in 60 mL of deionized water. 7.5 mL of glacial acetic acid was added to this solution. A solution of 6.5 g of K-permanganate dissolved in 120 mL of deionized water was prepared and added to the mixture. This solution was maintained at 90 °C under

refluxing conditions for 24 hours. The resulting precipitate was filtered, washed several times with deionized water, dried in air at 80 °C overnight, and finally calcined at 450°C for 2 hours.

Reflux Eu-doped cryptomelane was produced via ion-exchange (designated R-IE) by the same method as was done for the SS-IE using a Eu-nitrate solution, on R-CON produced via the method detailed above. R-CON was treated in 0.25 M aqueous solution of europium (III) nitrate (Alfa Aesar) ($Eu(NO_3)_3 \cdot 6H_2O$) at room temperature for one 24-hour cycle and one 96 hour cycle under gentle stirring with intermediate separation of the solid and refreshment of the Eu-nitrate each cycle. R-IE was filtered and washed with deionized water several times and dried overnight in air at 80 °C, and finally calcined at 450°C for 2 hours.

2.2   Catalyst characterization

The crystal structure of the cryptomelane samples was characterized by X-ray diffraction (XRD), the nanoscale surface morphology and atomic structure were explored by scanning and transmission electron microscopies (SEM and TEM), the chemical composition and Mn/Eu oxidation states were respectively evaluated by X-ray energy dispersive spectroscopy (XEDS) and electron energy loss spectroscopy (EELS), the BET surface area and BJH pore size distribution were characterized by nitrogen adsorption, and the thermal stability was determined by thermogravimetric analysis (TGA). Each technique is described below.

2.2.1   Powder X-ray diffraction

XRD patterns were collected using a Scintag Pad X powder diffractometer to determine the crystal structure of the samples. The sample powders were mounted onto zero-background slides and analyzed in the 2θ range 2-65° in 0.02° steps with a 5.0 s dwell time using monochromated Cu radiation (1.5418 Å) equipped with a Peltier detector, operating at 40 kV and 35 mA.

2.2.2   Scanning electron microscopy (SEM) and energy-dispersive X-ray spectroscopy (XEDS)

The surface morphology of the samples was examined using a Zeiss Supra 35 VP scanning electron microscope (SEM) with a Schottky field emission source, equipped with a Bruker Quantax 100 energy dispersive X-ray microanalysis system and operated at 2.0 keV for imaging and 20 keV for XEDS. Samples for SEM were prepared as powders dispersed onto carbon tab-covered aluminum stubs and were not coated. Bruker Esprit v.2.1 software was used

for standardless quantification by the P/B-ZAF method and the Phi(Rho,Z) method for energies <1 keV; overlapping Mn-$K_{\alpha1}$ and Eu-$L_{\alpha1}$ peaks were resolved by application of a series deconvolution function.

2.2.3   Transmission electron microscopy (TEM) and electron energy loss spectroscopy (EELS)

The nature of the atomic structure and oxidation states were examined using a JEOL JEM-2100 scanning transmission electron microscope (TEM/STEM) operated in brightfield at 200 keV with a LaB_6 source and equipped with a Gatan Orius SC200D camera and a Gatan GIF Tridiem 863 post-column energy filter EELS/EFTEM system with an UltraScan FT camera. Samples for HR-TEM/EELS were prepared via particulate suspension applications to 3.0 mm lacey carbon-coated copper grids.

The chemical shift method was used to discriminate between the different Mn_xO_y species in the EELS data; this method and others are summarized in Tan et al. [43]. As an additional measurement, the spin-orbital splitting was calculated because a positive correlation has been demonstrated between ΔE and oxidation state [44]. The 'white-line ratio method', which compares $L_{3,2}$ intensities, was not suitable for this investigation due to the particulate-style sample preparation, in which differences in effective thickness and crystallographic orientation introduce differences in inelastic mean free path and electron channeling, respectively. The position of the Mn-L_3 ($2p_{3/2} \rightarrow 3d$) and Mn-L_2 ($2p_{1/2} \rightarrow 3d$) excitation peaks were measured at peak maxima as well as used in the calculation of ΔE(Mn-L_2-L_3).

Spectra for each sample were collected in the range of 0-350 eV zero-loss (ZLP) and 450-800 eV core-loss (ELNES) range. The ELNES spectrum was spliced with the ZLP spectrum and deconvoluted using a Fourier ratio function to remove plural scattering effects. A low-pass numerical filter was utilized to improve signal-to-noise ratio. Mn-$L_{2,3}$ onset energy is linearly related to the oxidation state of Mn; this is a relationship found throughout the transition metals [43]. Cryptomelane is fundamentally defined as having a mixture of divalent, trivalent, and tetravalent manganese. It has been noted by several authors that without prior knowledge, it is very difficult to discriminate between a mixture of $Mn^{2+/4+}$ and Mn^{3+} or a mixture of multiple unknown oxidation states [45-47] and this feat is particularly challenging in inhomogeneous materials such as minerals due to overlap in the direction of the fast electrons [48-49]. Because of this limitation, we used relative oxidation state value rather than a nominal average.

2.2.4 BET surface area and pore size distribution

The BET surface area and pore size distribution for each sample was measured by nitrogen adsorption at 77 K using a Micrometrics Tri-Star II BET surface area analyzer. Prior to analysis, the samples were degassed for 30 min at 150 °C with a helium purge.

2.2.5 Thermogravimetric analysis (TGA)

TGA was conducted using a TA Instruments Q500 TGA to evaluate sample weight loss with increasing temperature. The temperature was varied from ambient temperature to 900 °C using a 10 °C/min ramp. Nitrogen gas was used to purge the furnace at 60 mL/min. The sample was held in a platinum pan.

2.3 Gas-phase catalytic oxidation of ethanol

The cryptomelane samples in this investigation were evaluated as catalysts for the gas phase oxidation of ethanol within a 25 °C – 200 °C temperature range. The catalytic oxidation of ethanol, shown in equations (1) and (2), generates acetaldehyde and carbon dioxide primary reaction products.

$$CH_3CH_2OH_{(g)} + \frac{1}{2}O_{2(g)} \rightarrow C_2H_4O_{(g)} + H_2O_{(g)} \tag{1}$$

$$C_2H_4O_{(g)} + \frac{5}{2}O_{2(g)} \rightarrow 2CO_{2(g)} + 2H_2O_{(g)} \tag{2}$$
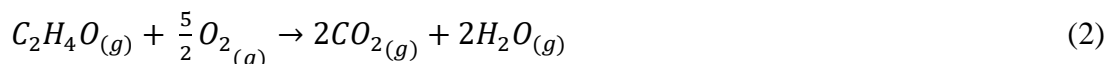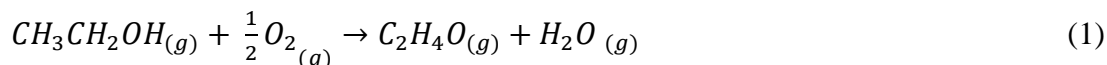
A schematic of the catalytic test system is illustrated in Figure 1. Catalyst materials were ground in a mortar and pestle to a fine powder (10-500 μm particle size). Approximately 50 mg of each sample was loaded into a stainless steel tube reactor in a bed of quartz wool. The tube reactor was 55 cm long, with a 0.635 cm outer diameter, and a 0.124 cm wall thickness; the catalyst plug volume was 0.47 cm^3 (gas hourly space velocity (GHSV) = 12,750 hr^{-1}).

The tube reactor was loaded into a Lindberg Blue M tube furnace. Ethanol vapor was generated in a diffusion cell at concentrations ranging from 310-390 ppm and directed at 100 ccpm into the reactor. Analysis of the diffusion cell effluent was performed before and after each run to ensure consistent ethanol concentration during the run. The effluent was collected after allowing the reactor to equilibrate at each temperature interval for one hour and analyzed used an Agilent 6890N gas chromatograph with flame ionization detection (GC/FID), which was calibrated before each run using prepared ethanol standards ranging from 0-0.23676 mg/μL.

Samples were collected in both gas phase using a Tedlar ® sampling bag and in liquid phase by scrubbing the reactor effluent in deionized water in a Pyrex ® glass impinger to measure concentrations of ethanol and acetaldehyde. To assess reproducibility of our experimental results, at each temperature interval, two 10 mL liquid samples were taken for 10 minutes and two-three 0.5 μL injections of each were performed; the gas sample was injected three times in 250 μL volumes. The GC/FID measured ethanol and acetaldehyde concentrations in the effluent and carbon dioxide in the effluent was measured at each interval using an Amprobe® CO_2-100 non-dispersive infrared CO_2 detector (1 ppm resolution, $\pm$ 30 ppm accuracy) which was calibrated between 0 and 2000 ppm using prepared air-CO_2 mixtures.

Ethanol flow rates were determined by multiplying the concentration by the sample volume divided by the sampling time. Conversion percentage values were calculated from mean ethanol flow rates (μmoles/min) for each sample, using the flow and ethanol concentration values measured at 25°C as the initial concentration – supported by the absence of detectable acetaldehyde or CO_2. Acetaldehyde concentration was calculated using the ethanol calibration standard curve as they have approximately the same molecular weight, number of carbon atoms, and chemical behavior – this value was then used to derive mean flow rate as described above for ethanol. CO_2 concentration in the effluent was directly measured as described; atmospheric CO_2 was measured and subtracted and the resulting value was calibrated according to the standard curve generated by the air-CO_2 mixtures. CO_2 flow rate was calculated by multiplying concentration by the reactor effluent velocity (100 ccpm).

3.   Results

3.1   XRD

The XRD patterns for the cryptomelane samples are shown in Figure 2. All of the samples were identified as tetragonal (*I* 4/m) cryptomelane (PDF #01-072-1982) with figures-of-merit values ranging from 4.0-5.9. In all samples, no secondary phases were detected, indicating that the incorporation of Eu into the cryptomelane structure was successful or that any secondary phases present were beyond the instrument resolution. In the Eu-doped samples, reflections were generally broadened and diminished in intensity, likely reflecting an overall smaller crystal size with crystallographic defects. SS-IE had the most significant reflection broadening compared to

the other Eu-doped samples. Minor positive shifts in 2-theta between undoped and doped species in the Eu-doped samples were found only in reflections *hk*0.

3.2   *SEM and EDS*

SEM micrographs showed that solid state cryptomelane samples were comprised of uniform, randomly-oriented, stout, needle-shaped crystals approximately 20-100 nm in length and 10-20 nm in width (Fig. 3 a-c). Due to the resolution limits of the SEM, SS-CON, SS-CP, and SS-IE were virtually indistinguishable from one another, making further morphological characterization with TEM necessary. Reflux cryptomelane samples were comprised of non-uniform, randomly-oriented, slender, needle-shaped crystals approximately 50-1000 nm in length and 20-100 in width (Fig. 3 d-f). In contrast to the solid-state cryptomelanes, the doped reflux cryptomelanes had apparent plaque-like growths on the crystals (Fig. 3 e-f). The nature of the 'plaque' was unable to be resolved with SEM and so TEM analysis was required to determine the details of these textures.

The XED spectra for the cryptomelane samples in this study displayed X-ray emission lines for potassium, manganese, and oxygen with no detectable chemical impurities; europium lines were observed only in the doped samples. A summary of the sample chemistry in atomic percentages is shown in Table 2; these values are based upon multiple measurements within the same sample and also of duplicate samples.

R-CON and SS-CON had approximately identical chemical compositions consistent with the stoichiometry of cryptomelane – approximately 32 at.% Mn, 4 at.% K, and 64 at.% O. SS-CP had 5.0 at.% Eu. This Eu enrichment was accompanied by a significant decrease in Mn content (-10.2 at.%) and an increase in O content (+5.1 at.%); K content remained constant (3.6 at.%). SS-IE had 0.8 at.% Eu. This Eu enrichment was also accompanied by a decrease in Mn content (-3.3 at.%) and an increase in O content (+2.7 at.%); however, K content had decreased slightly (-0.3 at.%).

R-CP had 0.7 at.% Eu. Like SS-CP, R-CP's Eu enrichment was accompanied by a decrease in Mn content (-3.5 at.%) and an increase in O content (+3.1 at.%); however, there was a measurable decrease in K content (-0.2 at.%), which was not observed in the solid state analogue. R-IE had 0.6 at.% Eu. This Eu-enrichment was accompanied by a decrease in Mn (-5.1 at.%) and an increase in O content (+4.9 at.%); a decrease in K was also observed (-0.4 at.%).

3.3   TEM

TEM micrographs showing representative general textures of each sample are shown in Figure 4. All of the solid-state cryptomelane images (Fig. 4 a-c) showed textural information consistent with that observed in the SEM data. SS-CON crystals were approximately 20-80 nm long and 5-10 nm wide, SS-CP crystals were 20-60 nm long and 5-15 nm wide, and SS-IE crystals were 20-60 nm long and 5-10 nm wide; all solid state samples had the general crystal morphology of short, stout fibers. No other phases were detected in the solid state samples; however, it was observed that both SS-CP and SS-IE's crystal populations were smaller and less heterogeneous in size. SS-IE's crystals had a prevalent lumpy and pitted surface texture that was not present in other samples in this investigation (Fig. 5 a-b). Closer inspection shows that the crystallinity of SS-IE was not damaged, evident from reasonably defect-free lattices, but there did appear to be a general uneven, potentially amorphous 'rind' around the crystals (Fig. 5b – inset). It is this 'rind' that was potentially responsible for the broader XRD reflections for SS-IE.

Within the reflux cryptomelanes, longer fibrous crystals were observed, consistent with SEM data (Fig. 4 d-f). R-CON crystals ranged 100-1500 nm long and 10-50 nm wide, R-CP crystals ranged 25-300 nm long and 5-30 nm wide, and R-IE crystals were in 50-2000 nm long and 10-40 nm wide. R-CON showed clean, apparently defect-free crystals. R-CP was very similar in terms of crystallinity, with an average reduction in crystal size homogeneity. As in the solid state samples, R-CP had a general texture of larger crystals intermixed with smaller crystal 'fragments'. It is the bi-modal size distribution that was likely responsible for the 'plaque' texture observed in R-CP in SEM as all material observed in TEM was identified as cryptomelane.

R-IE cryptomelane was nearly identical in texture to R-CON but present and intimately associated with it were hexagonal, equant crystals (Fig. 4f and Fig. 6a and 6a-inset) approximately 50 nm in size – it is this phase that was interpreted as the 'plaque' observed in SEM. In addition to the anomalous hexagonal crystals, R-IE showed prevalent lenticular omission defects not observed in any of the other cryptomelane samples in this study (Fig. 6b). Atomic imaging of the hexagonal crystals showed lattice fringe d-spacing of 0.44 Å (Fig. 6c).

Because of the presence of an additional phase in R-IE, STEM-XEDS maps of an interface between a cluster of cryptomelane crystals and one of the hexagonal crystals were obtained to show the elemental composition to try and elucidate the identity of this phase, which

was not detected in the XRD data. The elemental maps show that distribution of Mn, O, and Eu were homogenous between the phases, however, the hexagonal crystal was conspicuously lacking K, unlike the adjacent cryptomelane crystals (Fig. 7). These data, coupled with morphological data, lattice-spacing (Fig. 6c), and EELS data (detailed later) led us to interpret this phase as the manganese oxide mineral, bixbyite ($Mn^{3+}_2O_3$); the presence of Eu yielding a nominal general formula (Mn, Eu)$_2$O$_3$.

In addition to textural and lattice fringe imaging in the <200> direction, micrographs of each sample were taken down the tunnel axis <001> to observe if any major crystalline defects were present in this direction (Fig. 8). All samples showed no observable dislocations or omissions in this direction. Although the XRD data showed that all of the samples are tetragonal (*I* 4/m), the reflection broadening induced by Eu-doping necessitated detailed analysis of images down the tunnel axis to determine if symmetry reduction was present, particularly close to or at the crystal surface. The *I* 2/m polymorph of cryptomelane differs *very* slightly from *I* 4/m (Fig. 9), the main difference being a 1° tilt of the framework. Obtaining these images was highly challenging particularly for the reflux species as their crystals are larger. From the data gathered, it was reasonable to interpret SS-CP and R-IE as having some minor tilt, making it potentially partially monoclinic and SS-IE of being fairly tetragonal.

3.4   EELS

The EELS results, displayed in Table 3, showed that SS-CP did not appear to have a different average Mn oxidation state than SS-CON whereas SS-IE appeared to have a greater average oxidation state, as can be observed from the positive L_3 shift and increase in ΔE. Although the R-CP Mn-L_3 was 1.0 eV less than the Mn-L_3 of R-CON (644.4 vs. 643.4 eV) indicating Mn oxidation state decrease; R-CP's ΔE was larger than R-CON's (10.8 vs 10.2 eV), indicating oxidation increase. Because the position of Mn-L_2 did not change commensurately as it did in the other samples, the spin-orbital splitting value was more reflective of the state. Thus, R-CP's Mn oxidation state was interpreted to have increased. A significant reduction in the average Mn oxidation state was present in R-IE compared to R-CON. In addition to the cryptomelanes, the phase potentially identified as Eu-bixbyite had a slightly higher average oxidation state than R-IE with which it co-exists.

3.5   Surface area, pore volumes, and pore size distributions

The surface areas of the cryptomelane samples are summarized in Table 1. Surface area values were higher on average for SS-CON than those for R-CON (92.0 m^2/g and 79.6 m^2/g, respectively), likely owing to smaller crystallite size. Surface area values of the SS-CP and R-CP were higher than the controls (115.7 m^2/g and 99.4 m^2/g, respectively). SS-IE's surface area was measured as 97.1 m^2/g, a net increase from SS-CON, but R-IE's surface area (70.4 m^2/g) was less than R-CON's.

Although micropores (<20 Å), mesopores (20–500 Å), and macropores (>500 Å) exist in cryptomelane, the use of nitrogen as an adsorbent as well as the presence of potassium/europium ions in the narrow (<7 Å) channels in the crystal structure, limits the ability to measure most of the micropores of the crystal structure [2, 30]. Therefore the pore volumes and pore distribution values reported in Table 1 are between 17 Å and 3000 Å.

In the solid state samples, all of the BJH adsorption pore volume curves showed a narrow size distribution of mesopores centered on approximately 100 Å in diameter (Fig. 10.). Most of the SS-CON's mesopores were larger than the SS-IE's and even larger still than the SS-CP's mesopores (109.2>99.3>88.3 Å). The SS-CP was the only solid state sample to have any observed macroporosity, although the percentage was minor in comparison to values observed in the reflux cryptomelanes. The type IV isotherms of the solid state samples showed type H_{2B} hysteresis, indicating these samples had relatively uniform, channel-like pores with slightly narrow pore mouths (Fig. 11).

In the reflux samples, all of the BJH adsorption pore volume curves showed a narrow pore size distribution centered at approximately 30 Å with a broader distribution in the range of 255–310 Å (Fig. 10). All reflux samples had significant macroporosity, which was reflected in the reflux samples' low bulk densities (approximately 0.5 g/mL), in comparison to those of the solid state series (approximately 1.0 g/mL); bulk density values are also reported in Table 1. Macroporosity was highest in R-IE (52.5%), followed by R-CON (47.0%), and lastly by R-CP, which had the least percentage macroporosity (44.5%). The type IV isotherms of the reflux samples showed type H_1 hysteresis, indicating that the sample's mesopores were approximately uniform and cylindrical in shape; however, the narrow loop reflected the reflux samples' high macroporosity (Fig. 11).

3.6   TGA

The TGA curves for the cryptomelane samples in this investigation are shown in Figure 12. Published literature defines the four main stages of cryptomelane mass loss as (1) loss of physically adsorbed water at temperatures < 200 °C, (2) loss of chemisorbed water and lattice oxygen between 200 °C and 500 °C, (3) the phase transformation from cryptomelane to bixbyite ($Mn_2^{3+}O_3$) between 500 °C and 700 °C, and (4) the phase transformation from bixbyite to hausmannite ($Mn^{2+}Mn_2^{3+}O_4$) at temperatures > 700 °C [2, 41, 50-52].

The solid state cryptomelane samples in this study steadily lost mass from physically adsorbed and chemisorbed water until approximately 500 °C. SS-CON began the transformation to bixbyite at approximately 520 °C, SS-CP at 600 °C, and SS-IE at 610 °C. SS-CON then began to transform to hausmannite at 660 °C, SS-CP at 680 °C, and SS-IE at 675 °C. SS-CON, SS-CP, and SS-IE completed the hausmannite transition at 740 °C, 775 °C, and 775 °C, respectively.

The reflux cryptomelane samples steadily lost mass from physically adsorbed and chemisorbed water until approximately 550 °. R-CON began the transformation to bixbyite at approximately 545 °C, R-CP at 590 °C, and R-IE at 600 °C. R-CON then began to transform to hausmannite at 660 °C, R-CP at 660 °C, and R-IE at 600 °C. R-CON, R-CP, and R-IE completed the hausmannite transition at 725 °C, 775 °C, and 775 °C, respectively.

Table 4 shows a comparison of the mass loss percentages of the samples during each transitional temperature interval. Overall, the solid state series lost more mass from physically adsorbed water than the reflux series. This is potentially due to differences in surface area. In both solid state and reflux cryptomelanes, co-precipitated samples lost more mass from physically adsorbed water than the non-promoted samples whereas ion-exchanged material lost less mass from physically adsorbed water than the non-promoted samples. As co-precipitation increased surface area in both series, there was likely simply more physically adsorbed water to lose. Ion-exchanged samples, although having higher surface area than non-promoted samples, lost less water. This indicated that the ion-exchange may have increased hydrophobicity in cryptomelane due to high concentrations of europium at the surface relative to the bulk.

Overall, solid state species lost more mass between 200 °C and 500 °C and less mass between 500 °C and 700 °C than the reflux species did. This may have been due to higher surface areas allowing for greater chemisorption of water in the solid state species as well as smaller overall crystal size. Within each series, the ion-exchange species lost less mass between 200 °C and 900 °C than the non-promoted species whereas the co-precipitated samples lost more

22

than the non-promoted species, a correlation also found at temperatures <200 °C. The differences were likely complex and related to europium's spatial position and concentration.

3.7   *Catalytic oxidation of ethanol*

The light-off curves for each catalyst, which show ethanol conversion percentage as a function of temperature, are shown in Figure 13. The T_{50} and T_{90} values of each light-off curve – which reflect the temperature at which the catalysts are respectively converting 50% and 90% ethanol – are shown in Table 5. Finally, Figure 14 shows the flow rate in all effluent species detected and measured in this study (ethanol, acetaldehyde, and carbon dioxide) as a function of temperature.

In each run, the moles of carbon in the effluent products (ethanol, acetaldehyde, and carbon dioxide) were within 90-97% of the total moles of carbon fed into the reactor, excepting R-IE which was 78% of the moles fed. Due to the volatility of acetaldehyde in the liquid phase, it was likely a strong contributor to any error. Ethylene, carbon monoxide, and acetic acid are also potential trace compounds in the effluent that could contribute to the mass balance error; however, none were observed with the analytical methods used in this study.

All catalysts in this study had catalytic activity for the oxidation of ethanol between 25-200 °C. All catalysts achieved 100% ethanol conversion before or by 200 °C. At 25 °C, none of the catalysts were converting any ethanol as evidenced by the lack of acetaldehyde or CO_2 generation. At 100 °C, all of the catalysts samples had begun converting ethanol as shown in Fig. 14 by the decrease in ethanol flow in the effluent and the appearance of acetaldehyde. Only SS-CON and SS-CP appeared to be 'completing' the reaction as evidenced in the generation of CO_2. At 100 °C, SS-CON was converting an average of 6.74% ethanol; SS-CP an average of 32.4% ethanol; SS-IE an average of 4.71% ethanol; R-CON an average of 24.6% ethanol; R-CP an average of 22.3% ethanol; and R-IE an average of 5.30% ethanol, as shown graphically in Fig. 11.

At 125 °C, all of the catalysts were converting ethanol into acetaldehyde and finally CO_2, as shown by the continually decreasing ethanol flow rate and presence of the intermediates and products. For all species, maximum acetaldehyde flow was measured at 125 °C. At 125 °C, SS-CON was converting an average of 37.0% ethanol; SS-CP an average of 42.6% ethanol; SS-IE an average of 42.6% ethanol; R-CON an average of 48.8% ethanol; R-CP an average of 28.8% ethanol; and R-IE an average of 36.3% ethanol.

At 150 °C, ethanol flow rates continued to decrease while acetaldehyde plateaued and CO_2 sharply rose in all species as the forward reaction energy barrier was weakened. At 150 °C, SS-CON was converting an average of 74.1% ethanol; SS-CP an average of 69.9% ethanol; SS-IE an average of 66.5% ethanol; R-CON an average of 62.0% ethanol; R-CP an average of 58.0% ethanol; and R-IE an average of 54.9% ethanol.

At 175 °C, SS-CON and SS-CP had converted 100% of ethanol whereas SS-IE and all of the reflux samples were not finished yet. In SS-CON, there was less acetaldehyde in the effluent at 175°C than SS-CP, indicating that it was driving the reaction forward more. At 175 °C, R-CON was converting an average of 76.0% ethanol, R-CP was converting 75.3% ethanol, and R-IE was converting 74.3% ethanol. In all reflux species, acetaldehyde flow remained approximately constant or a small amount less than that measured between 100 and 150 °C.

At 200 °C, no more acetaldehyde was measured in the solid state cryptomelanes, indicating that the reaction had been driven fully toward final products. In the reflux cryptomelanes, 100% conversion has been achieved; however, R-CON still maintained 0.3 μmoles/min acetaldehyde in the effluent, indicating a lag in completion, which R-CP and R-IE had overcome.

The oxidation of ethanol reaction is assumed to be first order with respect to ethanol concentration [41, 53]; therefore, the activation energy (E_a) was determined here by first determining the reaction rate constant (k) for each temperature interval in a run from Equation 3, linearized in Equation 4.

$$C_A = C_{A_o} \times e^{-k\tau} \tag{3}$$

$$\ln\left(\frac{C_A}{C_{Ao}}\right) = -k\tau \tag{4}$$

C_A is concentration of ethanol in the reactor effluent at time $= n$ and C_{Ao} is the initial concentration of ethanol at time zero. Because the reactor was a plug flow type, the variable τ for residence time was used and calculated from the volume of the reactor (V) divided by the volumetric flow rate (Q). Activation energy was determined using the Arrhenius equation (Equation 5, linearized in Equation 6). The natural log of k as determined for each temperature interval above was then plotted against inverse temperature, the slope of this line (-E/R) was used to calculate activation energy (E).

$$k = Ae^{-\frac{E}{RT}} \tag{5}$$

$$\ln(k) = \ln(A) - \frac{E}{R}\left(\frac{1}{T}\right) \tag{6}$$

Where k = reaction rate constant (s^{-1}), A = pre-exponential factor (s^{-1}), E = activation energy (kJ/mole), R = gas constant (0.008314 kJ/mol*K) and T = absolute temperature (K).These activation energies, calculated at inlet ethanol values of 310-390 ppm, are listed in Table 5.

The reaction rates (μmoles/min) were calculated per gram of catalyst (Equation 7) and per square meter of catalyst (Equation 8) where X_a is equal to the fraction of ethanol converted at 150 °C and Q_a is equal to the initial ethanol flow in μmoles/min multiplied by two for stoichiometric balance.

$$\frac{X_{a_{150\,°C}} \times Q_{a_o}}{Mass\ of\ Catalyst\ (g)} = \frac{\mu moles}{min \times gram\ catalyst} \tag{7}$$

$$\frac{X_{a_{150\,°C}} \times Q_{a_o}}{Mass\ of\ Catalyst\ (g) \times Surface\ Area\ (\frac{m2}{g})} = \frac{\mu moles}{min \times m^2\ catalyst} \tag{8}$$

Table 5 summarizes the observed reaction rates per mass of catalyst and per surface area of each catalyst in this study at 150 °C, selected because there is the most disparity in apparent activity.

4.   Discussion

4.1   *Crystal structure, crystal chemistry, and physical properties (XRD, SEM, TEM, BET)*

The presence of Eu did not significantly change the average crystal size or the overall crystal structure arrangement of all the cryptomelane samples in this study, indicated by the *d*-spacings determined in the XRD data. There was an overall broadening of reflections and diminishment in intensity between the control species and the Eu-doped species (Fig. 2). This result was also reported for Ce-cryptomelane and was attributed to reduction in average crystal size and introduction of crystallographic defects [26-27, 35, 37-38, 54-55].

Although a small reduction in average crystal size was noted for SS-CP, SS-IE, and R-CP using the TEM data, the textural information suggests that Eu instead increased crystal size bimodality in these samples but not significantly in the overall range of crystal dimensions in the samples. The increase in crystal size bi-modality in SS-CP, SS-IE, and R-CP was reflected in gains in surface area and losses in average mesopore diameter. SS-IE had the most significant change in reflection intensity and broadness; this is interpreted as having to do with the potentially amorphous 'rind' found on the crystals in the TEM data (Fig. 5). R-IE experienced an

overall increase in crystal size and commensurate decrease in surface area. The disparity in crystal sizes in this study are far more likely to be the result of synthesis method – which is a function of differences in mass transport and diffusion capacity in the solid-state method and in the reflux method. The more pressing question in this study relates to *where* Eu went into or onto the cryptomelane structure and how that incorporation affected the physical properties observed and ultimately, the catalytic activity.

4.1.1 *Solid state cryptomelane Eu-doped via co-precipitation (SS-CP)*

SS-CP experienced a decrease in average crystal size, which was also correlated with its higher specific surface area and larger pore volume per gram of sample. The term 'pore' is a bit of a misnomer as most of the 'pores' identified and measured in the N_2 adsorption experiments were spaces between adjacent crystals or large surface defects. From the TEM data (Fig 4b) it can be observed that the mix of large and small crystals created more of these types of pores.

According to the XEDS data, SS-CP had less Mn, more O, and the same percentage of K as SS-CON, albeit with 5.0 at.% Eu. This result suggests that Eu^{3+} is substituting for Mn^{3+}, rather than K^+. The crystal radius of Mn^{3+} in 6-coordination is 0.8 Å. Although a somewhat small site for Eu^{3+} (1.1 Å), it is likely a more favorable position than the larger, 8-coordinated K^+-site (1.65 Å). This mechanism is supported by TEM data showing what is interpreted as a shift toward a monoclinic structure in at least some regions of the sample (Fig. 8b), which may need to occur to accommodate a larger cation. This is also supported by the lack of Mn oxidation state change from SS-CON to SS-CP as observed in the EELS data (Table 3). Additionally, literature supports that Ce substitutes both in the framework and tunnel sites in cryptomelane, a mechanism largely controlled by synthesis method [56].

The TGA data of SS-CP showed less weight loss overall compared to the control species. More weight was lost at temperatures <200°C, indicating that SS-CP had more physically adsorbed water than the control. This is likely a function of increased surface area; however, SS-IE lost less weight from physically adsorbed water even though it has a slightly larger than SS-CON, so surface area alone cannot be used to explain this difference.

4.1.2 *Solid state cryptomelane Eu-doped via ion-exchange (SS-IE)*

SS-IE has a slightly larger surface area than SS-CON and a larger pore volume per gram of material. Similarly to SS-CP, this is likely a function of increased population of smaller crystals intermixed with larger ones. In the XEDS data of SS-IE, there were reductions in both Mn and K at.%, indicating that likely Eu^{3+} exchanged with K^+, the result of which may have led to Mn^{2+} leeching, the effect of which produces octahedral-site defects, a phenomenon observed by Santos et al. [34] in Ce-OMS-2, and supported by our XRD data and EELS data.

SS-IE shows an overall Mn-oxidation state increase; crystallographically, the mechanism may be the combination of Eu-K substitution and Mn^{2+} loss. There were not any additional phases observed, such as the $(Eu,Mn)_2O_3$ found in R-IE observed; however, the uneven surface texture observed in TEM may be an indication of what happened during ion-exchange (Fig. 5). A potential explanation of this texture is that free Mn or Mn+Eu re-precipitated into a near-surface amorphous rind, rather than as crystalline $(Eu,Mn)_2O_3$. This texture and mechanism were described by Gac et al. [57] who reported that introduction of dopants (Ag) via impregnation reduced the number of free-hydroxyl groups and produced a near-surface amorphous texture on their cryptomelane crystals due to the different octahedral arrangement.

4.1.3   *Reflux cryptomelane Eu-doped via co-precipitation (R-CP)*

According to XEDS data for R-CP, Eu-doping reduced Mn and K and increased O content. The mechanism for this substitution is likely complex, but in reflux cryptomelanes doped with cerium via co-precipitation, Ma et al. [35] found that Ce^{4+} mainly replaces K^+ and partially replaces Mn^{4+} in the framework. Due to similarity in chemical behavior in solution, Eu potentially behaved similarly in cryptomelane although differences may have occurred due to differences in oxidation state between the two ions (3^+ vs 4^+, respectively). Another potential result is only Eu-K substitution with a resulting loss in Mn as is suggested in SS-IE and R-IE – both mechanisms are supported by the EELS data (Table 3) which shows that R-CP experienced an overall increase in Mn oxidation state relative to R-CON.

R-CP did have a smaller overall crystal size than R-CON, 13.53 nm vs. 17.57 nm wide, respectively, as determined in XRD and a smaller and narrower crystal length distribution: 25-300 nm long vs. 100-1500 nm long, respectively. The presence of Eu likely introduced defects which caused this size limitation; this is also supported by the positive 2-theta shifts in the XRD

data. Because of this smaller crystal size, pore volume is larger than in R-CON and overall macroporosity decreased.

Similar to SS-CP, R-CP lost more weight at temperatures less than 200 °C, indicating more physically adsorbed water than in R-CON. This may be related to increase in surface area, but as in SS-CP, the surface area may not be the only contribution to more surface water. A potential explanation is that all co-precipitated cryptomelanes were more hygroscopic. The ion-exchanged cryptomelanes both lost less weight from physically adsorbed water than the controls, potentially indicating they were less hygroscopic.

4.1.4 *Reflux cryptomelane Eu-doped via ion-exchange (R-IE)*

In the XEDS data for R-IE, similar trends are found as in SS-IE. Decrease in Mn and K content and increase in oxygen content. As in SS-IE, Eu likely had some exchange with K, leading to a loss of Mn^{2+} and the introduction of defects. The major difference here, is that R-IE has Eu-bixbyite crystals co-existing whereas SS-IE experienced amorphous occlusion.

Bixbyite (Mn_2O_3) has been observed in syntheses of cryptomelane at very low pH (pH 2) as a co-existing precipitate; however, no studies have observed it occurring post-crystallization as a result of ion exchange [8, 12]. Because Mn_2O_3 was not observed in either of the replicate R-CON samples and was observed in both of the R-IE preparations, the formation of Mn_2O_3 seems to have occurred during ion-exchange. Manganese lost during Eu^{3+}-K^+ substitution is the likely source for $(Eu,Mn)_2O_3$, which may have grown during calcination. The fact that this precipitate did not occur in SS-IE is odd, but may have to do with the lower average Mn oxidation state in SS-IE; on average, the lower the oxidation state of Mn, the stronger the Pauling bond will be. This mechanism is supported by the EELS data (Table 3), which shows a lower average oxidation state for cryptomelane (likely due to the loss of Mn^{2+}) and an even lower average oxidation state for Mn_2O_3, which makes sense as there would be no tetravalent Mn.

With respect to other physical properties, the results of R-IE are interesting compared to cryptomelane samples prepared similarly with cerium. Some Ce-doped cryptomelane showed improved surface area and porosity [26, 38] while another investigation reported minimal to negative improvement in these properties with a CeO_2 secondary phase precipitation but only at higher molar concentrations of cerium(III) nitrate [27]. Some of these differences may be related to differences in exchange protocol – perhaps longer exchange times are detrimental as they

allow for secondary phase formation or maybe this could be avoided by frequent nitrate solution refreshment.

4.2   Catalytic performance

The oxidation of ethanol over cryptomelane follows a Mars and Van Krevelen (MVK) mechanism in which the catalyst's lattice oxygen oxidizes the adsorbed organic molecule, leaving an oxygen vacancy that is subsequently replenished by gaseous oxygen [58]. In the reaction, ethanol is first adsorbed onto the surface of cryptomelane in the form of intermediate ethoxides and acetates facilitated by the participation of lattice oxygen, weakly bound surface oxygen (O_2^-), and OH^- groups; during this, Mn^{4+} is reduced to Mn^{2+} [12, 59-61].

The ethoxides and acetates then interact with the cryptomelane surface, favoring hydrogen abstraction to form acetaldehyde or cleaving carbon-carbon bonds to complete the oxidation. This leaves an oxygen vacancy in the catalyst which is replenished by gaseous oxygen, oxidizing Mn^{2+} to Mn^{4+}. The steps in the MVK mechanism are shown in equations (9-12), which lead to the overall observed reaction depicted in equations (1) and (2).

$$CH_3CH_2OH_{(g)} + Mn^{4+}{}_{(s)} \rightarrow CH_3C(O)H_{(g)} + Mn^{2+}{}_{(s)} + 2H^+{}_{(g)} \tag{9}$$

$$2H^+{}_{(g)} + O_2^{2-}{}_{(g)} \rightarrow H_2O_{(g)} + \frac{1}{2}O_2{}_{(g)} + (*) \tag{10}$$

$$O_2{}_{(g)} + (*) + 2e^- \rightarrow O_2^{2-}{}_{(g)} \tag{11}$$

$$Mn^{2+}{}_{(s)} \rightarrow Mn^{4+}{}_{(s)} + 2e^- \tag{12}$$
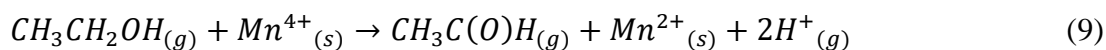
Surface area, pore size and geometry, and crystallinity and crystal texture are not solely responsible for catalytic activity improvement in this reaction. The oxidation state of Mn in cryptomelane has been demonstrated to be equally if not more important than surface characteristics. Indeed, a higher Mn oxidation state has been demonstrated to improve catalytic activity through the availability of lattice oxygen [62]; however, it is not always so simple. The more oxidized sample may not necessarily have the best activity due to the energy requirements (reducibility and reactivity) needed to make lattice oxygen transfers to the organic molecules, requirements dependent on the global oxidation state of the catalyst [8, 12]. Other factors that could introduce complications related to Mn-oxidation state are chemical or physical impurities, which can inhibit lattice oxygen transfer – this will be discussed further in detail later.

All of the cryptomelane catalysts in this study have activity for the oxidation of ethanol, meaning the addition of Eu did not diminish this base capacity; however, some catalysts clearly performed better than others. The activations energies of ethanol on cryptomelane catalysts in this study range from 26.2 – 133.7 kJ/mol (Table 5). These values are within the range of activation energies reported for the catalytic oxidation of ethanol which range 25 kJ/mol to greater than 130 kJ/mol over a variety of catalysts [41, 53, 63-68].

As discussed above, addition of Eu to cryptomelane has affected its crystal structure, texture and size, pore size and geometry, oxygen content, Mn oxidation state, and amount of physically adsorbed water in all species. The contribution of these changes for each catalyst with respect to observed activity is described below.

4.2.1 Solid state cryptomelanes

Eu-doping via co-precipitation had a significant effect on the activation energy (Table 5) and light-off curves (Fig. 13) of the solid state cryptomelanes. SS-CP had a dramatically lower activation energy than SS-CON – 32.0 kJ/mol vs. 78.2 kJ/mol. The activity improvement in SS-CP is probably mostly related to its higher specific surface area; but as it was the sample in this study with the highest amount of Eu at 5.0 at%, EuO_6 groups may have increased lattice oxygen availability, introduced surface defects, or increased surface oxygen density through the increase in hydroscopy. Of the four Eu-doped cryptomelanes produced in this study, SS-CP is the only sample to show improvement in all measured properties that contribute to better activity in this oxidation reaction and also demonstrate actual improved performance.

Although SS-IE had high surface area as well as higher lattice oxygen content, its activation energy was only slightly improved compared to SS-CON at 74.9 kJ/mol. A potential reason for this is the amorphous layer coating the surface of crystals of SS-IE (Fig. 5) which may have made lattice oxygen less labile throughout the reaction, but particularly at low temperatures. In spite of the introduction of some promising physical and chemical properties, SS-IE did not perform well as a catalyst such as to recommend further development unless efforts can be made to avoid amorphous surface precipitates.

Although it had a poor activation energy and the lowest specific surface area among the solid state samples, SS-CON had higher reaction rates with respect to both mass and surface area of catalyst at 150 °C than the Eu-doped varieties. This phenomenon may have been a reflection

of diminished reactant access to lattice oxygen and/or ability of products to desorb from the surface due to reduction in pore size in the doped species. Although the reactivity of cryptomelane has been found to have almost linear relationship with specific surface area in oxidation reactions [41, 51-52, 69], surface area alone cannot explain catalytic activity; access to active sites is a major control [70]. At higher temperatures, SS-CON appeared to make up for what it lacked in surface area by its ability to transport reactants and products due to its more uniform crystal and pore size range.

4.2.2 *Reflux cryptomelanes*

Eu-doping reflux cryptomelane by co-precipitation had a diminishing effect with respect to activation energy (26.9 kJ/mol vs. 43.2 kJ/mol). In comparison with SS-CP, where the substitution mechanism was more straightforward to interpret ($Eu^{3+} \rightarrow Mn^{3+}$) and the catalyst activity commensurately improved, R-CP's behavior was complicated. Catalytic activity was indeed hypothesized to improve because of gains in surface area and mesoporosity as well because Eu was observed to be incorporated into the structure, rather than occupying some inhibiting secondary phase. Although Eu was observed to have been incorporated into the R-CP structure, unlike in SS-CP, it appeared to occupy largely (K) tunnel sites. The tunnel position may have been deleterious on the catalytic activity, potentially due to changes in Mn oxidation state. In spite of poorer behavior at lower temperatures, R-CP had a higher reaction rate than R-CON and while both are converting 100% ethanol at 200°C, R-CP drove it all forward to products while R-CON was still producing intermediates; surface area was the likely contributing factor here but contribution of Eu to average oxidation state to the surface sites may have played a role.

R-IE had a severely diminished activation energy and reaction rate compared to R-CON and all the other catalysts in this study; however R-IE did still convert 100% of ethanol by 200°C. Although R-IE had the poorest surface area, the highest percentage of macropores, and the largest crystal size, its poor performance was attributed largely to the presence of Mn_2O_3, which has been found to decrease reactivity and mobility of lattice oxygen in cryptomelane and therefore decrease catalytic activity when mixed together [12].

To summarize, our results conceptually support those obtained by Liu and Hou [56] who reported that the position of Ce in the cryptomelane structure was critical to the lattice oxygen

activity. In contrast to our work, they reported that oxygen vacancy formation energy was lower when Ce occupied a tunnel position and higher when Ce occupied a framework position – this was correlated with an improved performance in benzene oxidation by the former. There is a strong possibility that Eu-doped cryptomelane may yield similar results, however the ion-exchange method investigated here, which built off of existing literature described in our methodology, did not achieve the intended result and instead led to occlusive additional phases on the cryptomelane which ultimately led to reaction inhibition. Certainly other differences in material may have played a role in this discrepancy, namely atom size, charge, ionization energy, and bonding characteristics. Further work should therefore be undertaken to determine a better method for ensuring Eu occupation of the tunnel site without additional phase precipitation.

Although the results of this investigation point to an overall positive impact of Eu-doping on cryptomelane when introduced via co-precipitation on solid-state type, the improvement is likely not significant enough to warrant the financial investment of europium. Indeed, the T_{50} and T_{90} values did not shift in any broadly meaningful, positive ways. In spite of this, this study demonstrates a wide variety of results with differing synthesis methods, particularly with respect to physical properties and crystal chemistry that can help to inform further research on modification of octahedral molecular sieve type catalysts as well as other similar catalytic systems.

5.   Conclusions

This study shows that the addition Eu alters the physical and catalytic properties of cryptomelane in different ways depending largely upon the mechanism of Eu-doping but also secondarily in combination with the synthesis method. Eu-doping cryptomelane via co-precipitation has generally positive effects on the properties that contribute favorably to the catalytic oxidation of ethanol, namely (1) increasing the surface area (115.7 m^2/g vs. 92.0 m^2/g for co-precipitated and control solid state species and 99.4 m^2/g vs. 79.6 m^2/g for co-precipitated and control reflux species, respectively; (2) increasing total mesoporosity (88.3 Å vs. 109.2 Å average pore width of co-precipitated and control solid state species and 273.7 Å vs. 306.9 Å average pore width of co-precipitated and control reflux species, respectively; (3) and increasing available lattice oxygen as observed by increasing relative Mn oxidation state with EELS. Only

SS-CP showed commensurate activity improvement in experimental reactions ($E_a = 32.0$ kJ/mol vs. 78.2 kJ/mol for co-precipitated vs. control, respectively).

Eu-doping cryptomelane via ion-exchange, however, shows deleterious effects on properties relevant to the catalytic oxidation reaction, prominently by precipitating bixbyite (Mn_2O_3) nanoparticles approximately 50 nm in size as in the reflux species or precipitating amorphous coatings due complex crystal-chemical changes on the solid state species. These features indeed resulted in commensurate inhibition in catalytic activity ($E_a = 74.9$ kJ/mol vs. 78.2 kJ/mol for ion-exchanged and control solid state species, respectively and 133.7 kJ/mol vs. 26.9 kJ/mol for ion-exchanged and control reflux species, respectively). This study demonstrates a range of nuance in catalyst modification research that can provide guidance for further investigations of this type.

References

[1] J. Luo, Q., Zhang, A., Huang, S.L. Suib, Micro. Meso. Mater. 35-36 (2000) 209-217. https://doi.org/10.1016/S1387-1811(99)00221-8

[2] J. Luo, Q. Zhang, J. Garcia-Martinez, S.L. Suib, J. Amer. Chem. Soc. 130:10 (2008) 3198-3207. https://doi.org/10.1021/ja077706e

[3] H. Deng, S. Kang, J. Ma, C. Zhang, and H. He, Appl. Catal. B 239 (2018) 214-222. https://doi.org/10.1016/j.apcatb.2018.08.006

[4] S. Said, M. Riad, M. Helmy, S. Mikhail, L. Khalil, Chem. and Mater. Res. 6 (12) (2014) 27-41.

[5] S. Said, M. Riad, M. Helmy, S. Mikhail, L. Khalil, J. Nanostruct. Chem. 6 (2016) 171-182. http://doi.org/10.1007/s40097-016-0192-3

[6] X. Zhang, Z. Mag, Z. Song, H. Zhao, W. Liu, M. Zhao, J. Zhao, J. Phys. Chem. C 123 (2019) 17255-17264. http://doi.org/10.1021/acs.jpcc.9b02499

[7] Z. Sihaib, F. Puleo, J.M. Garcia-Vargas, L. Retailleau, C. Descorme, L.F. Liotta, J.L. Valverde, S. Gil, A. Giroir-Fendler, Appl. Catal. B 209, (2017) 689-700. https://doi.org/10.1016/j.apcatb.2017.03.042

[8] V.P. Santos, M.F.R. Pereira, J.J.M. Órfão, J.L. Figueiredo, Top. Catal. 52 (2009) 470-481. https://doi.org/10.1007/s11244-009-9187-3

[9] D. F. Santos, O. S. Soares, J. L. Figueiredo, M. F. R. Pereira, Environ. Tech. (2018) 1-14. https://doi.org/10.1080/09593330.2018.1491639

[10] A.R. Gandhe, J.S. Rebello, J.L. Figueiredo, J.B. Fernandes, Appl. Catal. B 72 (2007) 129-135. https://doi.org/10.1016/j.apcatb.2006.10.017

[11] M.A. Peluso, L.A. Gambaro, E. Pronsato, D. Gazzoli, H.J. Thomas, J.E. Sambeth, Catal. Tod. 133-135 (2008) 487-492. https://doi.org/10.1016/j.cattod.2007.12.132

[12] V.P. Santos, M.F.R. Pereira, Appl. Catal. B 99 (2010) 353-363. https://doi.org/10.1016/j.apcatb.2010.07.007

[13] J.E. Post, Proc. Nat. Acad. Sci. 96(7) (1999) 3447-3454. https://doi.org/10.1073/pnas.96.7.3447

[14] R.N. DeGuzman, Y.F. Shen, E.J. Neth, S.L. Suib, C.L. O'Young, S. Levine, J.M. Newsam, Chem. of Mater. 6(6) (1994) 815-821. https://doi.org/10.1021/cm00042a019

[15] S. Ching, J. L. Roark, N. Duan, S. L. Suib, Chem. of Mater. 9(3) (1997) 750-754. https://doi.org/10.1021/cm960460k

[16] Q. Zhang, J. Luo, E. Vileno, S.L. Suib, Chem. Mater. 9(10) (1997) 2090-2095. https://doi.org/10.1021/cm970129g

[17] Y.S. Ding, X.F. Shen, S. Sithambaram, S. Gomez, R. Kumar, V.M.B. Crisostomo, M. Aindow, Chem. of Mater. 17(21) (2005) 5382–5389. https://doi.org/10.1021/cm051294w

[18] M. Sun, L. Yu, F. Ye, G. Diao, Q. Yu, Z. Hao, L. Yuan, Chem. Eng. J. 220 (2013) 320-327. https://doi.org/10.1016/j.cej.2013.01.061

[19] A. Awaluddin, L. Astuti, A. Linggawati, S.S. Siregar, P. Prasetya, L. Saputra, AIP Confer. Proc. 2026(1) (2018) 020075. http://doi.org/10.1063/1.5065035

[20] P. Legutko, J. Pęza, A.V. Rossi, M. Marzec, T. Jakubek, M. Kozieł, A. Adamski, Topics in Catal. 62 (2019) 599-610 http://doi.org/10.1007/s11244-019-01132

[21] S. Said, Heba H. El Maghrabi, M. Riad, S. Mikhail, J. Asian Ceram. Soc. 6(2) (2018) 169-181 http://doi.org/10.1080/21870764.2018.1480686

[22] R.K. Muya, L. Achola, E.C. Njagi, O. Ombaka, S.L. Suib, Reas. J. Life Sci., Bioinf., Pharm., Chem. Sci. 5(2) (2019) 16-30. http://doi.org/10.26479/2019.0502.02

[23] P. Stelmachowski, A.H.M. Videla, T. Jakubek, A. Kotarba, S. Specchia, Electrocatalysis 9(6) (2018) 762-769. http://doi.org/10.1007/s12678-018-0488-9

[24] N.T. Mo, L.M. Cam, Russian J. Phys Chem A 93(10) (2019) 2016-2002 http://doi.org/10.1134/s0036024419100182

[25] H. Tian, J. He, L. Liu, D. Wang, Ceram. Inter. 39(1) (2013) 315-321. https://doi.org/10.1016/j.ceramint.2012.06.027

[26] M. Abecassis-Wolfovich, R. Jothiramalingam, M.V. Landau, M. Herskowitz, B. Viswanathan, T. K. Varadarajan, Appl. Catal. B 59(1–2) (2005) 91–98. https://doi.org/10.1016/j.apcatb.2005.01.001

[27] E. Hapeshi, C.R. Theocharis, Adsorp. Sci. and Tech. 26(10) (2008) 789–801. https://doi.org/10.1260/026361708788708289

[28] S. Said, M. Riad, M. Helmy, S. Mikhail, L. Khalil, J. Porous. Mater. 24 (2017) 829-836. http://doi.org/10.1007/s10934-016-0322-9

[29] Y. Zhang, H. Zhang, Y. Xu, Y. Wang, J. Mater. Chem. 13(9) (2003) 2261-2265. https://doi.org/10.1039/B305538H

[30] J.V. Hernández, S. Coste, A.G. Murillo, F.C. Romo, A. Kassiba, J. of Alloy and Comp. 710 (2017) 355-363. https://doi.org/10.1016/j.jallcom.2017.03.275

[31] A. Zhang, J. Zhang, J. of Haz. Mater. 173(1-3) (2010) 265-272. https://doi.org/10.1016/j.jhazmat.2009.08.079

[32] T. Tian, C. Liu, J. Liao, X. Wei, T. Lu, J. Pow. Sourc. 174 (2007) 176-179. https://doi.org/10.1016/j.powsour.2007.08.082

[33] F. Wang, Y. Zheng, Y. Guo, Fuel Cells, 10(6) (2010) 1100-1107. https://doi.org/10.1002/fuce.200900158

[34] V.P. Santos, S.A.C. Carabineiro, J.J.W. Bakker, O.S.G.P. Soares, X. Chen, M.F.R. Pereira, F. Kapteijn, J. Catal. 309 (2014) 58-65. https://doi.org/10.1016/j.jcat.2013.08.030

[35] J. Ma, C. Wang, H. He, Appl. Catal. B 201 (2017) 503–510. https://doi.org/10.1016/j.apcatb.2016.08.050

[36] S.L. Suib, Acc. of Chem. Res., 41(4) (2008) 479-487. https://doi.org/10.1021/ar7001667

[37] M.H. Wu, J. Shi, H.P. Deng, Arab. J. Chem. 11(6) (2018) 924-934. https://doi.org/10.1016/j.arabjc.2018.02.002

[38] R. Jothiramalingam, B. Viswanathan, T.K. Varadarajan, Indian J. of Chem - A Inorg. Phys. Theor. Analy. Chem. 44(11) (2005) 2214–2217. http://nopr.niscair.res.in/handle/123456789/20224

[39] D. Frías, S. Nousir, I. Barrio, M. Montes, T. López, M.A. Centeno, J.A. Odriozola, Mater. Charac. 58(8–9 SPEC. ISS.) (2007) 776–781. https://doi.org/10.1016/j.matchar.2006.11.005

[40] J.S. Valente, D. Frías, P. Navarro, M. Montes, J.J. Delgado, E. Fregoso-Israel, E. Torres-García, Appl. Surf. Sci. 254(10) (2008) 3006–3013. https://doi.org/10.1016/j.apsusc.2007.10.042

[41] C. Almquist, M. Krekeler, L. Jiang, Chem. Eng. J. 252 (2014) 249–262. https://doi.org/10.1016/j.cej.2014.04.102

[42] J. Kilmartin, J.M. Fisher, J.E. Collier, D. Thompsett, R.R. Rajaram, U.S. Patent Application No. 10 (2018) 124,325.

[43] H. Tan, J. Verbeeck, A. Abakumov, G. Van Tendeloo, Ultramicr. 116 (2012) 24-33. https://doi.org/10.1016/j.ultramic.2012.03.002

[44] H.K. Schmid, W. Mader, Micron, 37 (2006) 426-432. https://doi.org/10.1016/j.micron.2005.12.004

[45] J. Lee, B. Kim, B.H. Kim, B.I. Min, S. Kolesnik, O. Chmaissem, C.J. Mais, B. Dabrowski, H.J. Shin, D.H. Kim, H. J. Lee, J.-S Kang, Physical Review B, 80(20) (2009) 205112. https://doi.org/10.1103/PhysRevB.80.205112

[46] Z.L. Wang, J.S. Yin, Y.D. Jiang, Micron, 31(5) (2000) 571-580. https://doi.org/10.1016/S0968-4328(99)00139-0

[47] D.H. Pearson, C.C. Ahn, B. Fultz, Phys. Rev. B 47(14) (1993) 8471. https://doi.org/10.1103/PhysRevB.47.8471

[48] L. Cavé, T. Al, D. Loomer, S. Cogswell, L. Weaver, Micron, 37(4) (2006) 301-309. https://doi.org/10.1016/j.micron.2005.10.006

[49] D.B. Loomer, T.A. Al, L. Weaver, S. Cogswell, Am. Min. 92(1) (2007) 72-79. https://doi.org/10.2138/am.2007.2252

[50] R. Jothiramalingam, B. Viswanathan, T.K. Varadarajan, J. of Mol. Catal. A 252(1-2) (2006) 49-55. https://doi.org/10.1016/j.molcata.2006.01.054

[51] F. Schurz, J.M. Bauchert, T. Merker, T. Schleid, H. Hasse, R. Glaser, Appl. Catal. A, 355(1-2) (2009) 42-49. https://doi.org/10.1016/j.apcata.2008.11.014

[52] S. Dharmarathna, C.K. King'ondu, W. Pedrick, L. Pahalagedara, S.L. Suib, Chem. of Mater. 24(4) (2012) 705-712. https://doi.org/10.1021/cm203366m

[53] I.Z. Ismagilov, E.M. Michurin, O.B. Sukhova, L.T. Tsykoza, E.V. Matus, M.A. Kerzhentsev, Z.R. Ismagilov, A.N. Zagoruiko, E.V. Rebrov, M.H.J.M. de Coon, J.C. Schouten, Chem. Eng. J. 135, (2008) S57-S65. https://doi.org/10.1016/j.cej.2007.07.036

[54] H. Liu, Y. Li, Y. Yang, Z. Shi, Q. Zhang, S. Wu, X. Zhao, Catal. Today, 326 (2019) 46-53. https://doi.org/10.1016/j.cattod.2018.07.008

[55] X. Wu, X. Yu, X. He, G. Jing, J. Phys. Chem. C, 123 (2019) 10981-10990. http://doi.org/10.1021/acs.jpcc.9b01048

[56] Y. Liu, J. Hou, Mater. Res. Bull. 118 (2019) 110497 http://doi.org/10.1016/j.materresbull.2019.110497

[57] W. Gac, G. Giecko, S. Pasieuna-Patkowska, T. Borowiecki, L. Kepinski, Catal. Tod. 137 (2008) 397-402. https://doi.org/10.1016/j.cattod.2007.11.008

[58] V.D. Makwana, Y.C. Son, A.R. Howell, S.L. Suib, J. Catal. 210 (2002) 46-52. https://doi.org/10.1006/jcat.2002.3680

[59] L. Lamaita, M.A. Peluso, J.E. Sambeth, H.J. Thomas, Appl. Catal. B, 61 (2005) 114-119. https://doi.org/10.1016/j.apcatb.2005.03.014

[60] M.A. Peluso, E. Pronsato, J.E. Sambeth, H.J. Thomas, G. Busca, Appl. Catal. B, 78 (2008) 73–79. https://doi.org/10.1016/j.apcatb.2007.09.002

[61] H. Li, G. Qi, Tana, X. Zhang, X. Huang, W. Le, W. Shen, Appl. Catal. B 103 (2011) 54–61. https://doi.org/10.1016/j.apcatb.2011.01.008

[62] H. Cao, S.L. Suib, J. Am. Chem. Soc. 116 (1994) 5334-5342. https://doi.org/10.1021/ja00091a044

[63] A. Popa, V. Sasca, J. Halasz, Appl. Surf. Sci. 255 (2008) 1830–1835. https://doi.org/10.1016/j.apsusc.2008.06.040

[64] B-S. Jiang, R. Chang, Y-C. Lin, Indus. and Eng. Chem. Res. 52 (2013) 37–42. https://doi.org/10.1021/ie300348u

[65] N.I. Ionescu, N.I. Jaeger, P.J. Plath, C. Hornoiu, J. Therm, Anal. Calorim. 91(2) (2008) 381–384. https://doi.org/10.1007/s10973-007-8465-1

[66] M.A. Campesi, N.J. Mariani, M.C. Pramparo, B.P. Barbero, L.E. Cadus, O.M. Martinez, G.F. Barreto, Catal. Today 176 (2011) 225–228. https://doi.org/10.1016/j.cattod.2011.01.009

[67] W. Zhang, J.A. Desikan, S.T. Oyama, J. Phys. Chem. 99 (1995) 14468–14476. https://doi.org/10.1021/j100039a039

[68] M. Boronat, A. Corma, F. Illas, J. Radilla, T. Rodenas, M.J. Sabater, J. Catal. 278 (2011) 50–58. https://doi.org/10.1016/j.jcat.2010.11.013

[69] V.D. Makwana, L.J. Garces, J. Liu, J. Cai, Y.-C. Son, S.L. Suib, Catal. Today 85 (2003) 225–233. https://doi.org/10.1016/S0920-5861(03)00390-0

[70] H. Tian, J. He, X. Zhang, L. Zhou, D. Wang, Micro. Meso. Mater. 138 (2011) 118–122. https://doi.org/10.1016/j.micromeso.2010.09.022
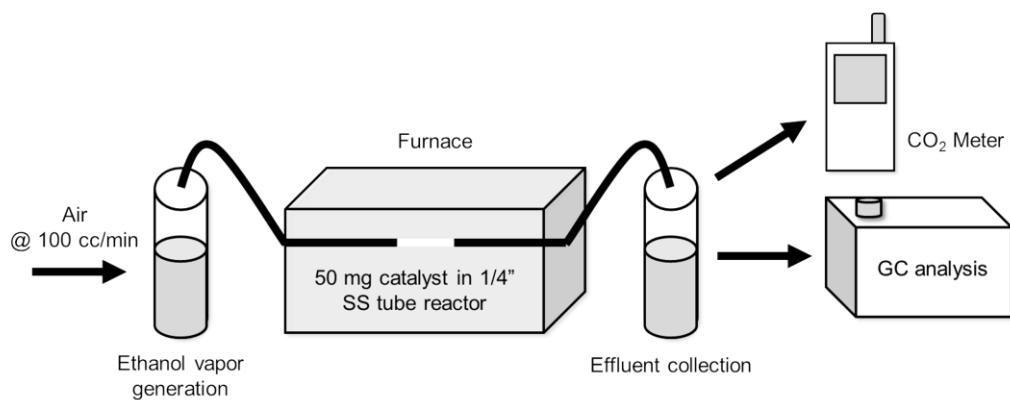
Figure 1. Schematic of reactor system for catalytic oxidation of ethanol over cryptomelane catalysts in this study.
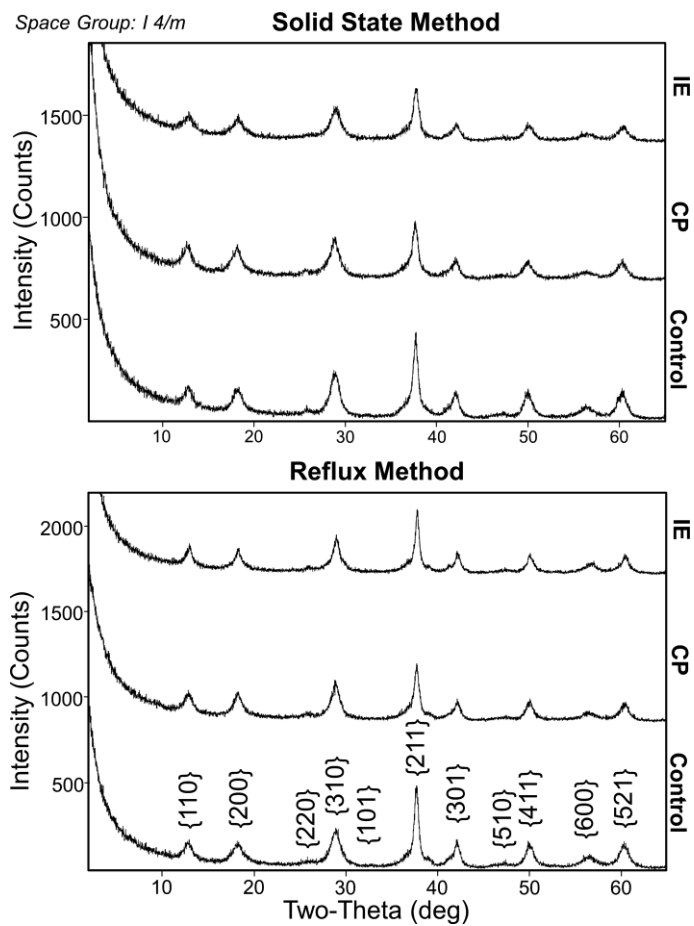
Figure 2. XRD patterns of the cryptomelane samples in this study; from top to bottom: SS-IE, SS-CP, SS-CON, R-IE, R-CP, and R-CON.
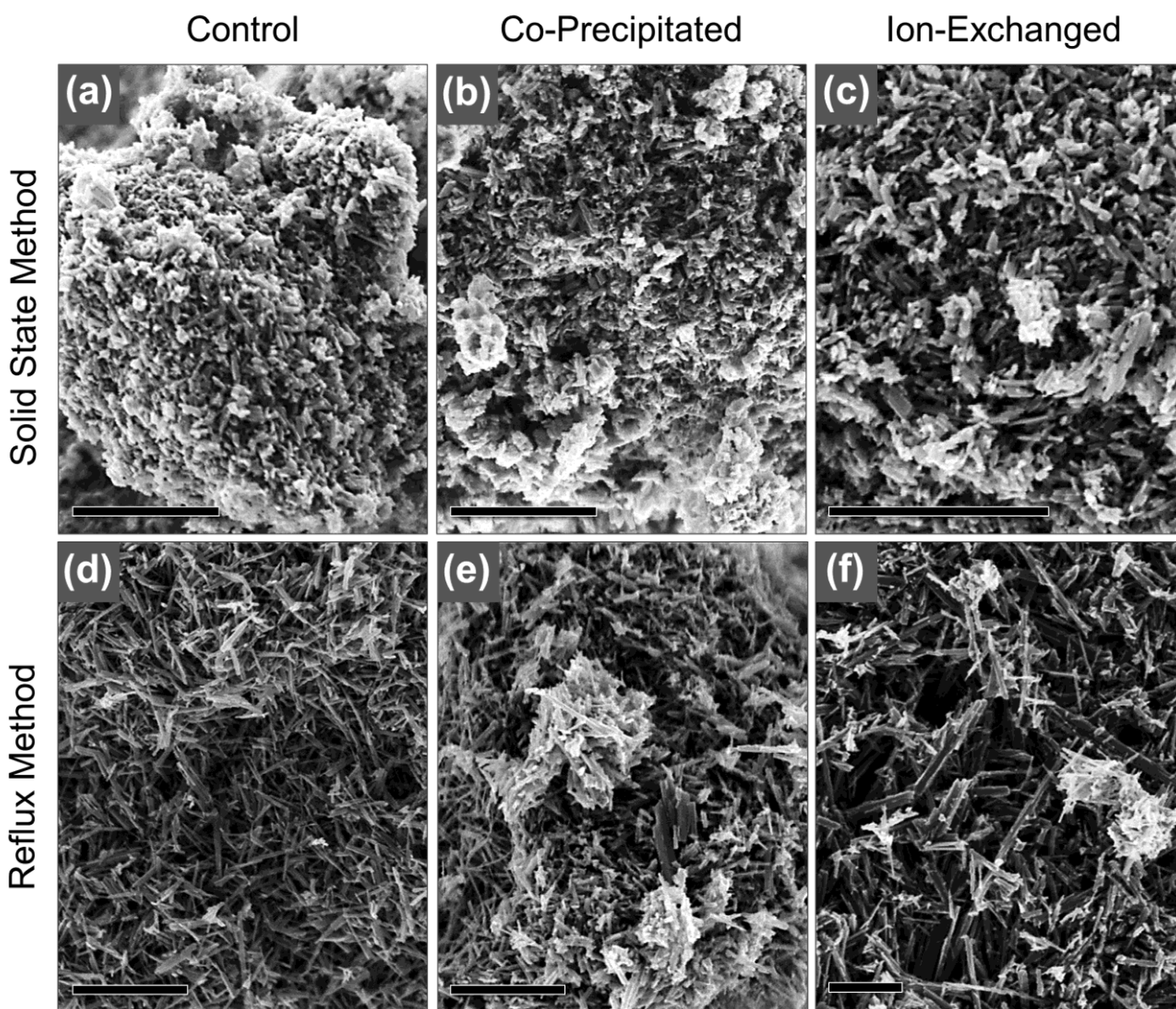
Figure 3. SEM micrographs of cryptomelane samples prepared in this study taken at 2.0 keV accelerating voltage. (a) Undoped solid state cryptomelane sample showing stubby, fibrous crystalline texture; (b) solid state cryptomelane Eu-doped by co-precipitation sample; (c) solid state cryptomelane Eu-doped by ion exchange sample; (d) undoped reflux cryptomelane sample showing uniform slender fibrous crystal texture; (e) reflux cryptomelane Eu-doped by co-precipitation sample showing wider range of crystal size and 'plaque' coating the crystals; (f) reflux cryptomelane Eu-doped by ion-exchange showing uniform, slender fibrous crystals with 'plaque' coating the crystals. Bars = 500 nm.
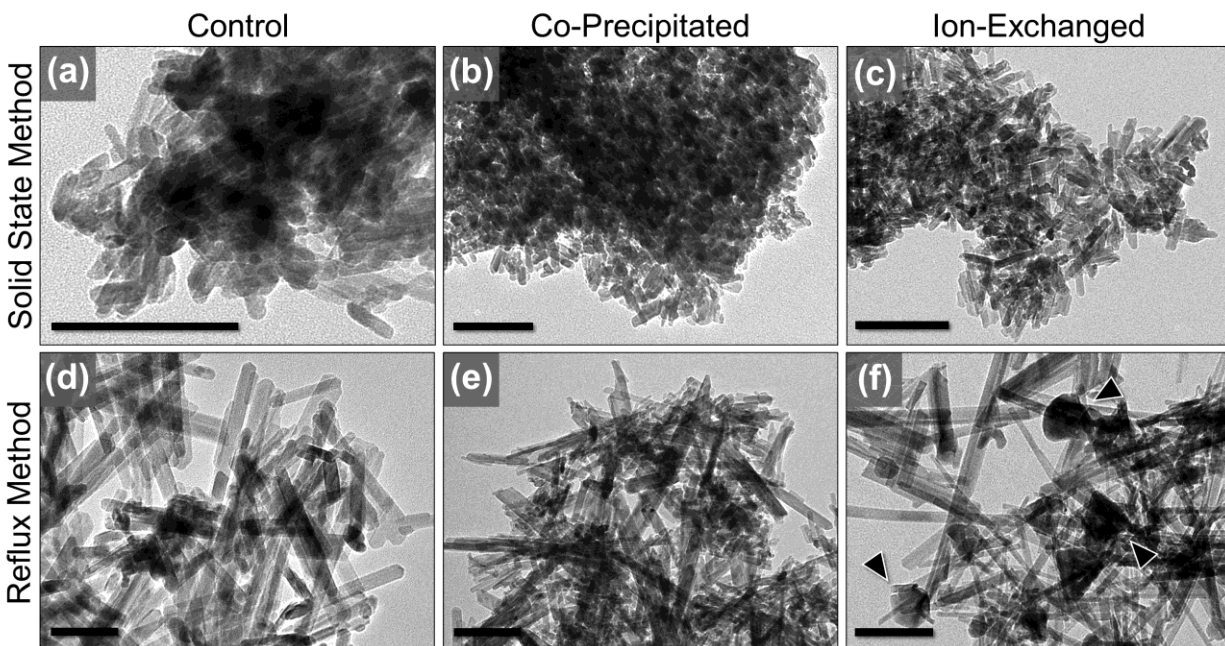
Figure 4. TEM brightfield micrographs of general micro-textures of the cryptomelane samples in this study taken at a 200 keV accelerating voltage. (a) undoped solid state cryptomelane, showing homogenously-sized subhedral short fibrous crystals, (b) solid-state cryptomelane Eu-doped by co-precipitation, showing subhedral short fibrous crystals with a minor degree of size heterogeneity, (c) solid-state cryptomelane Eu-doped by ion-exchange showing homogenous-sized subhedral short fibrous crystals, (d) undoped reflux cryptomelane showing homogenous, euhedral elongated fibrous crystals, (e) reflux cryptomelane Eu-doped by co-precipitation showing euhedral elongated fibrous crystals of moderately varying size, (f) reflux cryptomelane Eu-doped by ion-exchange showing multi-phase composition of elongated euhedral fibrous crystals of moderately varying size intimately associated with equant square and hexagonal crystals interpreted as the mineral bixbyite (indicated with arrows). Bars = 100 nm.
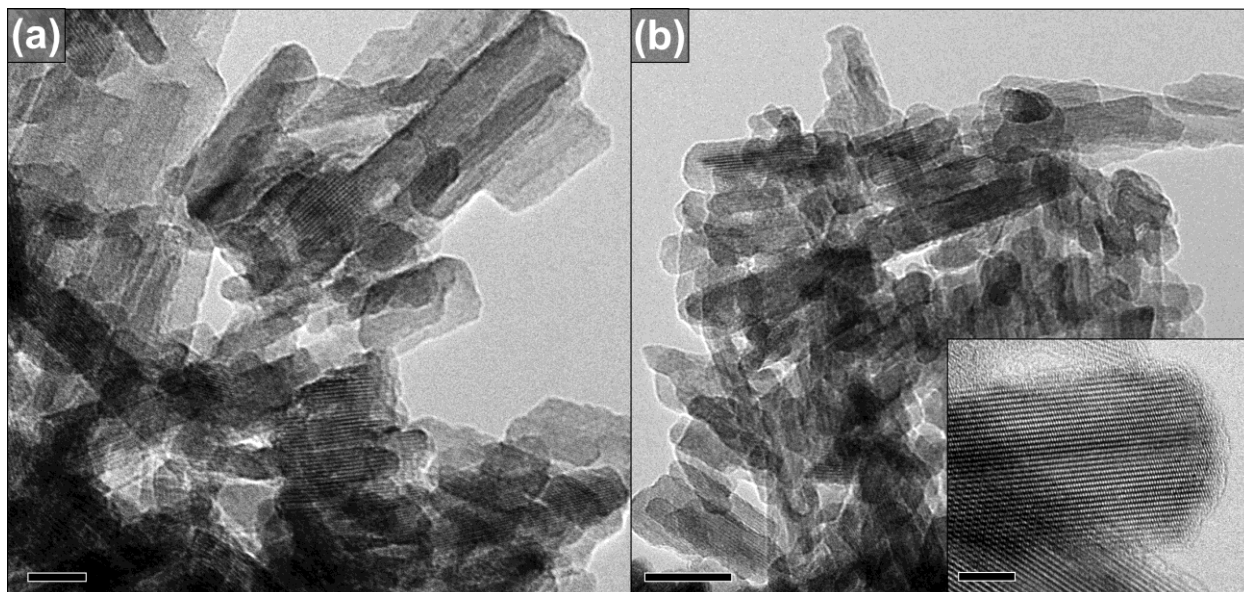
Figure 5. TEM brightfield micrographs of sample SS-IE showing degraded crystal surface texture. (a) image showing uneven crystal surface texture of SS-IE in one region; bar = 10 nm; (b) image of another region of SS-IE showing more of the uneven surface texture; bar = 20 nm; (b-inset) image showing defect-free atomic detail of the {200} planes; Bar = 5 nm.
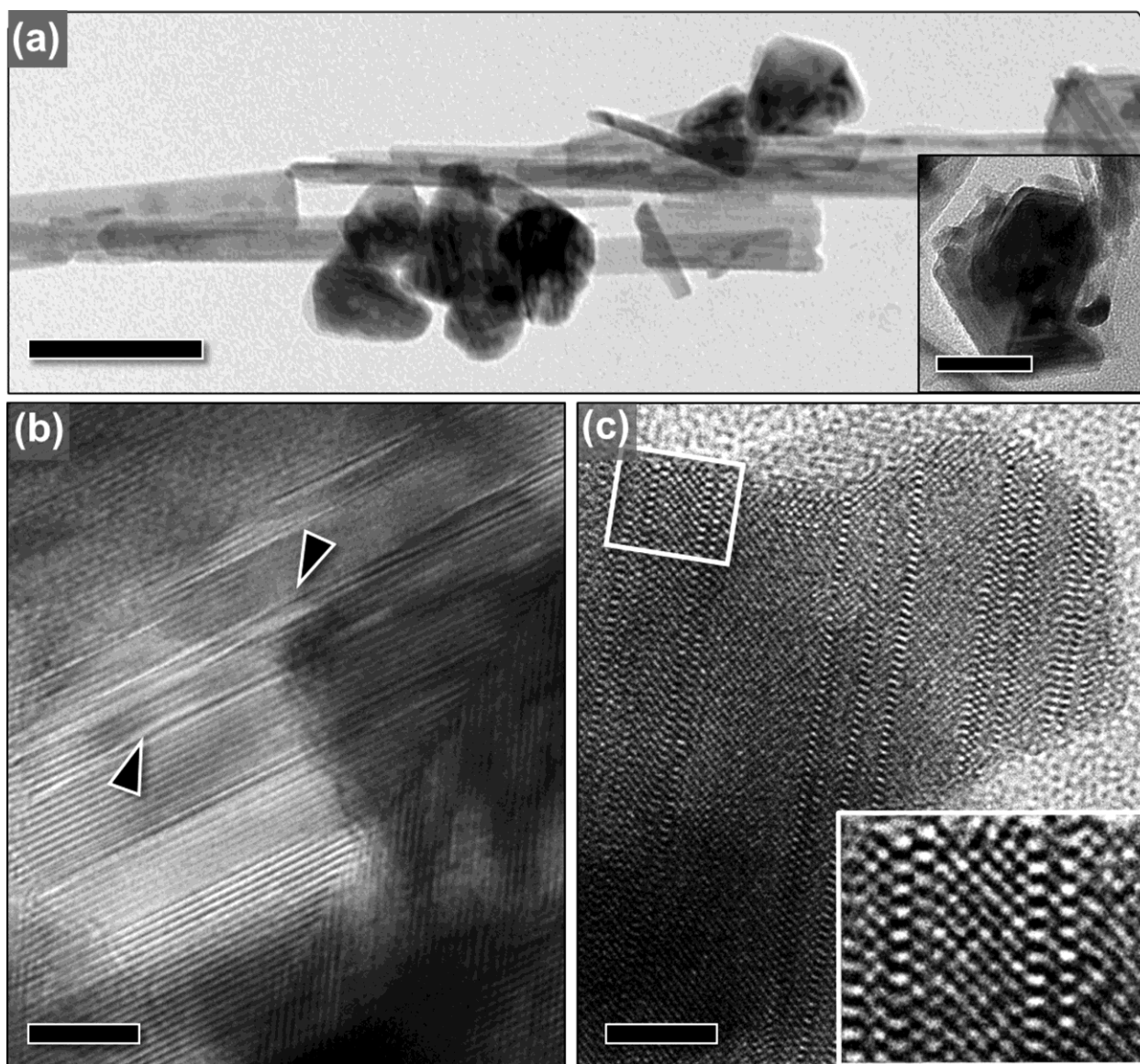
Figure 6. Brightfield TEM micrographs showing detailed data of the Eu-bixbyite crystals found throughout sample R-IE. (a) Image of R-IE showing textural relationship between the fibrous cryptomelane crystals and bixbyite crystals in random orientations bar = 100 nm (inset is image of a Eu-bixbyite crystal as viewed in the <222> direction. bar = 10 nm); (b) lattice fringe image of an R-IE cryptomelane crystal showing linear, lenticular defects parallel to the c-axis (indicated by arrows) bar = 10 nm; (c) image showing near atomic detail of one of the Eu-bixbyite crystals as viewed parallel to a, b, or c axes (equivalent) Bar = 5 nm (detail inset shows width disorder structural variation interpreted as single and double Mn octahedra rows).
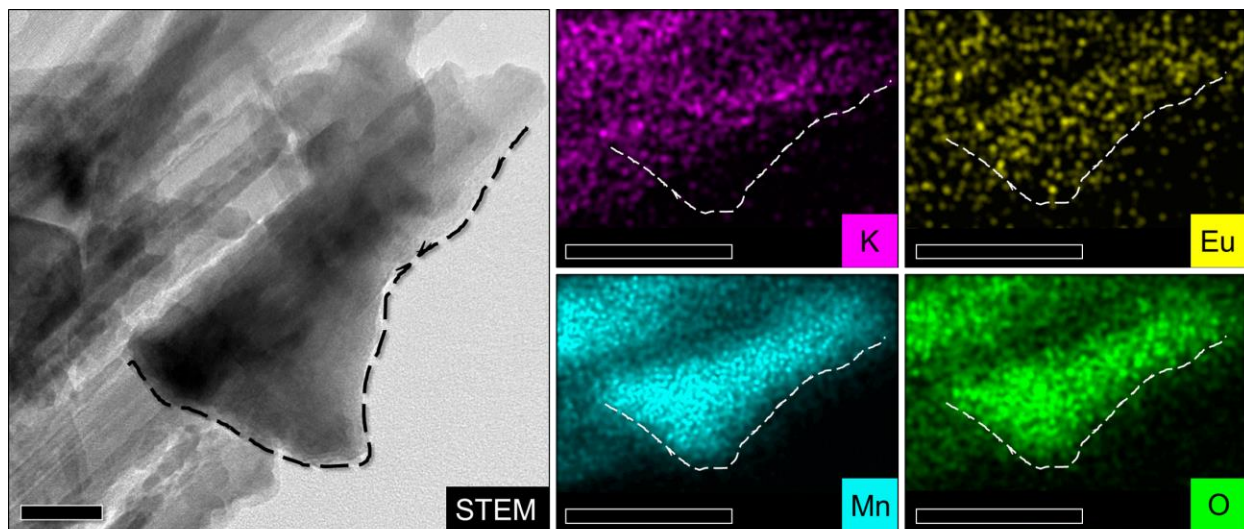
Figure 7. STEM-XEDS maps of R-IE showing interface between an elongated fiber of cryptomelane and a triangular-shaped crystal of Eu-bixbyite (outlined with dashes); note the absence of K in the bixbyite crystal relative to the rest of the region. Bars = 100 nm
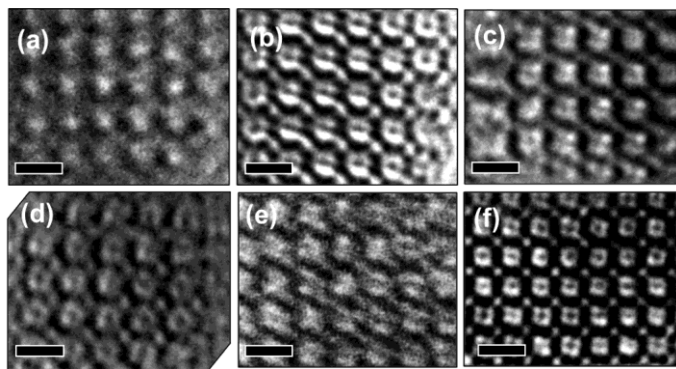
Figure 8. Brightfield TEM micrographs showing the view down the tunnel axis in each species to demonstrate crystallinity and symmetry. (a) SS-CON, (b) SS-CP, (c), SS-IE, (d) R-CON, (e) R-CP (some astigmatism present), and (f) R-IE. Bars = 1 nm. Variations in image features are partially caused by variation in sample thickness and defocus values which are difficult to control in a particulate mount. All images show coherence of the crystal structure at the nanoscale to near-atomic resolution.
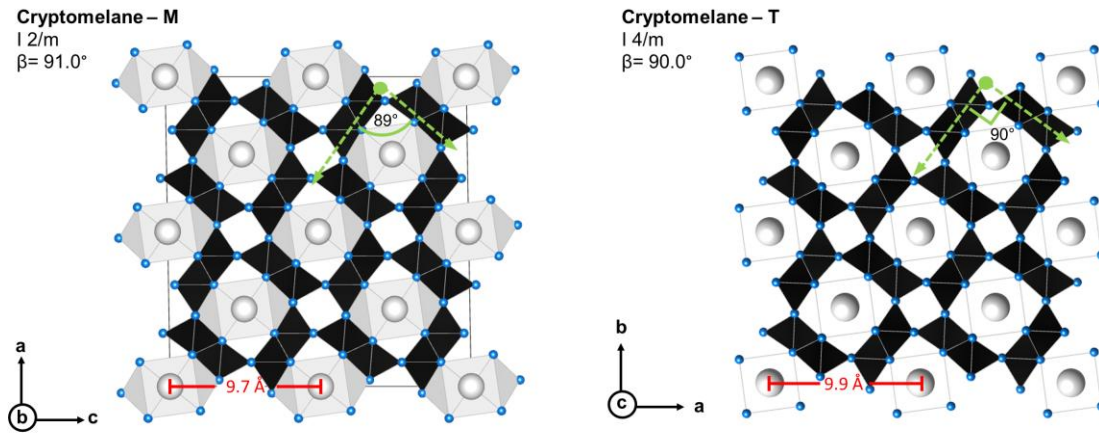
Figure 9. Polyhedron models of the cryptomelane crystalline monoclinic and tetragonal polymorph crystal structures
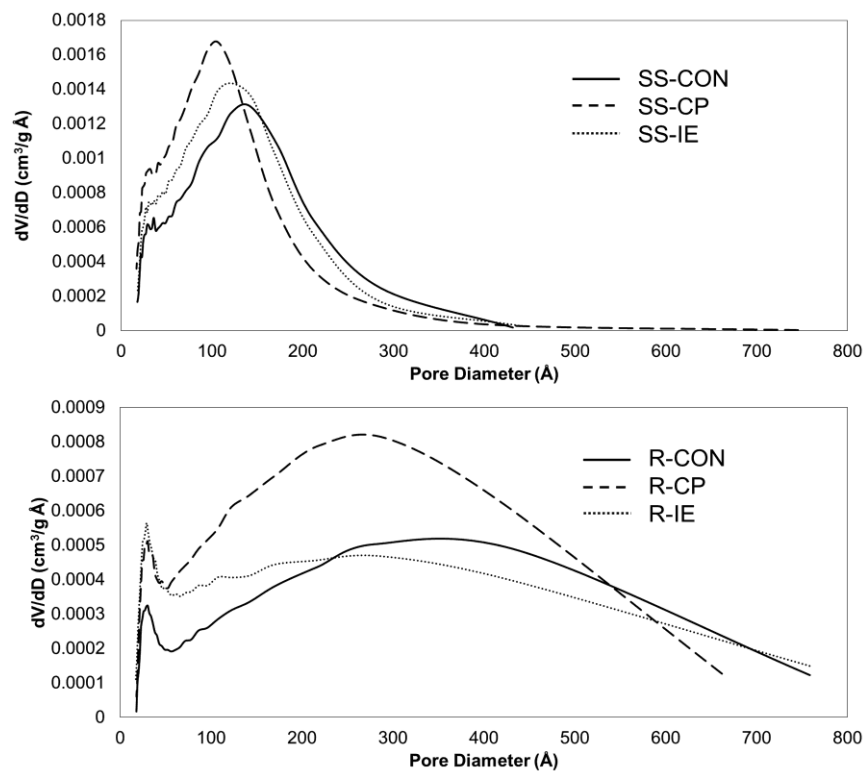
Figure 10. Mesopore size distribution curves for the cryptomelane samples; solid state samples (top), reflux samples (bottom).
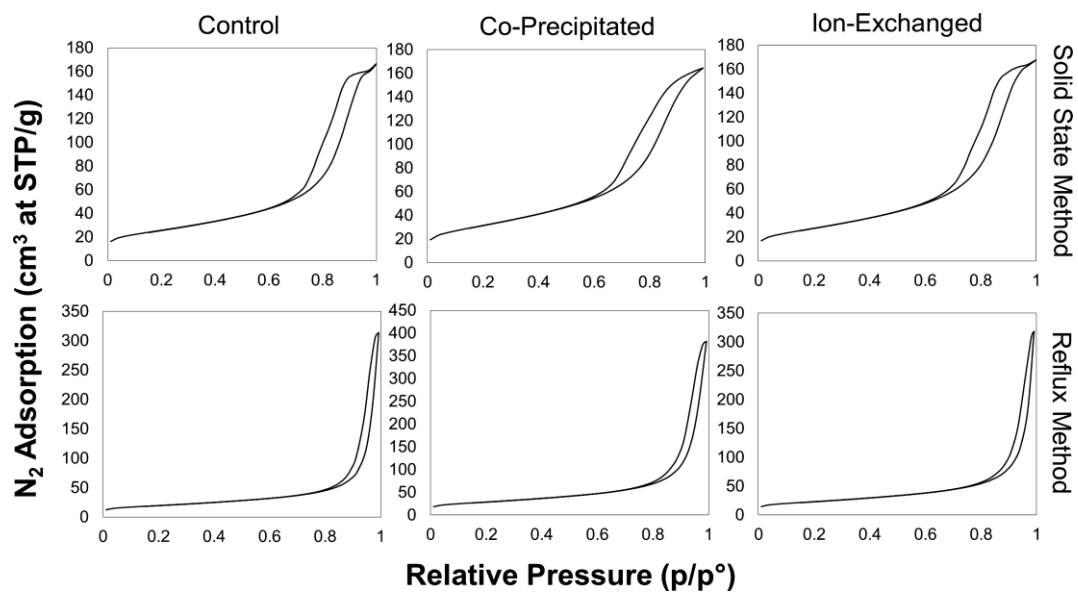
Figure 11. Nitrogen adsorption-desorption isotherms of the cryptomelane samples in this study.
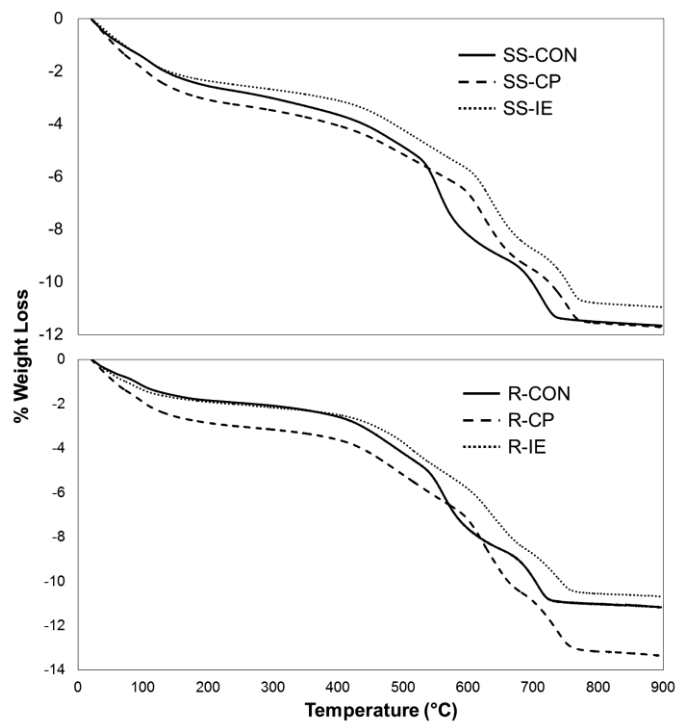
Figure 12. Thermogravimetric analysis results shown as percent weight loss as a function of temperature of the cryptomelane samples in this study; solid state samples (top) and reflux samples (bottom).
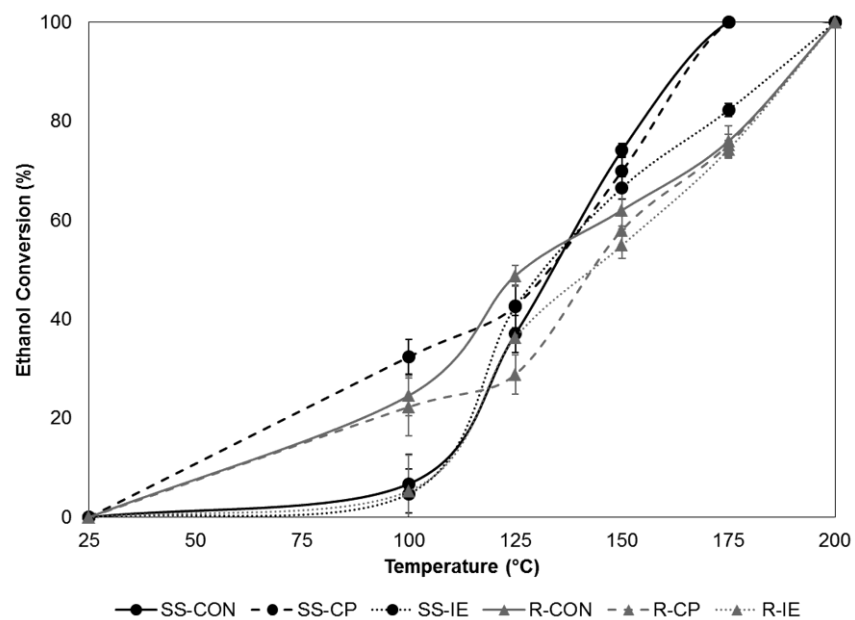
Figure 13. Ethanol conversion percentages at temperatures between 25 °C and 200 °C for each catalyst in this study. Error bars reflect one standard deviation.
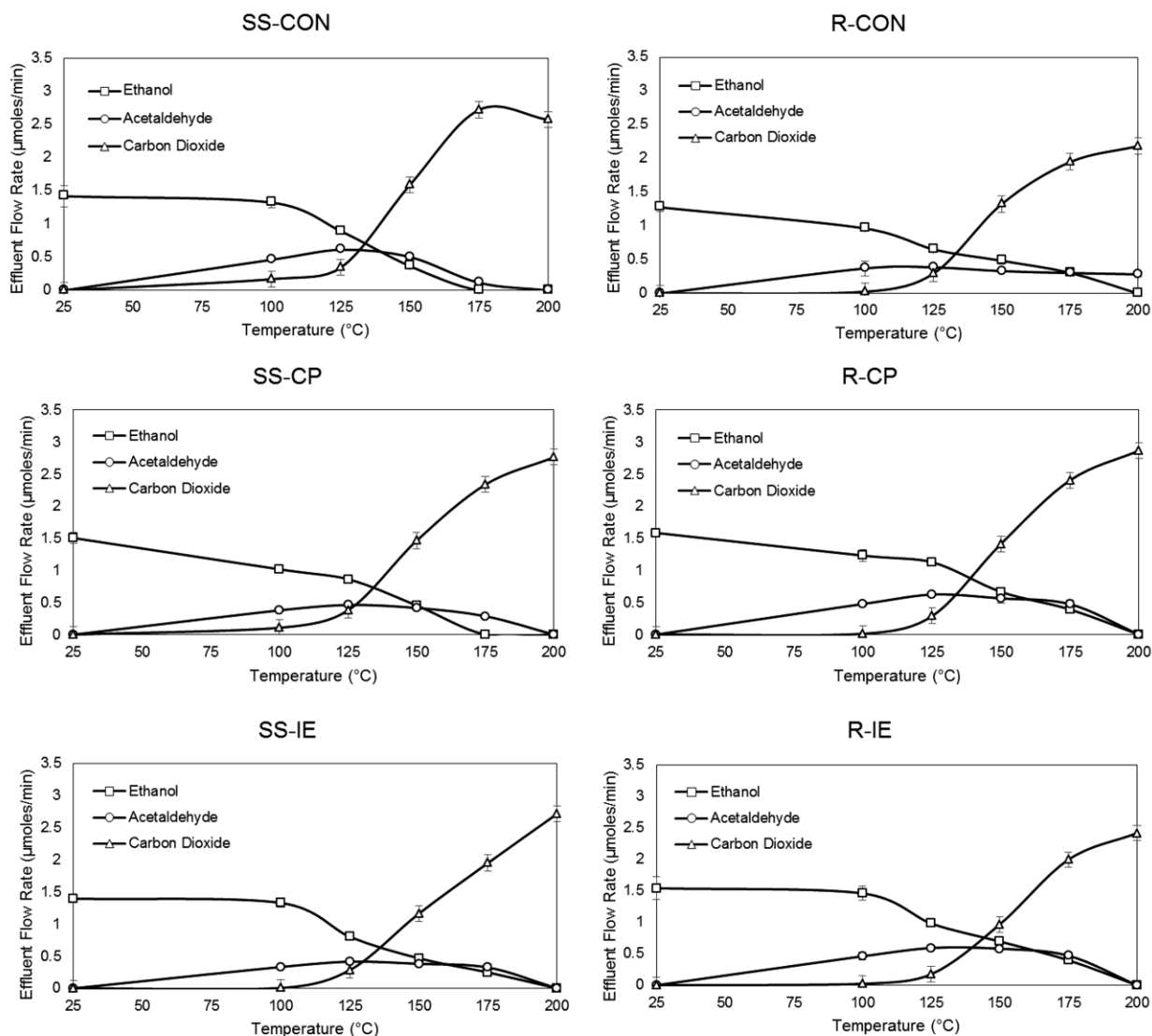
Figure 14. Effluent species (ethanol, acetaldehyde, and carbon dioxide) flow rate measured between 25 °C and 200 °C for each catalyst in this investigation. Error bars for ethanol and acetaldehyde reflect one standard deviation and carbon dioxide error bars reflect rated instrument accuracy (± 30 ppm).

Table 1. Summary of surface area, pore volume, bulk densities, and crystallite size in cryptomelane samples in this study.

Cryptomelane Sample	BET Surface Area (m^2/g)	[a] Pore Volume (cm^3/g)	[b]Pore Volume in Macropores (%)	Bulk Density (g/mL)	[c]Crystal Length Range (nm)	[c]Crystal Width Range (nm)
SS-CON	92.0 ± 0.4	0.2 ± 0.0	-nd-	1.0 ± 0.1	20-80	5-10
SS-CP	115.7 ± 0.5	0.3 ± 0.0	2.4 ± 0.6	1.0 ± 0.1	20-60	5-15
SS-IE	97.1 ± 0.4	0.3 ± 0.0	-nd-	1.0 ± 0.1	20-60	5-10
R-CON	79.6 ± 0.5	0.6 ± 0.1	47.0 ± 2.2	0.6 ± 0.2	100-1500	10-50
R-CP	99.4 ± 0.4	0.6 ± 0.1	44.5 ± 10.7	0.6 ± 0.2	25-300	5-30
R-IE	70.4 ± 0.3	0.4 ± 0.1	52.5 ± 7.7	0.5 ± 0.0	50-2000	10-40

[a]BJH adsorption cumulative volume of pores between 17 Å and 3,000 Å.

[b]Cumulative BJH adsorption.

[c]Measured from TEM data – approximate values.

Table 2. Summary of elemental composition for cryptomelane samples in this study.

Cryptomelane Sample	[a]Elemental Composition (At.%)				Eu/Mn Atomic Ratio
	Mn	K	O	Eu	
SS-CON	32.5 ± 3.2	3.6 ± 0.3	64.0 ± 3.5	-nd-	
SS-CP	22.3 ± 0.8	3.6 ± 0.2	69.1 ± 1.1	5.0 ± 0.2	0.2
SS-IE	29.2 ± 2.0	3.3 ± 0.2	66.7 ± 2.3	0.8 ± 0.1	< 0.1
R-CON	32.2 ± 2.9	3.7 ± 0.6	64.1 ± 3.5	-nd-	
R-CP	28.7 ± 3.5	3.5 ± 0.3	67.2 ± 3.8	0.7 ± 0.1	< 0.1
R-IE	27.1 ± 1.3	3.3 ± 0.6	69.0 ± 1.6	0.6 ± 0.1	< 0.1

[a]Standard-less quantification

Table 3. Summary of ELNES values for Mn in cryptomelane samples in this study as determined by EELS.

Cryptomelane Sample	[a]Energy Mn-L_3 (eV)	[a]Energy Mn-L_2 (eV)	[b]ΔE(Mn L_2-L_3) (eV)
SS-CON	642.4	653.0	10.6
SS-CP	642.6	653.2	10.6
SS-IE	645.5	656.3	10.8
R-CON	644.4	654.6	10.2
R-CP	643.4	654.2	10.8
R-IE	638.0	649.1	11.1
Eu-Bixbyite	641.0	651.4	10.4

[a]Mn-$L_{2,3}$ white-line peak$_{(max)}$ positions [38]
[b]Spin-orbital splitting between Mn-$L_{2,3}$ white lines [38]

Table 4. Summary of weight changes in the cryptomelane samples as a function of temperature from TG analysis.

Cryptomelane Sample	Weight Loss (% of initial mass)					
	Temp < 200 °C	200 °C ≤ T ≤ 500 °C	500 °C ≤ T ≤ 700 °C	Temp > 700 °C	Total 200 °C ≤ T ≤ 900 °C	Total Temp < 900 °C
SS-CON	2.6 ± 0.1%	2.3 ± 0.1%	5.1 ± 0.2%	1.7 ± 0.1%	9.0 ± 0.4%	11.6 ± 0.5%
SS-CP	3.2 ± 0.1%	2.1 ± 0.1%	4.4 ± 0.1%	2.2 ± 0.1%	8.6 ± 0.2%	11.7 ± 0.3%
SS-IE	2.3 ± 0.2%	1.8 ± 0.1%	4.6 ± 0.1%	2.2 ± 0.1%	8.5 ± 0.3%	10.8 ± 0.5%
R-CON	1.8 ± 0.0%	2.1 ± 0.5%	5.6 ± 0.2%	1.5 ± 0.3%	9.1 ± 1.0%	10.9 ± 1.0%
R-CP	2.7 ± 0.4%	2.0 ± 0.5%	5.3 ± 0.6%	2.5 ± 0.1%	9.7 ± 1.2%	12.3 ± 1.6%
R-IE	1.7 ± 0.3%	1.5 ± 0.5%	4.8 ± 0.4%	2.4 ± 0.6%	8.6 ± 1.6 %	10.3 ± 1.8%

Table 5. Observed reaction rates at 150 °C, activation energies, and T_{50} and T_{90} values calculated for each cryptomelane sample.

Cryptomelane Sample	Reaction rate (μmol/min*g cat) at (inlet ethanol concentration)	Reaction rate (μmol/min*m^2 cat) at (inlet ethanol concentration	Activation energy (kJ/mole)	T_{50} (K)	T_{90} (K)
SS-CON	40.5 (350 ppm)	0.44 (350 ppm)	78.2	406	435
SS-CP	39.2 (370 ppm)	0.34 (370 ppm)	32.0	405	438
SS-IE	35.7 (340 ppm)	0.37 (340 ppm)	74.9	403	458
R-CON	29.8 (310 ppm)	0.37 (310 ppm)	26.9	407	463
R-CP	36.0 (390 ppm)	0.36 (390 ppm)	43.2	416	463
R-IE	31.6 (380 ppm)	0.45 (380 ppm)	133.7	416	463

CHAPTER 3

EFFECTS OF Mn(II) AND Eu(III) CATION EXCHANGE IN SEPIOLITE/TiO$_2$ NANOCOMPOSITES IN THE PHOTOCATALYTIC DEGRADATION OF ORANGE G

1. Introduction

Dyes are a major component of the waste stream generated by the textile industry. Many industrial dyes and their raw materials are known to be toxic, posing a significant hazard to the environment into which dye-containing wastewater is disposed (Konstantinou and Albanis, 2004; Teh and Mohamed, 2011). Because dyes of a synthetic origin can be persistent even with traditional wastewater treatment techniques, many novel methods have been developed to degrade these compounds more effectively (Shaul et al., 1991; Tünay et al., 1996; Fernández et al., 2010; Teh and Mohamed, 2011). One of these methods is decolorization by semiconductor photocatalysis and one of the most popular photocatalysts for dye degradation is titanium dioxide (TiO_2, 'titania') as it is a stable, inexpensive, and non-toxic material (Konstantinou and Albanis, 2004).

Due to its wide band gap energy (3.2 ev), TiO_2 functionality as a photocatalyst requires ultraviolet radiation (UVR). Efforts to modify TiO_2 for visible spectrum activity have been extensive and ongoing since the mid 1980's; this enormous body of work has been reviewed over the past 35 years by Linsebigler et al. (1995), Rehman et al. (2009), Kumar and Devi (2011), Daghrir et al. (2013), Park et al. (2013), Bo et al. (2015), Ghosh and Das, (2015), Humayun et al. (2018), and Basavarajappa et al. (2020); however, opportunities to address activity challenges under UVR still remain. The two primary limitations in UVR-driven TiO_2 photocatalytic reactions are the limited quantum yield due to the high rate of electron-hole pair recombination and tendency to sinter, reducing specific surface area. Various strategies have been developed to address the high recombination rate of photogenerated electrons and holes, one of which has been to dope TiO_2 with certain transition metals, such as iron (Sun et al., 2009; Asilturk et al., 2009), copper (Chen et al., 2009), and vanadium (Tian et al., 2009) or with rare earth metals such as holmium (Shi et al., 2009), neodymium (Xu et al., 2009), and cerium (Fan et al., 2006). These dopants promote charge-carrier separation in TiO_2 by trapping charge, enhancing the reaction by maintaining available free hydroxyl radicals and active oxygen species.

Another challenge associated with TiO_2 use is deactivation by sintering, in which dispersed populations of small catalyst particles migrate and coalesce, decreasing the specific surface area, lowering the photocatalytic activity. This limitation has been addressed by

combining TiO₂ with a supportive composite that helps inhibit this phenomenon. Supports used for this purpose include synthetic materials such as carbon nanotubes (Yen et al., 2008, Gao et al., 2009), graphene (Williams et al., 2008), and organic polymers (Zhang et al., 2006, Wang et al. 2008). Phyllosilicate minerals such as montmorillonite (Tahir and Amin, 2013), halloysite (Papoulis et al., 2010), hectorite (Kibanova et al., 2009), kaolinite (Kibanova et al., 2009), palygorskite (Papoulis et al., 2010), and sepiolite (Zhou et al. 2018; Uğurlu and Karaoğlu, 2011) have also been investigated as supports for TiO₂.

Although there is abundant work on direct TiO₂ doping alone or in combination with supportive compositing, there is little work on modification of the substrate itself to directly promote the catalytic activity. Cation exchange has been shown to modify the net surface charge of clay minerals and a recent study by Papoulis et al. (2019) investigated the role of cation exchange of Cu and Zn on sepiolite-TiO₂ nanocomposites for gas phase photocatalysis under UVR. The authors found that photocatalytic activity was enhanced in Zn-exchanged sepiolite/TiO₂ due to the combined effect of agglomeration inhibition by the sepiolite and, they hypothesize, the in-situ formation of ZnO complexes on the support surface, which acted as a co-catalyst. However, they found that Cu-exchanged sepiolite/TiO₂ had lower catalytic activity, potentially due to enhancing recombination and a narrowing of the band gap energy.

In this investigation, the concept of modification of the phyllosilicate substrate is explored further and under different conditions. Here, europium and manganese-exchanged sepiolites are produced and used as a substrate for TiO₂ growth and deposition. Of interest are the potential different behaviors of Eu- and Mn-exchanged sepiolite compared to the Zn- and Cu-exchanged sepiolites prepared by Papoulis et al. (2019) with respect to photocatalytic activity. The catalysts were evaluated in the aqueous phase photocatalytic degradation of the azo dye, Orange G. Orange G was chosen as a model compound because azo dyes represent more than 50% of the textile dyes on the market today (Konstantinou and Albanis, 2004); these dyes and their precursors are suspected to be human carcinogens because they can form toxic aromatic amines. (Stylidi et al., 2003; Gomes da Silva and Faria, 2003; Brown and De Vito, 2009).

Mn and Eu are selected as exchange cations because both have been used as direct-TiO₂ dopants with positive results with respect to photocatalytic activity. Mn-doped TiO₂ has been shown to have a red-shifted absorption gap and high photocatalytic activity for methylene blue

dye degradation relative to undoped TiO_2 (Deng et al., 2011; Binas et al., 2012; Chauhan et al., 2012) and Eu has been shown to promote photocatalytic activity in TiO_2 for various volatile organic compound degradations as a direct single-dopant (Xiaohong et al., 2007; Khade et al., 2017; Zhang et al., 2003) and as a co-dopant with Fe (Diamandescu et al., 2008) and Ho and Nd (Reszczynska et al., 2014). Eu-doped TiO_2 was also recently composited with sepiolite for Orange G degradation, showing the highest photocatalytic activity improvement among the lanthanides investigated (Zhou et al., 2019).

2.   Materials and Methods

2.1   *Preparation of the photocatalysts*

Sepiolite powders prepared by first treating 5 g of sepiolite powder (Sigma-Aldrich) in a solution of double-distilled deionized water and glacial acetic acid (pH = 4.5) to enhance ion exchange capacity. The acid-treated sepiolite samples were exchanged with manganese(II) chloride (Sigma Aldrich) and europium(III) nitrate hexahydrate (Alfa Aesar) to produce Mn-sepiolite and Eu-sepiolite, respectively. Mn-sepiolite was prepared by stirring sepiolite in a 0.2 M solution of $MnCl_2$ for a period of time, centrifuging between treatments. Eu-sepiolite was prepared by stirring sepiolite in 0.1 M solution of $Eu(NO_3)_3 \cdot 6H_2O$ for a period of time, centrifuging between treatments. Ion-exchanges were repeated five times with fresh solution added each time. Samples were rinsed repeatedly with double-distilled deionized water until no trace of anions remained. The sepiolite samples were then dried in an oven at 65 °C and ground into a powder in a mortar.

Sepiolite/TiO_2 nanocomposites were produced by a sol-gel method. TiO_2 was deposited on the sepiolite by in situ hydrolysis of titanium(IV) butoxide (Sigma Aldrich) following a method similar to that used by Zhang et al. (2011). The first step was to add 11.50 g of $Ti(OBu)_4$ to 5 g of sepiolite powder under stirring. Next, 100 ml of double-distilled deionized water was added dropwise to hydrolyze the $Ti(OBu)_4$. This mixture was aged under vigorous stirring for 4 h. The mixture was then centrifuged, washed repeatedly with double distilled deionized water, filtered, dried at 80 °C overnight, and finally calcined at 300 °C for 4 h in air. After grinding, the resultant powders were labelled Mn-Sep$_{Ti}$, and Eu-Sep$_{Ti}$. As a comparative, an unexchanged sepiolite/TiO_2 nanocomposite was produced by the same method, designated Con-Sep$_{Ti}$. A

photograph of each of the prepared photocatalysts is shown in Fig. 1; Con-Sep$_{Ti}$ and Eu-Sep$_{Ti}$ were both the same beige-white color, but Mn-Sep$_{Ti}$ was tan in color.

2.2   *Physical and chemical characterization of the photocatalysts*

Prepared catalysts were characterized by powder X-ray diffraction (XRD) to determine the crystal structure, by transmission electron microscopy (TEM) to determine nanoscale textures and morphology, by scanning transmission electron microscopy-energy dispersive spectroscopy (STEM-EDS) to determine elemental distribution and abundance, nitrogen adsorption to determine the surface area and pore geometry, and UV-Vis diffuse reflectance spectroscopy to determine the band gap energy (E_g). XRD patterns were collected using a Scintag Pad X-1 powder diffractometer to identify mineral phases within the samples. The sample powders were mounted onto pack-mount slides and analyzed in the 2θ range 2-60° in 0.02° steps with a 3.0 s dwell time using monochromated Cu Kα radiation (1.5418 Å), operating at 40 kV and 35 mA. The data were analyzed using Jade 7 software. The nature of the nanoscale textures and elemental distribution were examined using a JEOL JEM-2100 scanning transmission electron microscope (TEM/STEM) operated at 200 keV with a LaB$_6$ source and equipped with a Gatan Orius SC200D camera, a JEOL BF STEM detector and a Bruker Quantax 200 STEM EDS system. Standardless elemental quantification was used to report normalized mass percentages for select regions of interest (ROI) within the STEM-EDS hypermaps produced for each sample; these numerical data were derived from routine P/B-ZAF correction with series-fit deconvolution and background subtraction. Samples for TEM were prepared via particulate suspension applications to 3.0 mm lacey carbon-coated copper grids. The BET surface area and adsorption-desorption isotherms for each sample were measured by nitrogen adsorption at 77 K using a Micrometrics Tri-Star II BET surface area analyzer. Prior to analysis, the samples were degassed for 30 min at 150 °C with a helium purge.

2.3   *Photoactivity testing of modified sepiolite/TiO$_2$ nanocomposites*

The prepared nanocomposites were evaluated for photocatalytic activity in degradation of Orange G (OG) under UV irradiation. The experiment was carried out in a continuously-stirred 400 mL aluminum-jacketed Pyrex beaker; the reaction cell volume (275 ml) was continuously bubbled with air at 80 ccpm. The irradiation source was a 26 W UV-A/B CFL bulb (1150 µW/cm^2 UV-A and 195 µW/cm^2 UV-B) suspended 3.0" above the slurry, delivering ≥ 4340 lx to

the surface, the slurry was maintained at room temperature. The initial concentration of OG in the reactor was 2.0×10^{-5} M and the catalyst loading was 1.0 g/L for all experiments. The reaction cell was stirred for 30 min prior to irradiation to ensure adsorption equilibrium had been achieved and the reaction was run for a total of 8 hrs. At defined time intervals, 3 mL of solution was removed from the cell. These aliquots were divided, centrifuged, and analyzed using a Thermo Fisher Genesys 10 visible light spectrophotometer at 480 nm and compared to a prepared concentration standard to determine the concentration of OG. Each reaction was performed in triplicate and all absorbance measurements performed in duplicate. Dark runs (catalyst + dye with no irradiation) were done to ensure that any direct oxidation of OG by the catalysts was assessed and light runs (dye + irradiation with no catalyst) were done to ensure any photolysis was assessed.

OG degradation reactions were also carried out in duplicate using UV-C irradiation in order to determine if changes in photolysis properties were present as a function of material alteration by cation exchange. Azo dyes are known to degrade in high energetic UV-C irradiation and it is of interest to understand if cation exchange also impacted this. This reaction was carried out in a polycarbonate-acrylic tube reactor which was cooled from the outside. The irradiation source was an 18 W twin-tube PLT UV-C CFL (λ=254 nm) that was fully submerged in the slurry. The reaction was maintained for 120 min. All other parameters remain the same as stated above for the UV-A/B irradiated reactions.

3. Results

3.1 Synthesis products

Following synthesis, it was noted that Mn-Sep$_{Ti}$ was a darker color than both Con-Sep$_{Ti}$ and Eu-Sep$_{Ti}$ (Fig. 1). This darkening of the material may indicate that an oxidation reaction involving Mn may have occurred during the anatase crystallization step because the precursor did not exhibit this color change.

3.2 X-ray Diffraction

The powder X-ray diffraction patterns of the nanocomposites synthesized in this study are shown in Fig. 2. Sepiolite (PDF#01-075-1597) and anatase (PDF#01-073-1764) were the only mineral phases detected in all materials. The TiO$_2$ polymorph, rutile, was not detected. The

major identifying reflections are labeled with their respective Miller indices (*hkl*) in Fig. 2. Compared to raw sepiolite, all catalysts show a <1.0° 2-theta shift in the (110) reflection. This shift is most likely from the calcination process as the sepiolite samples that were cation-exchanged and analyzed prior to TiO_2 deposition and subsequent calcination did not exhibit this shift, as shown on the right inset of Fig. 2. In addition, reflections of the nanocomposites were overall diminished in intensity compared to raw sepiolite, potentially due to signal obfuscation from intimately associated anatase nanoparticles. No evidence of a Mn-oxyhydroxide phase was detected in Mn-Sep$_{Ti}$ indicating that the dark material is either amorphous or in concentrations below resolving power.

3.3   Brightfield TEM and STEM-EDS hypermapping

The sepiolite fibers were imaged with TEM prior to any treatment in order to assess the general character of the material (Fig. 3a); sepiolite occurred as bundles of fibers 500-1500 nm long with individual fibers being 10-100 nm in width. The observed general textures of Con-Sep$_{Ti}$, Mn-Sep$_{Ti}$, and Eu-Sep$_{Ti}$ were very similar to one another with respect to the dimensionality of the sepiolite and the titania nanoparticles, which were a uniform 5-10 nm in diameter. However, although good dispersion of titania nanoparticles was observed on all three nanocomposite samples (Fig. 3b-d), both Mn-Sep$_{Ti}$ and Eu-Sep$_{Ti}$ displayed significant agglomeration of nanoparticles in many regions examined addition to dispersed nanoparticle areas (Fig 3e-f). The titania nanoparticles themselves were of good crystallinity, as shown in atomic-scale imaging and selected area electron diffractograms (SAED) (Fig. 4a-b).

Elemental composition hypermaps produced with STEM-EDS of Con-Sep$_{Ti}$ show the dispersion of titania on sepiolite, as observed from the congruous spatial distribution of Ti and Si (Fig. 5a-c). Mn-Sep$_{Ti}$ and Eu-Sep$_{Ti}$ were observed to have far more regions of Ti-poor sepiolite with associated Si-poor titania nanoparticle agglomerates (Fig 5d-f and g-i), showing the limited dispersion of TiO_2 on sepiolite in these samples. Hypermaps of Con-Sep$_{Ti}$ showing spatial distribution of Mn and Eu show absence of both on the control (Fig. 5j). Hypermaps showing the spatial distribution of Mn on Mn-Sep$_{Ti}$ show that Mn is homogeneously distributed in both sepiolite- and titania-bearing regions (Fig. 5k). Hypermaps showing the spatial distribution of Eu on Eu-Sep$_{Ti}$, in contrast, show that Eu is strongly associated with the titania regions and not the sepiolite (Fig. 5l). The spectra of regions of interest (ROI) of sepiolite crystals and titania

nanoparticles in each hypermap were used in quantification of elements in those regions to assess the relative abundances (normalized mass percentage), reported in Table 1 (Fig. 5a,d,g).

Raw sepiolite contained trace Cr and Fe, which are inherent to the commercial locality it was mined from (Amargosa Desert, NV) but are otherwise consistent with sepiolite composition ($Mg_4Si_6O_{15}(OH)_2 \cdot 6H_2O$); titanium is not observed until after deposition of TiO_2 and Al present may substituting for Si. Consistent with the hypermap data, Mn is present on both sepiolite-bearing regions (0.7 wt%) and nanoparticle-bearing regions (0.3 wt%) whereas Eu was detected only in nanoparticle-bearing regions (0.3 wt%).

3.4   Nitrogen adsorption-desorption and BET surface area

The BET surface areas of the nanocomposite catalysts produced in this study are summarized in Table 2. Raw sepiolite has a specific surface area of 275.1 m^2/g. Cation exchange with Mn did not affect surface area significantly (279.1 m^2/g); however, Eu caused some surface area loss (256.9 m^2/g). Following TiO_2 deposition, all materials experienced reduced surface area. The surface areas of Con-Sep$_{Ti}$, Mn-Sep$_{Ti}$, and Eu-Sep$_{Ti}$ were 236.5 m^2/g, 262.8 m^2/g, and 234.6 m^2/g, respectively.

The BJH adsorption cumulative pore volume values for each nanocomposite are reported in Table 2. Cumulative pore volumes for raw sepiolite and the cation-exchanged sepiolites were 0.45-0.46 m^3/g and following deposition, the pore volumes of the materials fell to 0.32-0.35 cm^3/g. The pore size distribution curves show narrow distributions of pore diameters between approximately 30-50 nm in width for all nanocomposites (Fig. 6). The adsorption-desorption isotherms show that all catalysts studied have type IV isotherms; however, following deposition the hysteresis loops changed from type H_1 to type H_4, reflective of the modified pore structure of nanocrystals on fibrous crystals (Fig. 7).

3.5   Photocatalytic Activity

Evidence of direct oxidation or photolysis was not detected in the dark or light controls under UV-A/B, respectfully, indicating that all OG degradation resulted from photocatalytic processes induced by UV-A/B (Fig. 8a). The results of Con-Sep$_{Ti}$, Mn-Sep$_{Ti}$, and Eu-Sep$_{Ti}$ degradation of OG under UV-A/B are shown in Fig. 8b-d as concentration as a function of time for 480 minutes. Con-Sep$_{Ti}$ and Eu-Sep$_{Ti}$ are both active for photocatalytic OG decomposition,

completing the reaction in approximately 480 min. Mn-Sep$_{Ti}$ displayed no photocatalytic activity whatsoever, indicating that addition of Mn completely inhibits the photocatalytic properties of TiO$_2$.

Table 3 shows the T$_{50}$ and T$_{90}$ values for each catalyst run. OG concentration over Con-Sep$_{Ti}$ was reduced to approximately 50% between t = 216 and 226 min and reduced to approximately 90% between t = 406 and 433 min. OG concentration over Mn-Sep$_{Ti}$ remained constant and thus there are no t$_{50}$ or t$_{90}$ values to report. OG concentration over Eu-Sep$_{Ti}$ was reduced to 50% between t =207 and 248 min and approximately 90% between t = 403 and 460 min.

Although the photocatalytic activity of TiO$_2$ is a function of several parameters (e.g. source wavelength, irradiation intensity, free oxygen, temperature, catalyst loading, pH, and initial concentration) these parameters were held constant in all experiments in order to draw comparison between the activities of the nanocomposite materials themselves. Thus, the degradation of OG over a sepiolite/TiO$_2$ catalyst can be modeled using Langmuir-Hinshelwood (L-H) kinetics in which degradation rates are proportional to the degree of surface coverage θ:

$$\theta = \frac{KC}{1+KC+K_SC_S} \qquad (1)$$

where K is the Langmuir adsorption constant of OG, K$_S$ is the adsorption constant of the solvent, C is the concentration of the OG, and C$_S$ is the concentration of the solvent. Because the solvent concentration is far larger than that of the OG and remains almost constant during the reaction, and that the catalyst coverage by water molecules remains almost constant, K$_S$C$_S$ can be ignored and Eq. 1 can be rewritten:

$$\theta = \frac{KC}{1+KC} \qquad (2)$$

when Eq. 2 is applied to the L-H kinetic rate expression (r=kθ), the following results:

$$r = -\frac{dC}{dt} = k\theta = \frac{kKC}{1+KC+\sum_{i=1}^{n} K_i C_i} \qquad (3)$$

where k is the reaction rate constant of the surface active site; K$_i$ is the adsorption coefficient of intermediate compounds on the catalyst surface; and C$_i$ is the concentration of those intermediates. Because the catalyst surface has a poor adsorption capacity for intermediate compounds (Zhou et al. 2018) and that intermediates are of limited concentration, the impact of

$\Sigma K_i C_i$ is negligible. Eq. 3 can now be simplified as an expression of the apparent degradation rate r:

$$r = \frac{kKC}{1+KC} \tag{4}$$

and because very low concentrations of OG were used in this experiment, the KC factor is negligible with respect to unity and therefore Eq. 4 can be rewritten to first-order kinetics with an apparent rate constant k_{app} which can be expressed as:

$$k_{app} = kK \tag{5}$$

which, when integrated, yields:

$$\ln\left(\frac{C_0}{C}\right) = k_{app}t \tag{6}$$

where t is the reaction time, C_0 is the initial solution concentration, and C is the solution concentration at t=0+n. The slope of the line on plot $\ln(C_0/C)$ vs. time is the value of k_{app}. Determining the apparent reaction rate constant (k_{app}) of each experimental run will provide a means of comparing the efficiencies of each catalyst and has been utilized previously for comparing performance between various materials independent of experimental parameters (Jing et al., 2013; Momeni and Ghayeb, 2016).

To determine the apparent reaction rate constant, plots of $\ln(C_0/C)$ vs. time for Con-Sep$_{Ti}$ and Eu-Sep$_{Ti}$ were created (Fig. 9). There are two distinct regions in the plots: at t = 0-240 minutes, the regressions are linear in character, representing 1st order reaction kinetics; beyond 240 minutes, higher order kinetics involving intermediates are acting. In order to determine k_{app} as an initial reaction rate, regression lines were drawn for t=0-240 min (Fig. 9 inset) and the value of the slope determine (reported in Table 3). The three runs of Con-Sep$_{Ti}$ yielded k_{app} values of 3.5×10^{-3} min^{-1}, 3.6×10^{-3} min^{-1}, and 3.6×10^{-3} min^{-1} with R^2 values of between 0.97 and 0.99. The three runs of Eu-Sep$_{Ti}$ yielded k_{app} values of 4.1×10^{-3} min^{-1}, 3.1×10^{-3} min^{-1}, and 3.5×10^{-3} min^{-1} with R^2 values of 0.99.

The results of the UV-C photolysis experiments are shown in Fig. 10 as plots of OG concentration as a function of time. Con-Sep$_{Ti}$ and Eu-Sep$_{Ti}$ exhibit the same trend as that in the irradiation without catalyst condition; however, both runs of Mn-Sep$_{Ti}$ show impeded progress of OG degradation over time – although the reaction was eventually completed at approximately

360 minutes (not shown). These data show that not only is Mn-Sep$_{Ti}$ inactive as a catalyst, as shown in the UV-A/B experiments, it impedes higher energetic irradiation UV-C from carrying out photolysis on the OG dye.

4.   Discussion

The addition of Mn and Eu to sepiolite as cation-exchange components prior to the deposition of TiO$_2$ had measurable effects on the physical, chemical, and catalytic properties of the sepiolite/TiO$_2$ nanocomposites in the degradation of OG. Only Con-Sep$_{Ti}$ and Eu-Sep$_{Ti}$ were active for total decomposition of OG; the difference between the two nanocomposites with respect to catalyst functionality was essentially negligible (k$_{app}$ values are approximately equal). In contrast, Mn-SepTi was completely inactive under UV-A/B irradiation. Potential explanations for this result revolve around deactivation of the titania, either by physical obfuscation (e.g. insulation of the semiconductor surface) or changes to the local charge environment (e.g. electron scavenging). Additional complexity comes in light of the UV-C experiments, which show that Mn-Sep$_{Ti}$ impeded primary photolysis, meaning it slowed down the rate of photon flux to the dye. Additional factors are considered below.

A difference between Cu and Zn was observed by Papoulis et al. (2019) in modified sepiolite/TiO$_2$ nanocomposites. They observed that Zn improved photocatalytic activity under UV-A irradiation due to the formation of a zinc-oxide co-catalyst but Cu inhibited catalytic activity, potentially due to enhanced recombination rate and minor activity shift ($\Delta E_g = 0.06$ eV) to the visible spectrum. The reason that Mn-Sep$_{Ti}$ and Eu-Sep$_{Ti}$ behaved differently in the photocatalytic reaction here is potentially related instead to how surface-held Mn and Eu behaved during growth of the titania phase. These relationships can be explored by examining the physical and chemical characterization data.

A major factor that can inhibit TiO$_2$ functionality is loss of surface area by sintering. Prevention of sintering can occur both by physical separation of the nanoparticles, but also can be influenced by altering the adjacent charge environment. A potential reason that Mn-Sep$_{Ti}$ and Eu-Sep$_{Ti}$ presented with both dispersed populations of titania nanoparticles and also areas with agglomeration is the presence of localized areas of lower pH, residual from exchange pre-treatment. Although cation-exchanged sepiolites were rinsed thoroughly, the complex pore structure makes the possibility of localized acidity difficult to rule out completely. It has been

demonstrated that pH can affect the dispersion state of nanoparticle populations by altering the zeta potential, resulting in agglomeration (Jiang et al, 2009). In spite of this textural difference, neither doped nanocomposite suffered any significant loss in specific surface area or pore volume (Table 2) in comparison to the control; indeed, Mn-Sep$_{Ti}$ actually shows the highest surface area and pore volume of the nanocomposites, with both Con-Sep$_{Ti}$ and Eu-Sep$_{Ti}$ having approximately the same surface area. Therefore, the observed agglomeration of titania on both Eu-Sep$_{Ti}$ and Mn-Sep$_{Ti}$ probably did not affect the photocatalytic activity. Although textural differences are not likely to blame for reduction in photocatalytic activity, exactly why Mn-Sep$_{Ti}$ has a higher surface area and pore volume when the TEM data show poorer dispersion is unclear.

The spatial chemical relationships shown in the STEM-EDS data (Fig. 5) have not yet been reported in studies of cation-exchanged TiO$_2$ nanocomposites; however, these data help to address questions regarding why catalytic activity changed. Mn does not appear to have any specific phase affinity (Fig. 5k) in Mn-Sep$_{Ti}$; it is present in association with both sepiolite and titania nanoparticles. In contrast, Eu appears to have a stronger association with titania nanoparticles than with sepiolite fibers in Eu-Sep$_{Ti}$ (Fig. 5l). From this result, it can be interpreted that Mn and Eu were superficially bonded to sepiolite and incorporated into the titania phase during nanoparticle growth, with Eu having a higher affinity than Mn. This relationship is important because if all Eu is doping into or onto TiO$_2$, Eu-Sep$_{Ti}$ will behave differently during catalysis than Mn-Sep$_{Ti}$ because the dopant is distributed differently.

It has been demonstrated in the literature that unsupported Mn-doped TiO$_2$ and Eu-doped TiO$_2$ have higher photocatalytic activity than TiO$_2$ (Zhang et al., 2009; Deng et al., 2011; Binas et al., 2012; Chauhan et al., 2012; Zhou et al., 2019). Lack of any detectable Eu$_2$O$_3$ phase and the results of the photocatalytic tests leads us to hypothesize that Eu^{3+} was incorporated into the TiO$_2$ lattice and the reaction was largely unaffected. Because we did not perform direct-incorporation, the benefit is potentially negligible likely due to low Eu concentration (Table 1). The photocatalytic activity results obtained by Zhou et al. (2019) in Eu-TiO$_2$ OG degradation are not directly comparable due to different synthesis methods.

If Mn-doped TiO$_2$ has superior photocatalytic activity to TiO$_2$, Mn-Sep$_{Ti}$ should have had higher reaction rates than Con-Sep$_{Ti}$; however this was not the case, so another process must have occurred. The color change observed in Mn-Sep$_{Ti}$ following the calcination process (Fig. 1)

most likely represents the oxidation of Mn. Despite repeated survey, neither TEM nor XRD revealed evidence of an additional Mn-oxyhydroxide phase; however, a lack of diffraction lines could also support high dispersion of a Mn-oxide or incorporation of Mn into the titania lattice (Villasenor et al., 2002); however, in such cases, crystalline Mn-oxide should have been active alone (Páez et al., 2011) and certainly in combination with TiO_2 as a direct dopant or as a co-catalyst (Xue et al., 2008). These lines of reasoning lead us to hypothesize that the formation of an amorphous Mn-oxyhydroxide coating on both TiO_2 and sepiolite was the fate of the Mn exchange cations and that this oxide coating inhibited photocatalytic activity by impeding hole migration to the catalyst surface and/or slowing the flux of photons to dye molecules through differences in absorbance. Furthermore, the formation of amorphous Mn-oxyhydroxide may also be related to the observed increase in surface area and total pore volume due to surficial irregularities.

Regarding the utility of cation-exchanging a phyllosilicate substrate in order to help facilitate activity of the primary photocatalyst, the data are unclear. Migration/secondary surface reactions of the cation-exchange components was also observed by Papoulis et al. (2019) in their photocatalytic degradation of NO_x gases, but not discussed in great detail. In the case of Zn, evidence of co-catalyst formation was found and activity improved, but the position of Cu relative to the nanocomposite was not detailed and activity decreased. Their synthesis method was similar to that used here, except that anatase growth was carried out in hydrothermal conditions at a lower temperature (180 °C), which may have yielded different results with respect to exchanged cation migration, but no spatially-resolved chemical data was reported, whereas the STEM-EDS results obtained here add new information to the phenomena potentially occurring.

This investigation demonstrates potential results that can occur when synthesizing a doped nanocomposite catalyst, particularly within the context of phyllosilicate cation exchange. It has been shown here that divalent and trivalent cations Mn and Eu may only be superficially bonded to the surface of sepiolite given how the elements came to be associated with Ti-rich areas following anatase growth. Further efforts to modify a phyllosilicate substrate for photocatalytic enhancement is suggested to be undertaken with pre-formed TiO_2 or perhaps in anhydrous conditions where migration may be mitigated.

71

5.   Conclusions

In this investigation, the modification of the substrate of a sepiolite/TiO_2 nanocomposite with Mn^{2+} and Eu^{3+} cations prior to deposition of TiO_2 (anatase) nanocrystals was undertaken to see the effects of support doping vs. catalyst doping in a UVR-driven photocatalytic azo dye degradation reaction. The XRD data show that cation exchange did not have a detectable effect on the crystal structure of sepiolite and that anatase growth was achieved with no rutile phase present. Cation exchange appears to have enhanced nanoparticle agglomeration, as observed in the TEM data, but specific surface area and pore volume were not affected – excepting an anomalous increase in surface area in Mn-Sep$_{Ti}$. The Mn^{2+} and Eu^{3+} cations did not remain surface-bound following the deposition and crystallization of anatase (TiO_2) as observed in STEM-EDS data. Mn migrated with no particular phase affinity and is hypothesized to have crystallized in-place into an amorphous oxyhydroxide coating during calcination, the results of which are visible at the macro-scale as a darkening of the material, which resulted in subsequent loss of catalytic activity in Orange G degradation under UV-A/B irradiation and hindrance of photolysis in Orange G degradation under UV-C irradiation. This reduction in activity is most likely not from loss of surface area, but impediment of hole migration to the catalyst surface by occlusive oxide formation and/or primary obstruction of photons. Eu migrated largely into the titania phase during calcination, into which it appears to incorporate in a manner that did not inhibit hole migration. This study and previous investigations on substrate-doping demonstrate complexity with respect to identity of the dopant as different transition and lanthanide metals have been shown to promote, inhibit, and have minimal effect on the progress of catalytic reactions involving volatile organic compound pollutants like azo dyes.

References

Basavarajappa, P. S., Patil, S. B., Ganganagappa, N., Reddy, K. R., Raghu, A. V., & Reddy, C. V. (2020). Recent progress in metal-doped TiO_2, non-metal doped/codoped TiO_2 and TiO_2 nanostructured hybrids for enhanced photocatalysis. International Journal of Hydrogen Energy, 45(13), 7764-7778.

Binas, V.D., Sambani, K., Maggos, T., Katsanaki, A., and Kiriakidis, G. (2012). Synthesis and photocatalytic activity of Mn-doped TiO_2 nanostructured powders under UV and visible light. Applied Catalysis B: Environmental, 113-114, 79-86.

Brown, M. A., & De Vito, S. C. (1993). Predicting azo dye toxicity. Critical reviews in environmental science and technology, 23(3), 249-324.

Chauhan, R., Kumar A., and Chaudhary, R.P. (2012). Structural and photocatalytic studies of Mn-doped TiO_2 nanoparticles. Spectrochimica Acta Part A: Molecular and Biomolecular Spectroscopy, 98, 256-264.

da Silva, C. G., & Faria, J. L. (2003). Photochemical and photocatalytic degradation of an azo dye in aqueous solution by UV irradiation. Journal of Photochemistry and Photobiology A: Chemistry, 155(1-3), 133-143.

Daghrir, R., Drogui, P., & Robert, D. (2013). Modified TiO_2 for environmental photocatalytic applications: a review. Industrial & Engineering Chemistry Research, 52(10), 3581-3599.

Deng, Q.R., Xia, X.H., Guo, M.L., Gao, Y., and Shao, B. (2011). Mn-doped TiO_2 nanopowders with remarkable visible light photocatalytic activity. Materials Letters, 65, 2051-2054.

Diamandescu, L., Vasiliu, F., Tarabasanu-Mihaila, D., Feder, M., Wlaicu, A.M., Teodorescu, C.M., Macovei, D., Enculescu, I., Parvulescu, V., and Vasile, E. (2008). Structural and photocatalytic properties of iron- and europium-doped TiO_2 nanoparticles obtained under hydrothermal conditions. Materials Chemistry and Physics, 112(1), 146-153.

Fernández, C., Larrechi, M. S., & Callao, M. P. (2010). An analytical overview of processes for removing organic dyes from wastewater effluents. TrAC Trends in Analytical Chemistry, 29(10), 1202-1211.

Gao, B., Chen, G.Z., and Puma, G.L. (2009). Carbon nanotubes/titanium dioxide (CNTs/TiO$_2$) nanocomposites prepared by conventional and novel surfactant wrapping sol-gel methods exhibiting enhanced photocatalytic activity. Applied Catalysis B: Environmental, 89(3-4), 503-509.

Ghosh, S., & Das, A. P. (2015). Modified titanium oxide (TiO$_2$) nanocomposites and its array of applications: a review. Toxicological & Environmental Chemistry, 97(5), 491-514.

Humayun, M., Raziq, F., Khan, A., & Luo, W. (2018). Modification strategies of TiO$_2$ for potential applications in photocatalysis: a critical review. Green Chemistry Letters and Reviews, 11(2), 86-102.

Jiang, J., Oberdörster, G., and Biswas, P. (2009) Characterization of size, surface charge, and agglomeration state of nanoparticle dispersions for toxicological studies. J. Nanopart. Res, 11, 77-89.

Jing, J., Feng, J., Li, W., Yu, W.W. (2013) Low-temperature synthesis of water-dispersible anatase titanium dioxide nanoparticles for photocatalysis. Journal of Colloid and Interface Science, 396, 90-94.

Khade, G.V., Gavade, N.L., Suwarnkar, M.B., Dhanavade, M.J., Sonawane, K.D., and Garadkar, K.M. (2017). Enhanced photocatalytic activity of europium doped TiO$_2$ under sunlight for the degradation of methyl orange. Journal of Materials Science: Materials in Electronics, 28, 11002-11011.

Kibanova, D., Cervini-Silva, J., and Destaillats, H. (2009). Efficiency of clay-TiO$_2$ nanocomposites on the photocatalytic elimination of a model hydrophobic air pollutant. Environ. Sci. Technol., 43(5), 1500-1506.

Konstantinou, I. K., & Albanis, T. A. (2004). TiO$_2$-assisted photocatalytic degradation of azo dyes in aqueous solution: kinetic and mechanistic investigations: a review. Applied Catalysis B: Environmental, 49(1), 1-14.

Kumar, S. G., & Devi, L. G. (2011). Review on modified TiO$_2$ photocatalysis under UV/visible light: selected results and related mechanisms on interfacial charge carrier transfer dynamics. The Journal of physical chemistry A, 115(46), 13211-13241.

Linsebigler, A.L., Lu, G., and Yates, J.T.Jr. (1995) Photocatalysis on TiO_2 surfaces: principles, mechanisms, and selected results. Chem. Rev., 95, 735-758.

Liu, B., Fang, Y., Li, Z., & Xu, S. (2015). Visible-light nanostructured photocatalysts—a review. Journal of nanoscience and nanotechnology, 15(2), 889-920.

Momeni, M.M., and Ghayeb, Y. (2016) Preparation of cobalt coated TiO_2 and WO_3-TiO_2 nanotube films via photo-assisted deposition with enhanced photocatalytic activity under visible light illumination. Ceramics International, 42(6), 7014-7022.

Páez, C. A., Liquet, D. Y., Calberg, C., Lambert, S. D., Willems, I., Germeau, A., Pirard, J-P., Heinrichs, B. (2011). Study of photocatalytic decomposition of hydrogen peroxide over ramsdellite-MnO_2 by O_2-pressure monitoring. Catalysis Communications, 15(1), 132-136.

Papoulis, D., Komarneni, A., Nikolopoulou, A., Tsolis-Katagas, P., Panagiotaras, D., Kacandes, H.G., Zhang, P., Yin, S., Sato, T., and Katsuki, H. (2010). Palygorskite- and halloysite-TiO_2 nanocomposites: synthesis and photocatalytic activity. Applied Clay Science, 50(1), 118-124.

Papoulis, D., Somalakidi, K., Todorova, N., Trapalis, C., Panagiotaras, D., Sygkridou, D., Stathatos, E., Gianni, E., Mavrikos, A., Komarneni, S. (2019). Sepiolite/TiO_2 and metal ion modified sepiolite/TiO_2 nanocomposites: synthesis, characterization and photocatalytic activity in abatement of NO_x gases. Applied Clay Science, 179, 105156.

Park, H., Park, Y., Kim, W., & Choi, W. (2013). Surface modification of TiO_2 photocatalyst for environmental applications. Journal of Photochemistry and Photobiology C: Photochemistry Reviews, 15, 1-20.

Rehman, S., Ullah, R., Butt, A., & Gohar, N. D. (2009). Strategies of making TiO_2 and ZnO visible light active. Journal of hazardous materials, 170(2-3), 560-569.

Reszczynska, J., Grzyb, T., Sobczak, J.W., Lisowski, W., Gazda, M., Ohtani, B., and Zaleska, A. (2014). Lanthanide co-doped TiO_2: The effect of metal type and amount on surface properties and photocatalytic activity. Applied Surface Science, 307, 333-345.

Shaul, G. M., Holdsworth, T. J., Dempsey, C. R., & Dostal, K. A. (1991). Fate of water soluble azo dyes in the activated sludge process. Chemosphere, 22(1-2), 107-119.

Stylidi, M., Kondarides, D. I., & Verykios, X. E. (2003). Pathways of solar light-induced photocatalytic degradation of azo dyes in aqueous TiO_2 suspensions. Applied Catalysis B: Environmental, 40(4), 271-286.

Tahir, M., and Amin, N.S. (2013). Photocatalytic reduction of carbon dioxide with water vapors over montmorillonite modified TiO_2 nanocomposites. Applied Catalysis B: Environmental, 142-143, 512-522.

Teh, C. M., & Mohamed, A. R. (2011). Roles of titanium dioxide and ion-doped titanium dioxide on photocatalytic degradation of organic pollutants (phenolic compounds and dyes) in aqueous solutions: A review. Journal of Alloys and Compounds, 509(5), 1648-1660.

Tünay, O., Kabdasli, I., Eremektar, G., & Orhon, D. (1996). Color removal from textile wastewaters. Water Science and Technology, 34(11), 9-16.

Uğurlu, M., & Karaoğlu, M. H. (2011). TiO_2 supported on sepiolite: preparation, structural and thermal characterization and catalytic behaviour in photocatalytic treatment of phenol and lignin from olive mill wastewater. Chemical Engineering Journal, 166(3), 859-867.

Villaseñor, J., Reyes, P., & Pecchi, G. (2002). Catalytic and photocatalytic ozonation of phenol on MnO_2 supported catalysts. Catalysis Today, 76(2-4), 121-131.

Wang, D., Wang, Y., Li, X., Luo, Q., An, J., and Yue, J. (2008). Sunlight photocatalytic activity of polypyrrole-TiO_2 nanocomposites prepared by 'in situ' method. Catalysis Communications, 9(6), 1162-1166.

Williams, G., Seger, B., and Kamat, P.V. (2008). TiO_2-graphene nanocomposites. UV-assisted photocatalytic reduction of graphene oxide. ACS Nano, 2(7), 1487-1491.

Xiaohong, W., Wei, Q., Xianbo, D., Yang, W., Huiling, L., and Zhaohua, J. (2007). Photocatalytic activity of Eu-doped TiO2 ceramic films prepared by microplasma oxidation method. Journal of Physics and Chemistry of Solids, 68(12), 2387-2393.

Xue, M., Huang, L., Wang, J. Q., Wang, Y., Gao, L., Zhu, J. H., & Zou, Z. G. (2008). The direct synthesis of mesoporous structured MnO_2/TiO_2 nanocomposite: a novel visible-light active photocatalyst with large pore size. Nanotechnology, 19(18), 185604.

Yen, C-Y, Lin, Y-F, Hung, C-H, Tseng, Y-H, Ma, C-C M., Chang, M-C, and Shao, H. (2008). The effects of synthesis procedures on the morphology and photocatalytic activity of multi-walled carbon nanotubes/TiO_2 nanocomposites. Nanotechnology, 19(4), 045604.

Zhang, L., He, D., & Jiang, P. (2009). MnO_2-doped anatase TiO_2–An excellent photocatalyst for degradation of organic contaminants in aqueous solution. Catalysis Communications, 10(10), 1414-1416.

Zhang, L., Liu, J., Tang, C., Lv., J, Zhong, H., Zhao, Y., and Wang, X. (2011). Palygorskite and SnO_2-TiO_2 for the photodegradation of phenol. Applied Clay Science, 51(1-2), 68-73.

Zhang, L., Liu, P., and Su, Z. (2006). Preparation of PANI-TiO_2 nanocomposites and their solid-phase photocatalytic degradation. Polymer Degradation and Stability, 91(9), 2213-2219.

Zhang, Y., Zhang, H., Xu, Y., and Wang, Y. (2003). Europium-doped nanocrystalline titanium dioxide: preparation, phase transformation, and photocatalytic properties. Journal of Materials Chemistry, 13, 2261-2265.

Zhou, F., Yan, C., Liang, T., Sun, Q., & Wang, H. (2018). Photocatalytic degradation of Orange G using sepiolite-TiO_2 nanocomposites: Optimization of physicochemical parameters and kinetics studies. Chemical Engineering Science, 183, 231-239.

Zhou, F., Yan, C., Sun, Q., and Komarneni, S. (2019). TiO_2/sepiolite nanocomposites doped with rare earth ions: preparation, characterization, and visible-light photocatalytic activity. Microporous and Mesoporous Materials, 274, 25-32.
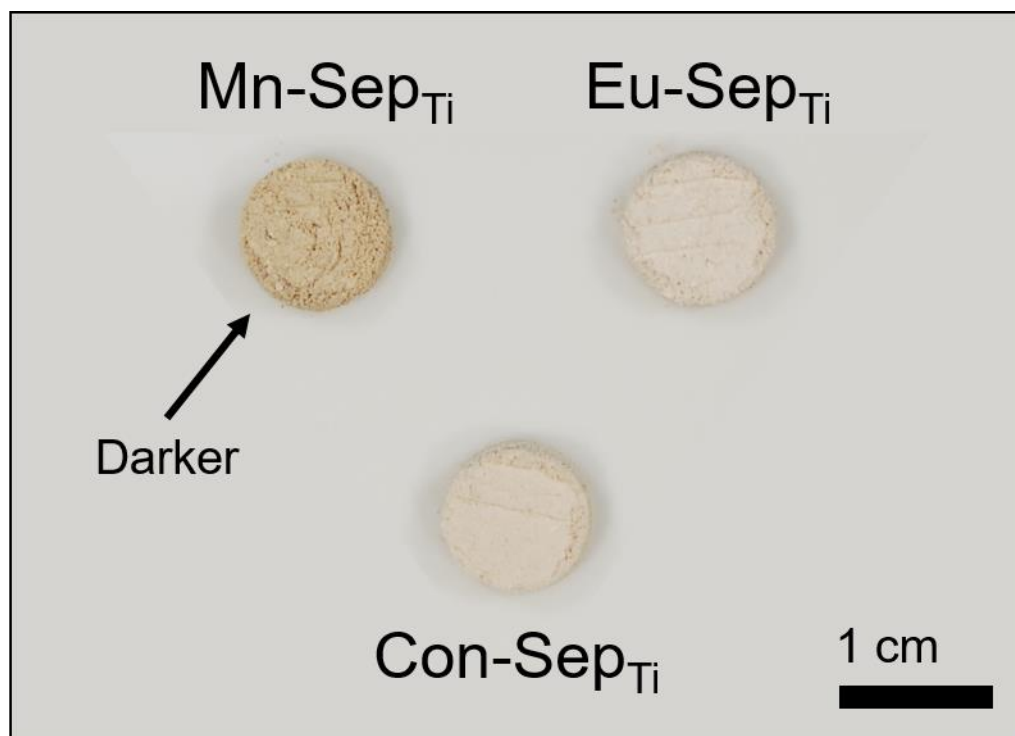
Figure 1. A photograph of the three catalyst materials synthesized in this study showing the difference in color that Mn-Sep$_{Ti}$ exhibits relative to Eu-Sep$_{Ti}$ and Con-Sep$_{Ti}$. The photograph was taken using color-corrected white light with no additional post-process enhancement.
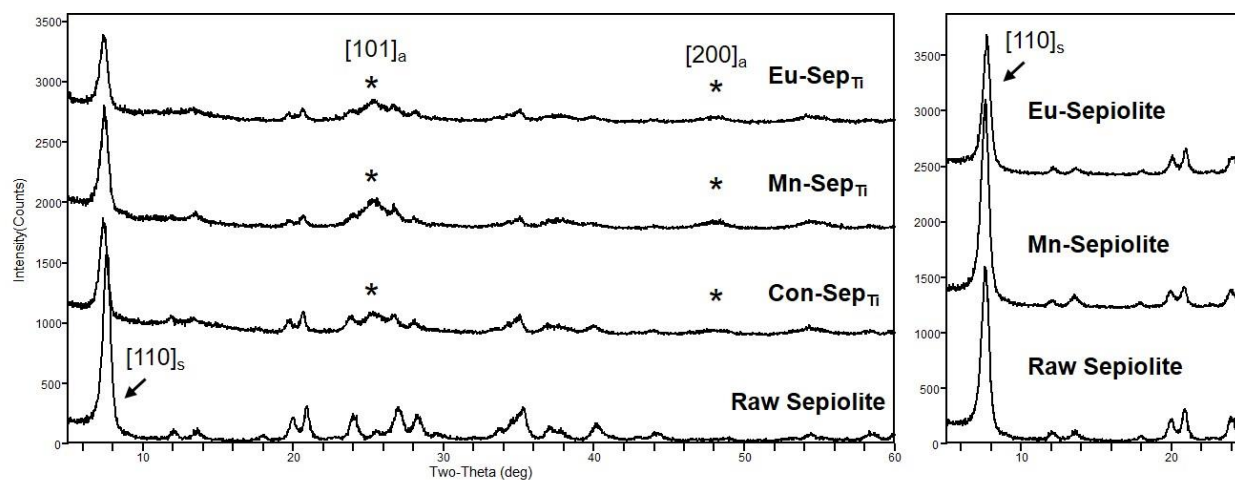
Figure 2. Powder X-ray diffraction patterns of all sepiolite/TiO$_2$ nanocomposites synthesized in this investigation compared to raw sepiolite - note the minor 2-theta shift of sepiolite (110) reflection and the appearance of anatase (101) and (200) reflections compared to raw sepiolite (left) and partial diffraction patterns of Eu- and Mn-exchanged sepiolite compared to raw sepiolite to demonstrate lack of 2-theta shift of (110) reflection (right). Anatase peaks are indicated with asterisks in addition to their *hkl* label.
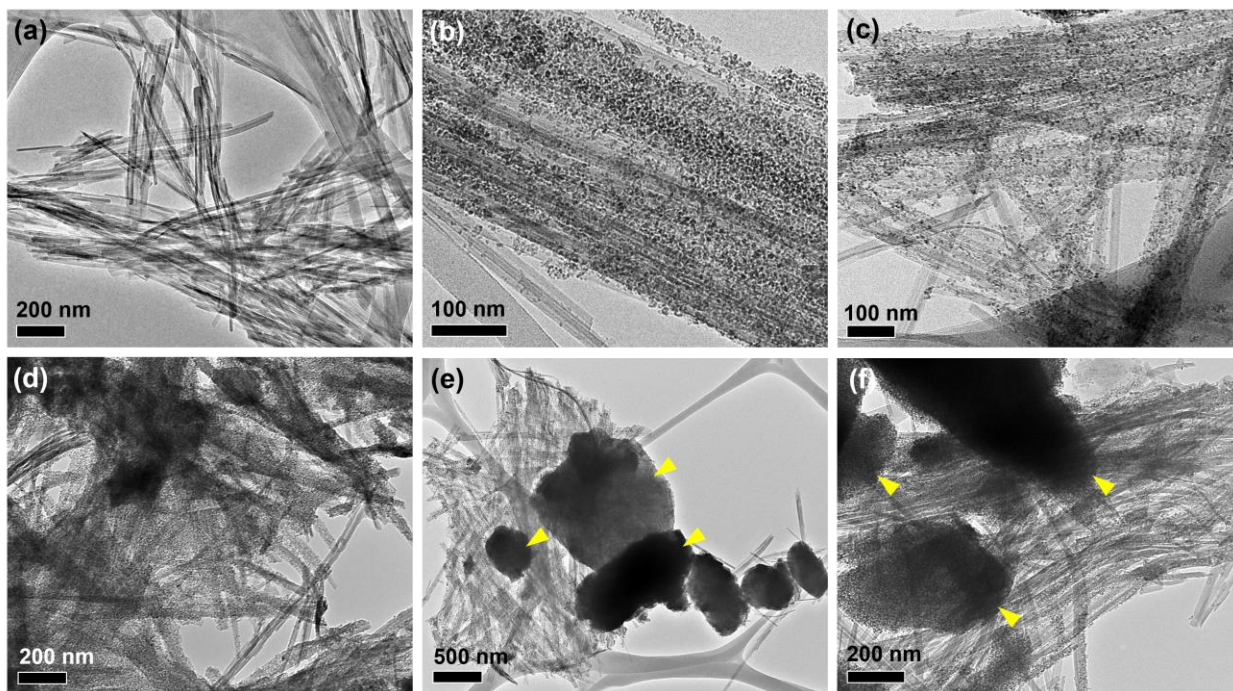
Figure 3. TEM brightfield images of the sepiolite/TiO$_2$ nanocomposites synthesized in this study. **(a)** image of raw sepiolite fibers; **(b-d)** images of Con-Sep$_{Ti}$, Mn-Sep$_{Ti}$, and Eu-Sep$_{Ti}$, respectively, showing good dispersion of titania nanoparticles on the sepiolite fibers; **(e-f)** images showing aggregation of titania nanoparticles on Mn-Sep$_{Ti}$ and Eu-Sep$_{Ti}$, respectively, adjacent to sepiolite fibers with dispersed nanoparticles.
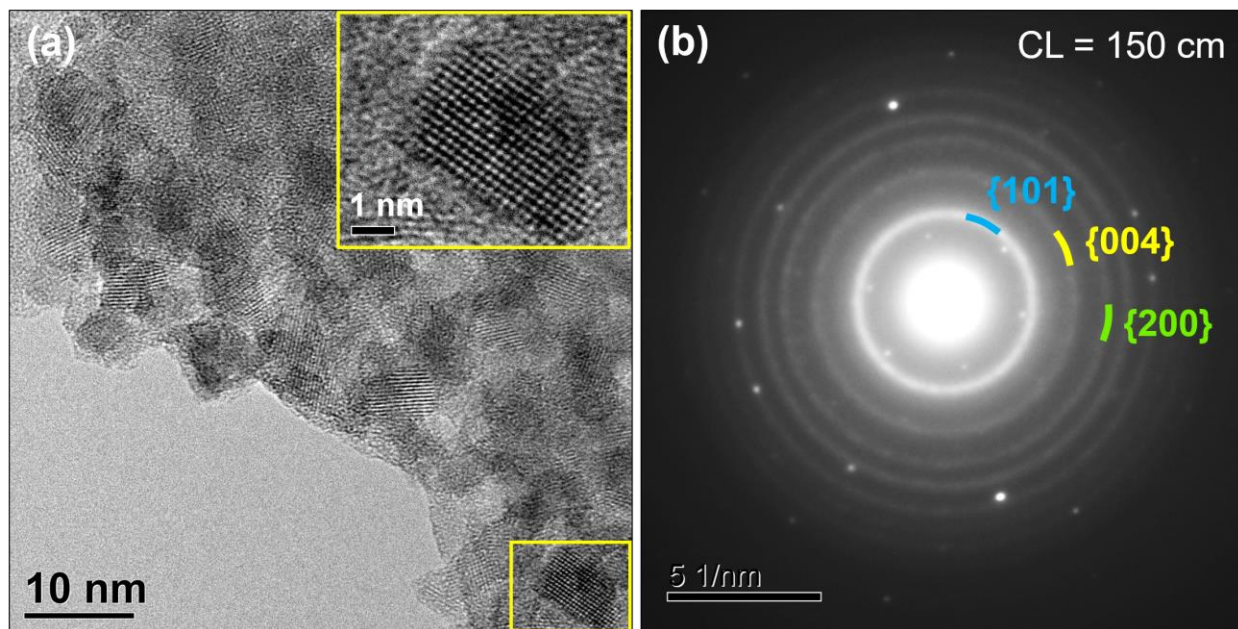
Figure 4. (a) TEM brightfield image showing atomic structural detail of the titania nanoparticles found on the samples produced in this study (inset) higher magnified image of a region indicated on the lower right showing discrete atoms; **(b)** selected area electron diffraction pattern of the region shown in (a) taken at 150 cm camera length showing a population of anatase nanoparticles with the (101), (004), and (200) spot rings labeled ($d_{(101)}$=3.5 Å, $d_{(004)}$=2.3 Å, and d=$_{(200)}$=1.8 Å).
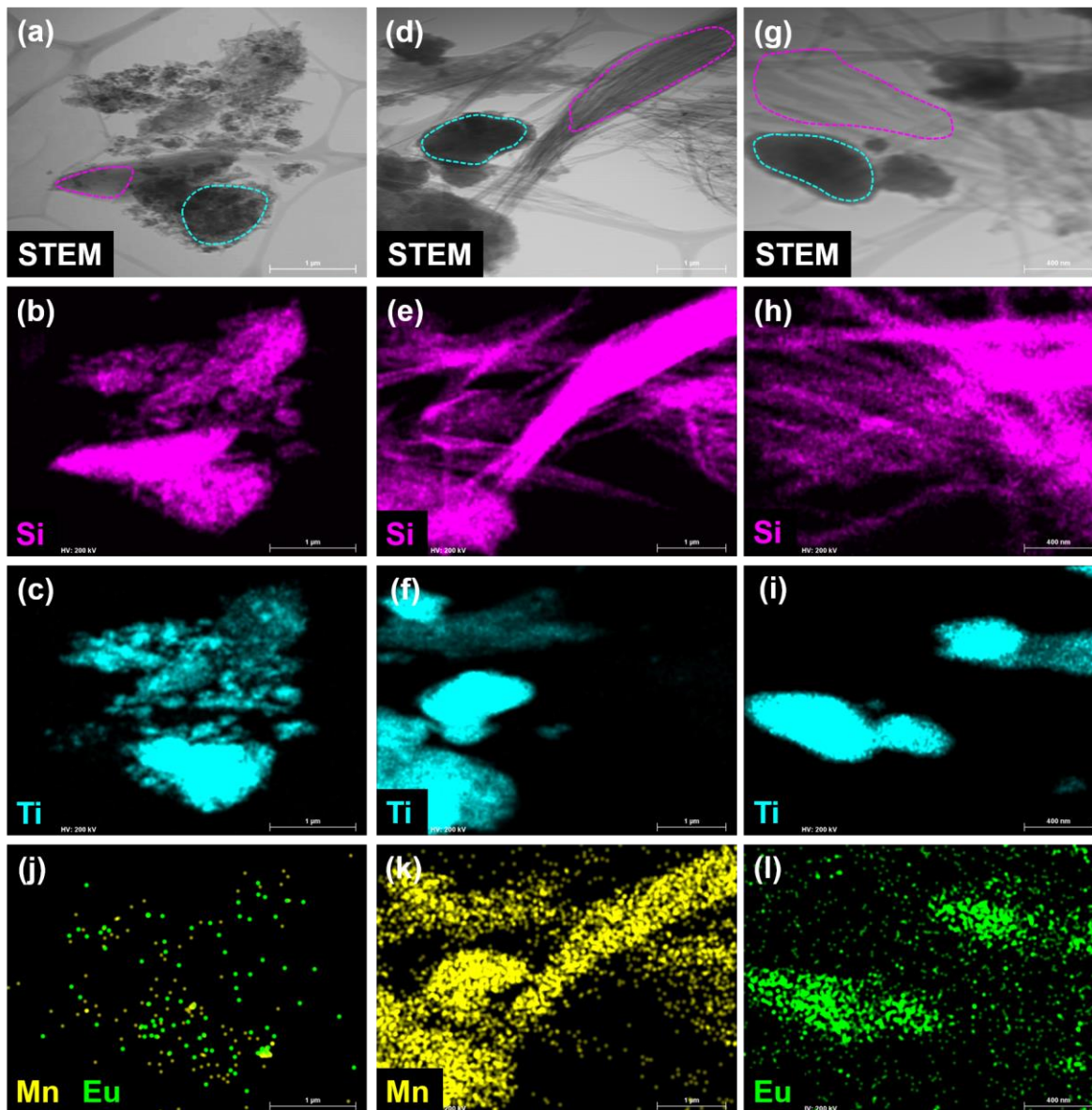
Figure 5. STEM-EDS elemental hypermaps of the nanocomposites synthesized in this study; pink and blue dashes on STEM-BF images represent hyperspectral regions of interest where quantifications of sepiolite and TiO_2 nanoparticles were measured (reported in Table 1) **(a)** STEM image of Con-Sep$_{Ti}$ bearing both sepiolite and titania **(b-c)** Si and Ti STEM-EDS maps of (a) demonstrating homogeneous distribution of Ti on Si-bearing phase sepiolite within Con-Sep$_{Ti}$; **(d)** STEM image of Mn-Sep$_{Ti}$ bearing both sepiolite and titania; **(e-f)** Si and Ti STEM-EDS maps of (d) demonstrating poor distribution of Ti on the sepiolite fibers; **(g)** STEM image of Eu-Sep$_{Ti}$ bearing both sepiolite and titania; **(h-i)** Si and Ti STEM-EDS maps of (g) demonstrating poor distribution of Ti on the sepiolite fibers; **(j)** Mn and Eu STEM map of (a) showing absence of Mn and Eu on Con-Sep$_{Ti}$ (colored spots are from internal scattering); **(k)** Mn STEM-EDS map of (d) showing homogeneous distribution of Mn on TiO_2 aggregates and sepiolite fibers; **(l)** Eu STEM-EDS map of (g) showing preference of Eu for the TiO_2 aggregates over the sepiolite fibers.
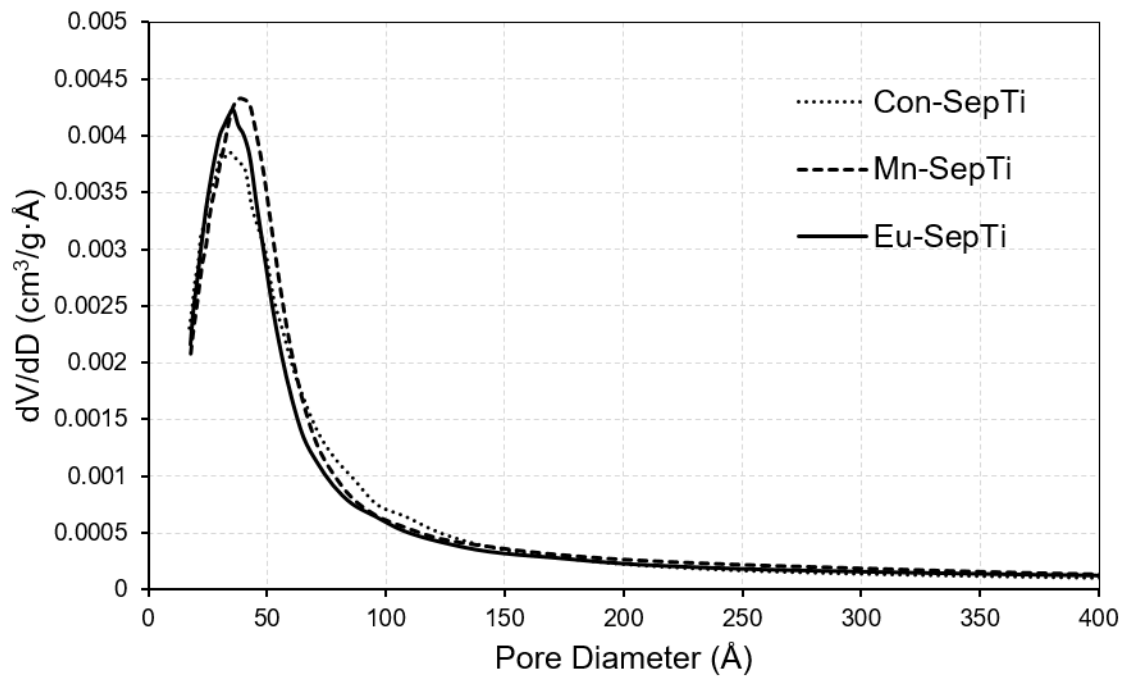
Figure 6. Pore size distribution curves for all pores between 17 and 3000 Å showing that pores in all nanocomposite materials are approximately 30-50 nm in diameter.
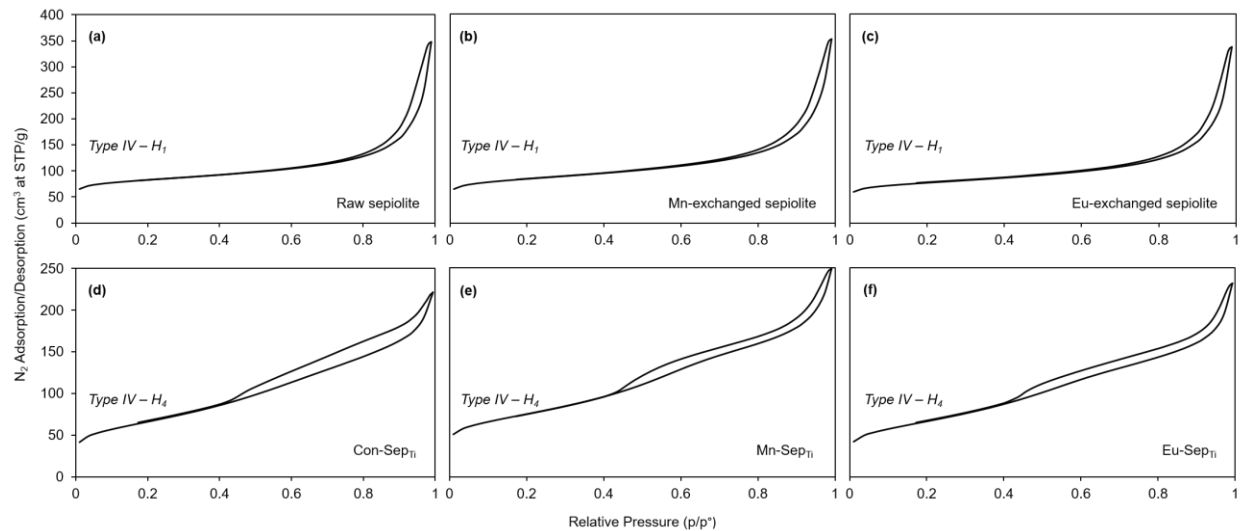
Figure 7. **(a)** Type IV adsorption/desorption isotherm of raw, untreated sepiolite showing H_1 hysteresis; **(b)** type IV adsorption/desorption isotherm of Mn-exchanged sepiolite, showing H_1 hysteresis; **(c)** type IV adsorption/desorption isotherm of Eu-exchanged sepiolite showing H_1 hysteresis; **(d)** type IV adsorption/desorption isotherm of Con-Sep$_{Ti}$ showing H_4 hysteresis; **(e)** type IV adsorption/desorption isotherm of Mn-Sep$_{Ti}$ showing H_4 hysteresis; **(f)** type IV adsorption/desorption isotherm of Eu-Sep$_{Ti}$ showing H_4 hysteresis.
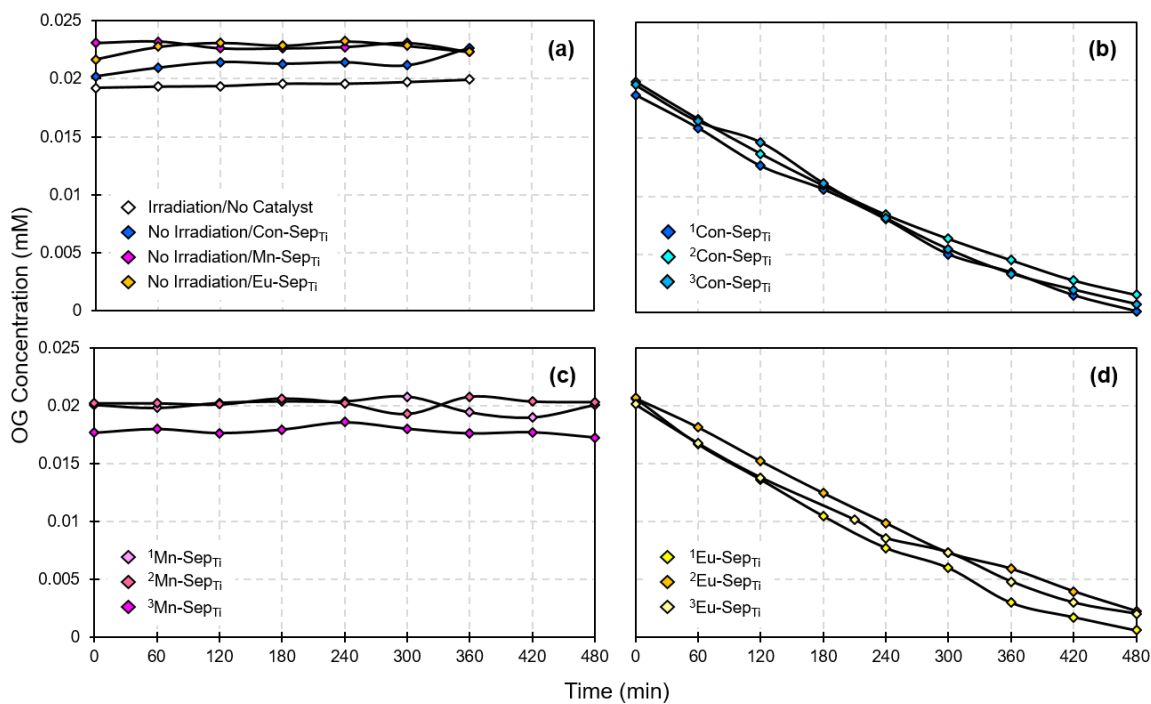
Figure 8. (a) Concentration vs. time plot for the control runs (360 min duration) of (i) with irradiation/no catalyst condition and (ii) no irradiation/with Con-Sep$_{Ti}$/Mn-Sep$_{Ti}$/Eu-Sep$_{Ti}$ conditions showing no evidence of photolysis or direct oxidation processes; **(b-d)** concentration vs. time plots for triplicate runs of Con-Sep$_{Ti}$, Mn-Sep$_{Ti}$, and Eu-Sep$_{Ti}$ for 480 min duration, respectfully (superscript indicates run number).
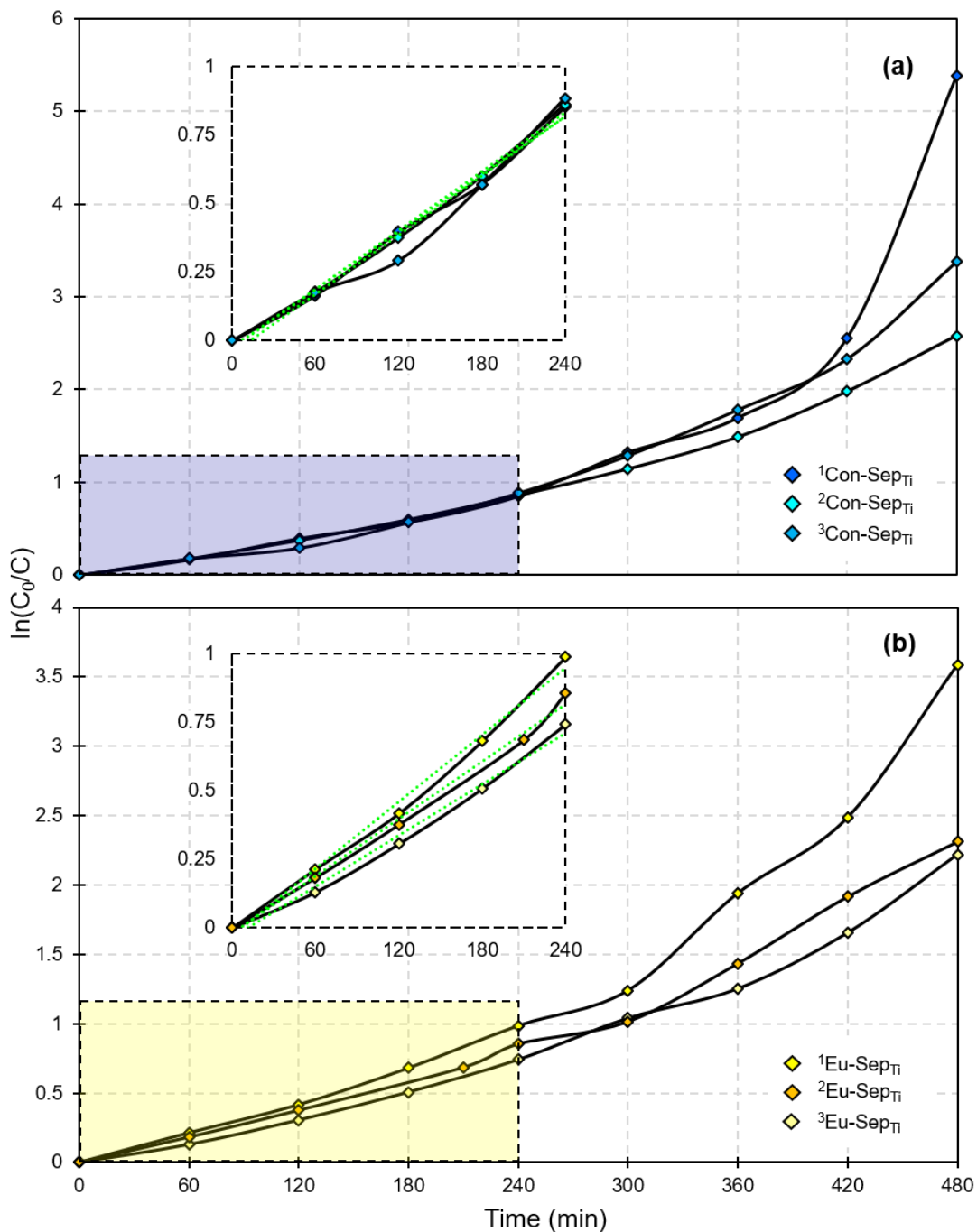
Figure 9. (a) ln(C_0/C) vs. time plots for each of the three runs of Con-Sep$_{Ti}$ (superscript indicates run number); inset is region defined in blue which represents 1st order kinetics (time = 0-240 min), the slope of each regression (green dashed lines) is equal to the initial apparent reaction rate constant (k_{app}). **(b)** ln(C_0/C) vs. time plots for each of the three runs of Eu-Sep$_{Ti}$ (superscript indicates run number); inset is region defined in yellow which represents 1st order kinetics (time = 0-240 min), the slope of each regression (green dashed lines) is equal to the initial apparent reaction rate constant (k_{app}).

86
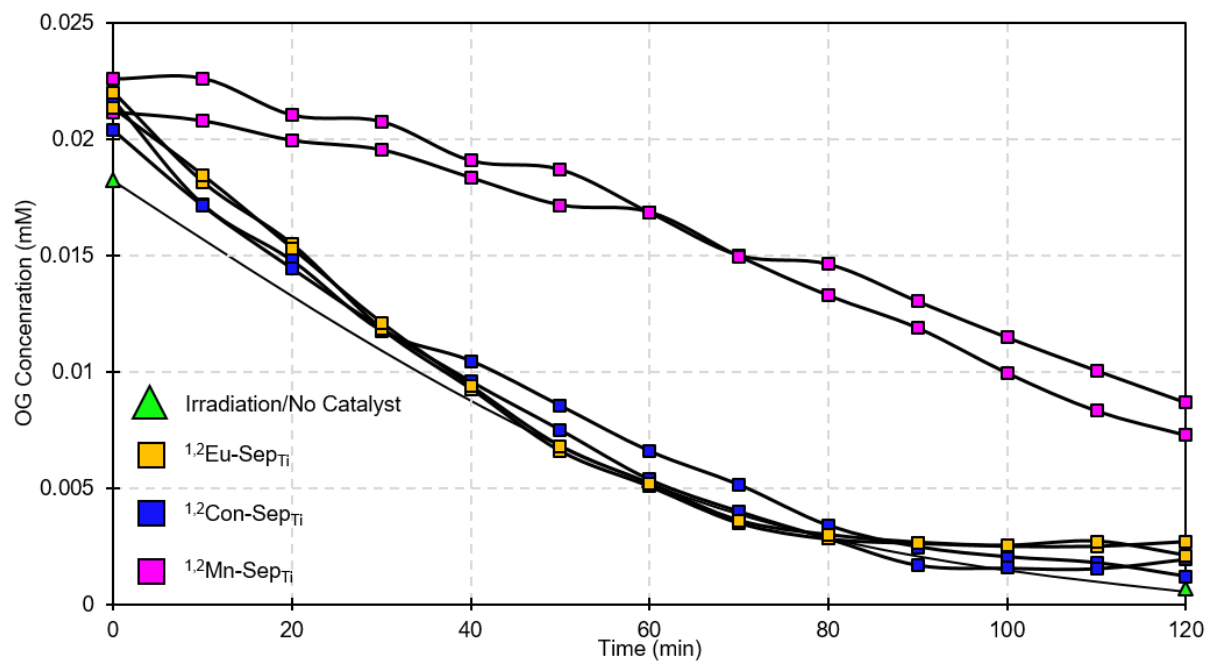
Figure 10. Concentration vs. time plot for OG photolysis via UV-C irradiation for 120 minute duration demonstrating the insulating capacity of Mn-Sep$_{Ti}$. Con-Sep$_{Ti}$ and Eu-Sep$_{Ti}$ permit essentially the same photolysis rate as that which occurs in the absence of a catalyst.

Table 2. Summary of elemental compositions of nanocomposite samples in this study. Values are representative of all pixels in the regions of interest indicated in the hyperspectral STEM-EDS maps in Figure 5. Spectral data for raw sepiolite was collected in TEM-brightfield mode.

Nanocomposite sample	Elemental Composition ([a]Normalized Mass %)								
	Si	O	Mg	Al	Cr	Fe	Ti	Mn	Eu
Raw Sepiolite	31.5	49.6	17.5	1.0	0.1	0.3	-nd-	-nd-	-nd-
[b]Con-SepTi	23.6	53.9	13.2	1.0	-nd-	0.3	8.1	-nd-	-nd-
[c]Con-SepTi	12.4	57.2	6.6	0.2	0.1	0.1	23.4	-nd-	-nd-
[b]Mn-SepTi	31.5	49.0	17.6	0.7	0.1	0.1	0.3	0.7	-nd-
[c]Mn-SepTi	3.3	59.0	1.4	0.2	-nd-	-nd-	35.8	0.3	-nd-
[b]Eu-SepTi	33.0	46.5	18.5	0.7	0.2	-nd-	1.2	-nd-	-nd-
[c]Eu-SepTi	3.1	68.0	1.8	0.2	-nd-	-nd-	26.7	-nd-	0.3

a. Based upon a P/B-ZAF-corrected standardless quantification model, series-fit deconvolution, and background-subtraction.
b. Sepiolite ROI (Fig. 5)
c. Nanoparticle ROI (Fig. 5)

Table 2. BET surface areas and BJH adsorption pore volumes of all of the nanocomposites synthesized in this study.

Nanocomposite Sample	BET Surface Area (m^2/g)	[a]Pore Volume (cm^3/g)
Raw sepiolite	275.1 ± 4.7	0.45 ± 0.01
Mn-sepiolite	279.1 ± 3.9	0.46 ± 0.01
Eu-sepiolite	256.9 ± 4.2	0.45 ± 0.01
Con-SepTi	236.5 ± 3.8	0.32 ± 0.01
Mn-SepTi	262.8 ± 1.0	0.35 ± 0.01
Eu-SepTi	234.6 ± 1.2	0.33 ± 0.01

a. BJH adsorption cumulative volume of pores between 17 Å and 3000 Å.

Table 3. The T_{50} and T_{90} values, which reflect the time (min) at which approximately 50% and 90% of the OG dye was degraded, for the nanocomposites synthesized in this study. The linear regression equations and R^2 values for the degradations were calculated from 0-240 minutes. Mn-Sep$_{Ti}$ failed to perform the reaction and thus there are no values to report.

Nanocomposite Sample	T_{50} (min)	T_{90} (min)	†Apparent reaction rate constant (k_{app}) (min^{-1})	Correlation coefficient R^2
[1]Con-Sep$_{Ti}$	216	406	3.5×10^{-3}	0.99
[2]Con-Sep$_{Ti}$	226	433	3.6×10^{-3}	0.99
[3]Con-Sep$_{Ti}$	221	412	3.6×10^{-3}	0.97
[1]Eu-Sep$_{Ti}$	207	403	4.1×10^{-3}	0.99
[2]Eu-Sep$_{Ti}$	248	460	3.1×10^{-3}	0.99
[3]Eu-Sep$_{Ti}$	231	444	3.5×10^{-3}	0.99

1. First Run
2. Second Run
3. Third Run
   †1st order (t = 0-240 min)

CHAPTER 4

INVESTIGATION OF THE CATALYTIC PROPERTIES OF CAVANSITE, A NATURALLY-OCCURRING MICROPOROUS VANADOSILICATE, AND CHARACTERIZATION USING ELECTRON MICROSCOPY

1. Introduction

Microporous vanadosilicates belong to a class of synthetic solids known as mixed octahedral-tetrahedral-pentahedral framework (OTP) silicates which feature both open framework topologies and isolated, redox sensitive vanadium centers in a variety of coordination environments (Rocha and Lin, 2005). This unique crystal chemistry and structure give vanadosilicates molecular sieve capabilities and potential catalytic activity. All reported production of novel microporous vanadosilicates with a variety of unique structural topologies took place during the 1990's and early 2000's by a handful of researchers inspired by expansive growth and advances in microporous titanosilicate synthesis (Rocha et al., 1997; Wang et al., 2001, 2002; Huang et al., 2002; Li et al. 2002; Brandão et al. 2002, 2003). Since the initial boom, efforts in synthetic vanadosilicate work have been reduced, although investigation of their unusual structural characteristics and dehydration properties (Danisi and Armbruster, 2018) as well as alternative synthesis routes continue (Ismail et al., 2009; Datta and Yoon, 2010, 2011). Although exploration of synthetic vanadosilicates has waned, perennial interest remains in the only known natural vanadosilicates, the mineral cavansite and its dimorph, pentagonite.

Cavansite ($Ca(VO)Si_4O_{10} \cdot 4H_2O$) was first discovered in Malheur County, Oregon (Staples et al., 1973) and has been of great interest since. The crystal structure of cavansite consists of two primary layers: a layer of SiO_4 tetrahedra (whose apices point alternatively along the b-axis) joined in a network of four- and eight-membered rings in (010) and a layer of alternating $V^{4+}O_5$ square-based pyramids and irregular $CaO_4(OH_2)_4$ polyhedra, which are arranged in ribbons along [100] in (010) (Evans, 1973, Hughes et al. 2011) (Fig. 1). The two layers are held together through shared bonds between VO_5 pyramid basal corners, silica tetrahedral apices, and calcium polyhedra. The four oxygen of the CaO_7 polyhedra that are not joined to the framework are bonded to H as water molecules. The apical oxygen of the VO_5 pyramid is not bonded to any other cation, only weakly to one hydrogen – this bond holds the calcium-vanadium ribbons together laterally. The structure of cavansite is closely related to that of the zeolite mineral gismondine, which is produced upon replacement of the VO_5 groups by two bridging oxygen.

Although technically a phyllosilicate, cavansite is often considered a framework mineral due to the remarkably zeolite-like character of its dehydration and three dimensional covalent

bonding. Shortly after discovery, cavansite was noted to have a stepwise dehydration pattern (Rinaldi, 1975; Demaiffe, 1994). This property has since been explored in great detail (Powar and Byrappa, 2001; Prasad and Prasad, 2006; Ishida et al., 2009; Danisi et al., 2012; Fisch et al., 2016; Martucci et al., 2016) alongside and in tandem with additional characterization techniques such as UV, visible, infrared, Raman, X-ray, and positron annihilation lifetime spectroscopies (Prasad and Prasad, 2006; Ravindran et al., 2012; Frost and Xi, 2012; Kumar et al., 2019), high-pressure studies (Ravindran et al., 2012; Danisi et al., 2015), and X-ray diffraction studies (Evans, 1973; Powar and Byrappa, 2001; Ishida et al., 2009; Hughes et al., 2011; Danisi et al., 2012, 2015; Martucci et al., 2015; Fisch et al., 2016; Kumar et al., 2019).

One of the first workers on cavansite, Rinaldi et al. (1975), proposed that cavansite may exhibit catalytic properties in the dehydrated state; this was also later mentioned by Hughes et al., (2011). Such behavior is certainly true of zeolites, whose catalytic properties are enhanced in the dehydrated state and at relatively high temperatures (Cruciani, 2006). However, despite great promise, no empirical investigation of the catalytic activity of synthetic or natural vanadosilicates has been carried out, a surprising fact considering wide success in selective oxidations over porous zeolites and zeotypes with V-doped frameworks (Reddy et al., 1993; Ramaswamy et al., 1994; Blasco et al., 1995; Kannan et al., 1997; Nieto, 2001; Pena et al., 2001; Gucbilmez et al. 2006, 2009). The present study aimed to address this knowledge gap. In addition to an ab initio investigation of cavansite's catalytic properties, we add to the existing body of literature with respect to morphological properties and potential natural variation by conducting a study of cavansite using scanning electron microscopy and transmission electron microscopy, which has not yet been reported.

In this investigation, we evaluated cavansite for catalytic activity for the first time. The model reaction we used is the gas phase oxidation of ethanol, for which V-doped zeolites are known to be active (Ramaswamy et al., 1994; Kannan et al., 1997; Gucbilmez et al. 2006, 2009). Relevant physical properties such as specific surface area in the hydrated and dehydrated states, thermal stability, crystal structure, and textural characteristics were also evaluated. In order to provide context for the measured catalytic activity in cavansite, another microporous framework mineral with a solely octahedral-based framework, cryptomelane, was tested and used as a reference material as it is known for high activity in ethanol oxidation (Santos et al., 2010, 2011; Almquist et al. 2014; Cymes et al., 2020). Our initial efforts to investigate cavansite as an

oxidative catalyst explored the temperature range 25-250 °C which represents a loss of 2 *apfu* H_2O; this experiment did not result in any clear catalytic activity trends (Cymes et al., 2017). In the present study, we take the reaction up to 350 °C with the hypothesis that loss of 3 *apfu* H_2O may yield different results.

2. Experimental

2.1 Sampling and preparation

Cavansite samples from Pune, India were purchased from John Betts Fine Minerals, New York, NY. Crystals of cavansite were carefully removed from the stilbite-rich substrate and sonicated to remove dust and other environmental impurities before being crushed in a mortar a pestle into a fine powder. This powder was used for all analyses and catalytic runs with no further modification.

Cryptomelane used for comparison was synthesized by a dry-milling method adapted from Ding et al. (2005) in which manganese(II) acetate and potassium permanaganate in a 3:2 ratio were ground together in a mortar and pestle thoroughly for 30 minutes until a uniform gray-lavender color was achieved. Next, the mixture was heated for 4 hr at 80 °C in air before being washed several times to remove residual organic compounds and finally dried overnight at 80 °C in air and calcined in air at 450 °C for 2 hr.

2.2 Powder X-ray diffraction (XRD)

Powder X-ray diffraction patterns were collected using a Scintag Pad X diffractometer equipped with a Peltier detector. Samples were mounted into pack slides. The powders were analyzed in the range of 0 to 90° 2-theta in a 0.02 step size with a 2.0 s dwell time. The radiation source was monochromated Cu Kα (1.5418 Å) and the instrument was operated at 40 kV and 35 mA.

2.3 Scanning electron microscopy and energy dispersive spectroscopy (SEM/EDS)

To explore the morphology and texture of cavansite, samples were examined using a Zeiss Supra 35 VP field emission scanning electron microscopy (SEM) equipped with a Bruker Quantax 100 energy dispersive X-ray microanalytical system. For imaging, 2.0 keV accelerating voltage was used and for EDS analysis, 20 keV was used. Sample preparation involved

dispersing prepared cavansite powder onto a carbon tab affixed to an aluminum pin stub and samples were not coated.

2.4 High resolution transmission electron microscopy (HR-TEM)

To explore the nature of cavansite at the atomic level, samples were analyzed using a JEOL JEM 2100 TEM/STEM operated in brightfield at 200 keV accelerating voltage. The electron beam was produced by a LaB_6 source and images were captured using a Gatan Orius SC200D camera. Samples for TEM analysis were loaded as particulate mounts onto 3.0 mm lacey-carbon copper grids.

2.5 Surface area and pore geometry analysis

The BET surface area and pore geometry were determined for cavansite using nitrogen porosimetry at 77 K using a Micrometrics Tri-Star II BET surface area analyzer. Prior to loading, cavansite was degassed for 30 minutes 50 °C with a helium purge to remove surface humidity. Cavansite was analyzed in its natural state and also following a heat treatment of 1 hr at 350 °C to determine if loss of zeolitic water impacted surface area or pore geometry.

2.6 Thermogravimetric and derivative thermogravimetric analysis (TGA/DTG)

TGA measurements were conducted using a TA Instruments Q500 analyzer to evaluate weight loss in cavansite as a function of temperature. The temperature was raised from room temperature (approximately 25 °C) to 800 °C at a rate of 10 °C/min. Nitrogen gas was used to purge the furnace at 60 mL/min and cavansite was analyzed in a platinum pan holder. The first derivative of the TGA curve – which is percentage weight loss as a function of temperature – is also reported (DTG) in order to determine the temperature maxima of each weight loss step.

2.7 Gas-phase catalytic oxidation of ethanol

The model heterogeneous experiment used in this study to evaluate if cavansite possesses catalytic activity is the gas phase oxidation of ethanol in the range of 25 °C – 350 °C. The oxidation of ethanol generates acetaldehyde and carbon dioxide as primary reaction products, as shown in Eqs. 1 and 2. Other potential reaction products are ethylene, carbon monoxide, and acetic acid; these were not analyzed for using the methods described here however, if present, they may contribute to any mass balance errors.

$$CH_3CH_2OH_{(g)} + \frac{1}{2}O_2{}_{(g)} \rightarrow C_2H_4O_{(g)} + H_2O_{(g)} \tag{1}$$

$$C_2H_4O_{(g)} + \frac{5}{2}O_2{}_{(g)} \rightarrow 2CO_2{}_{(g)} + 2H_2O_{(g)} \tag{2}$$
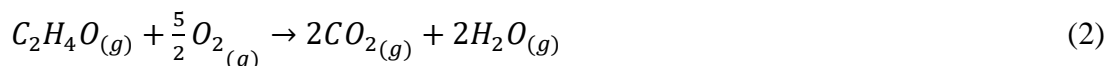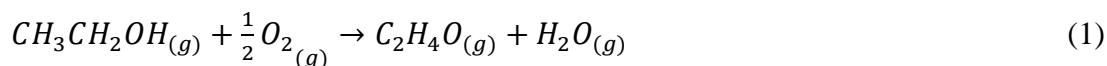
A schematic of the reactor system is shown in Fig. 2 and the experimental protocol is similar to that described in Cymes et al. (2020). In brief, house air was directed to a mass flow controller which modulated the flow to 100 ccpm – this flow entered a diffusion cell which generated and directed ethanol vapor (approximately 420 ppm ethanol) into a fixed-bed plug flow reactor which was housed in a Lindberg Blue M tube furnace. The stainless steel tube reactor was 55 cm long, with a 0.635 cm OD and a 0.124 WT; the catalyst plug volume was 0.47 cm^3 (gas hourly space velocity = 12,750 h^{-1}). Approximately 50 mg of catalyst powder was loaded into the reactor and held by a bed of quartz wool.

Following interaction with the catalyst bed, the reactor effluent was directed to a 1000 cm^3 positive-pressurized chamber equipped with an Amprobe® CO_2-100 non-dispersive infrared CO_2 detector (1 ppm resolution, ± 30 ppm accuracy) which was calibrated between 0 and 2000 ppm. Effluent collections for CO_2 concentration determinations were taken for 1 hour at each temperature interval. Following CO_2 concentration determination, the effluent was redirected to a Pyrex® glass impinger where samples were collected in double distilled deionized water for a ten minutes, which scrubbed the effluent so that ethanol and acetaldehyde could be measured. Finally the samples were injected into an Agilent 6890 N gas chromatograph with flame ionization detection (GC/FID) which was calibrated before each run using prepared ethanol standards. In addition to cavansite samples, a control reaction was carried out on a reactor loaded with quartz wool alone to assess contributions from the stainless steel tube; this is referred to in later figures as 'Qtz Wool'

3. Results

3.1 X-ray diffraction

The results of XRD analysis are shown in Fig 3. Our cavansite sample matched well to PDF #: 01-077-0930 which describes cavansite as a member of the space group *Pcmn* with unit cell dimensions *a* = 9.767 Å, *b* = 13.630 Å, and *c* = 9.627 Å; cavansite is orthorhombic. These data are consistent with previous powder diffraction studies of cavansite (Demaiffe, 1994; Prasad

and Prasad, 2007; Ishida et al. 2009; Danisi et al. 2015; Martucci et al., 2016) No secondary phases were detected in the cavansite powders.

3.2   *SEM and EDS*

SEM analysis of cavansite reveals crystals to be euhedral in form with prominent and excellent cleavage planes in {010} and also {100} in addition to perpendicular sinuous, conchoidal fracture lines along. Staples et al. (1973) reported only one set of cleavage planes in (010) and so the set we observed in (100) represents a previously unrecognized set; the latter set are likely a function of the reduced bonding perpendicular to the tunnels. Fig. 4a shows a view of cleavage developing in two directions – indicated with green and pink dashed lines – and so this is likely viewing parallel to the c-axis. Fig. 4b is viewing perpendicular to one of the cleavage directions, indicated with pink solid lines, and parallel to another, indicated with green dashed lines; conchoidal fracture patterns expressed at the surface are indicated in this image with a yellow circle. Fig. 4c is not normal to any axis and so all three planes are visible with cleavage and fracture present and indicated as above. Finally, Fig 4d likely represents a growth face, interpreted by the presence of surficial etching features that cross cut the cleavage planes at approximately 45° – (indicated with blue arrows). These etching features may be related to water diffusion paths as large pore spaces exist in that plane as can be seen in Fig. 1c. EDS analysis of multiple cavansite crystals reveal very pure composition; only Ca, V, Si, and O were detected (C and Al are from the sample holder); a representative energy dispersive spectrum for cavansite is shown in Fig. 5.

3.3   *Brightfield HR-TEM*

The TEM analysis of cavansite proved to be a challenging exercise due in part to the interaction of the sample with the electron beam, which caused rapid (i.e. < 5 seconds) dehydration and also difficulty finding a useful viewing direction. Void spaces in the 4- and 8-membered rings in the a-c plane are blocked by underlying Ca and V cations; therefore these pores were not able to be imaged, and while there was some success in obtaining lattice-fringe images of the b-c plane, the layer structure collapsed rapidly – as happens with most hydrous phyllosilicates – and the images obtained were of substandard quality and so are not included.

The highest quality images taken were parallel to the c-axis and these are represented in Fig. 6. In Fig 6a, the general texture of a cavansite particle 625 nm across can be seen with a

bladed, prismatic morphology consistent with that observed in SEM. Fig. 6b is a higher magnification image of the region indicated in yellow on the crystal showing detail of the atomic structure – this image is blown up in Fig. 6c and the selected area electron diffraction (SAED) pattern of the region is shown in Fig. 6d. The interatomic distances are 3.0 Å and measurement of selected diffraction spots are consistent with cavansite as viewed nearly parallel to the b-axis at lower *apfu* H_2O, which is assumed to be the state cavansite is under electron beam irradiation (Danisi et al. 2012).

Evaluation of many crystals on approximately 6-8 prepared TEM grids had to be undertaken in order to find an area in the right orientation; although the sample holder had two-directional tilting capabilities, the rapid de-watering limited the amount of time able to make adjustments. We found that lowering the condenser lens voltage at 200 keV and using longer camera exposure times allowed us to capture quality images of cavansite.

3.4 N_2 Porosimetry

The results of nitrogen porosimetry experiments on cavansite are shown in Table 1. The BET surface area of cavansite analyzed at 25 °C was 0.9 m^2/g and the cumulative pore volume was 0.003 cm^3/g. Upon heat treatment at 350 °C for 1 hour, the BET surface area of cavansite increased to 1.1 m^2/g and the cumulative pore volume increased to 0.004 cm^3/g. These gains in surface area and porosity are likely due to removal of superficially-held hydrous species and/or the generation of surface fissures due to the reduction in unit cell volume, a phenomenon described by Danisi et al. (2012). This phenomenon is supported by the changes in the distribution of pore sizes, shown graphically in Fig. 7. Upon heat treatment, the percentage of volume in macropores decreased from 64.8 to 63.5% and the percentage of volume contained in mesopores increased from 33.8 to 35.3% and microporosity remained largely unaffected. The adsorption and desorption isotherms are shown in Fig. 8; the isotherm is a reversible type III, indicating absence of capillary condensation and unrestricted multilayer formation processes.

3.5   TGA and DTG

The results of TGA and DTG analysis are shown in Fig. 9. The major weight loss steps of cavansite, as determined at peak maxima of the DTG graph, were measured at 60, 150, 240, and 410 °C, which correlate to those reported by Phadke and Apte (1994), Powar and Byrappa (2001), Prasad and Prasad (2007), Ishida et al., (2009), and Danisi et al., (2012). In experiments

by Danisi et al. (2012), it was determined that the first weight loss step is from expulsion of the H_2O molecule at the O9 site, the second step from the expulsion of H_2O at the O7 site, and the third loss from the expulsion of H_2O at the O8 site. Loss of these water molecules reduced the coordination number of Ca to fivefold and also causes reduction in unit cell volume. After 400 °C, cavansite decomposes to an amorphous phase following the loss of the last water molecule. The weight gain shown in our data at approximately 650 °C onwards represents the oxidation of V^{4+} to V^{5+} also indicated by loss of the characteristic blue color of VO^{2+} in the sample upon unloading the platinum pan.

Table 2 shows the mass loss percentages of cavansite at specific temperature intervals. Between 25 and 100 °C, cavansite lost 2.9 % of initial mass, representing loss of surface adsorbed species and 1 *apfu* H_2O; between 100 and 200 °C, cavansite lost 4.7 % of initial mass, this likely represented a loss of 2 *apfu* H_2O total; between 200-300 °C, cavansite lost 3.3 % of initial mass representing loss of a total of 3 *apfu* H_2O; between 300 and 400 °C, cavansite lost another 1.5 % of initial mass likely representing residual third weight loss stage H_2O; and at temperatures greater than 400 °C, cavansite lost another 3.1 % of its initial mass, representing the fourth and final water molecule. In total, cavansite lost 15.5 % of its initial mass between 25 °C and 800 °C.

3.6   Oxidative catalytic experiments

The results of effluent concentration monitoring throughout each run are shown in Fig. 10 as a function of temperature for each species detected in this study (ethanol, acetaldehyde, and carbon dioxide). Figure 10a shows the results from the quartz wool run; here, ethanol concentration remained constant until approximately 250 °C at which it was found to decrease and the first acetaldehyde signals were detected. At 300 °C, ethanol concentration was approximately half of the initial concentration as acetaldehyde concentration increased. By 350 °C, ethanol was reduced nearly completely as acetaldehyde concentration reached peak concentration as calculated from stoichiometric balancing and only here was CO_2 found to increase above ambient levels. With respect to CO_2 as a final reaction product, the control run did not drive the reaction forward fully, but intermediate acetaldehyde was produced.

Fig. 10b shows the results from the cavansite run. Decline in ethanol concentration occurred at a lower temperature than in the control run as measured at 200 °C; however,

acetaldehyde was not detected until 250 °C. At 300 °C, ethanol concentration was lower still as acetaldehyde concentration increases. Similar to the control run, an increase in CO_2 concentration was not detected until 350 °C; however here acetaldehyde concentration was lower than that measured for the control although ethanol concentration at 350 °C was close to zero. The decline in ethanol concentration was not entirely matched by production of acetaldehyde and CO_2, as shown by acetaldehyde selectivity determinations shown in Fig. 11a; this indicates that other intermediate products may have formed.

Finally, Fig. 10c shows the result of the cryptomelane comparative run. Cryptomelane is active for ethanol oxidation in a lower temperature range than cavansite and so this run demonstrates what a completed reaction looks like. Ethanol oxidation by cryptomelane began between 25 °C and 100 °C as shown by the generation of acetaldehyde and CO_2 at 100 °C. Ethanol was completely absent from the reactor effluent by 175 °C, acetaldehyde production peaked at approximately 125 °C before falling to zero by 200 °C, and CO_2 concentration was double that of initial ethanol concentration by 200 °C indicating completion of the reaction with a correct mass balance.

With respect to selectivity, as mentioned previously, the selectivity of acetaldehyde over cavansite is significantly lower than that over the quartz wool reaction (Fig. 11a), indicating that all moles of ethanol reacted were not forming acetaldehyde, but rather another intermediate compound. This is in contrast to the very high selectivity of acetaldehyde and carbon dioxide over cryptomelane at low and high temperatures, respectively (Fig. 11b). The mechanism that is ruling the behavior of cavansite in ethanol oxidation is considered and discussed further later.

The light off curves for each catalyst are shown in Fig. 12 – the DTG pattern for cavansite is also shown again on this figure in order to discuss their potential relationship later on. Cryptomelane, as discussed in the flow diagrams, converted 100% of ethanol by 175 °C. In contrast, cavansite reached approximately 75% ethanol conversion by 350 °C and the control quartz wool reached 85% conversion by 350 °C. Obviously, cavansite is an inferior catalyst when compared to cryptomelane for ethanol oxidation with respect to temperature efficiency; however, it did appear to possess some activity beyond that of the control. Cavansite appeared to begin converting ethanol at 200 °C and this correlates to the 2 *apfu* H_2O state. The difference in activity between 200 °C and 300 °C between cavansite and the control – the temperature interval

during which cavansite is reduced to 1 *apfu* H_2O is noteworthy and will be discussed further later.

With respect to ethanol concentration, the oxidation reaction is assumed to be first order (Almquist et al., 2014; Ismagilov et al., 2008) and therefore activation energy E_a (kJ/mole) was determined here by first determining the reaction rate constant k (s^{-1}) at each temperature interval using Eq. 3 which, when linearized, yields Eq. 4 where C_A is equal to the concentration of ethanol in the reactor effluent at a given temperature interval, C_{A0} is the initial concentration of ethanol in the reactor effluent at room temperature, and τ is equal to residence time derived by dividing the plug volume (V) by the volumetric flow rate (Q).

$$C_A = C_{A_0} \times e^{-k\tau} \tag{3}$$

$$ln\left(\frac{C_A}{C_{A_0}}\right) = -k\tau \tag{4}$$

Finally, activation energy was calculated using the Arrhenius equation (Eq. 5) which is linearized in Eq. 6 where A is equal to the pre-exponential factor (s^{-1}), R is equal to the gas constant (0.008314 kJ/mol·K) and T is equal to absolute temperature (K). The natural log of k as determined for each temperature interval was then plotted against the inverse of temperature (in Kelvin) for the range 250 to 350 °C, as shown in Fig. 13. This range was selected because although cavansite was converting ethanol by 200 °C, the quartz wool was not and so a higher temperature range was used so that the slopes would be more comparable. The slope of the linear trend line plotted between each point is equal to (-E/R), which was then used to calculate activation energy, which is shown in Table 3. The activation energy of cavansite was determined to be 42.3 kJ/mole and the activation energy of the control quartz wool was 88.4 kJ/mol.

$$k = Ae^{-\frac{E}{RT}} \tag{5}$$

$$\ln(k) = \ln(A) - \frac{E}{R}\left(\frac{1}{T}\right) \tag{6}$$

Reaction rates were calculated for cavansite per gram using Eq. 7 and per square meter using Eq. 8 where X_a is equal to the fraction of ethanol converted at 250 °C and Q_a is equal to double the initial ethanol flow rate for stoichiometric balance. These values are reported in Table 3 along with the T_{50} and T_{80} values, which are the temperatures at which each material was converting 50% and 80% of ethanol, respectively. The reaction rates of cavansite were 18.1

μmoles/min·g catalyst and 20.1 μmoles/min·m^2 catalyst. The T$_{50}$ and T$_{80}$ of cavansite were 573.15 and 623.15 K, respectively and the T$_{50}$ and T$_{80}$ of the control quartz wool were 583.15 and 613.15 K, respectively.

$$\frac{X_{a_{250°C}} \times Q_{a_0}}{mass\ of\ catalyst\ (g)} = \frac{\mu moles}{min \times (g)catalyst} \tag{7}$$

$$\frac{X_{a_{250°C}} \times Q_{a_0}}{mass\ of\ catalyst\ (g) \times surface\ area\ (\frac{m^2}{g})} = \frac{umoles}{min \times m^2 catalyst} \tag{8}$$

4.   Discussion

4.1   *Physical property characterization*

With respect to the crystal structure and thermal stability analyses, our data did not shed new light that had not already been thoroughly related by other workers (Powar and Byrappa, 2001; Prasad and Prasad, 2006; Ishida et al., 2009; Danisi et al., 2012; Fisch et al., 2016; Martucci et al., 2016). Of note, however, are the new electron microscopy data and the nitrogen porosimetry results.

Staples et al. (1973) identified only one set of cleavage planes on (010) in cavansite; however, from our SEM results (Fig. 4), there are clearly two perpendicular directions that readily develop. We hypothesize that these occur perpendicular to the tunnel axis on the (010) and (100) planes as the bonding density is reduced in these directions. The conchoidal fracture observed was widespread, striking in appearance, and appears to be present perpendicular to the two cleavage directions, along the c-axis. In addition, linear etching on growth surfaces has not previously been reported in cavansite and so this texture represents a novel observation.

The TEM micrographs taken of cavansite show the atomic structure in clear detail; we were able to capture images of the channels running perpendicular to the c-axis (Fig. 6) and the dimensionality of these channels is consistent with published data on the crystal structure of cavansite. Cavansite occurs as bladed and prismatic crystal aggregates using the particulate sample preparation method for TEM – this method appears to work well despite the time required to find a useful viewing direction and not render the phase amorphous.

The nitrogen porosimetry experiments showed that heat treatment does yield a minor increase in specific surface area and that this is likely a function of generation of mesoporosity related to unit cell shrinkage. In comparison to the surface area of other microporous materials,

cavansite is unimpressive. The surface area of the cryptomelane used for comparison in the catalysis experiments, for example, is greater than 100 times that of cavansite. It is unlikely that increases in surface area as a function of heating temperature contributed substantially to the catalytic activity, as detailed later.

4.2   *Catalytic activity*

The removal of ethanol over cavansite was first detected at approximately 50 °C lower than over the control; indeed, the activation energy of cavansite was double that of the control (Table 3). Between 200 and 300 °C, cavansite had higher conversion percentages than the control (Fig. 12). These data demonstrate that cavansite possesses some measure of catalytic activity for total ethanol oxidation; however, a Mars and Van Krevelen mechanism does not fully describe the activity observed as it does for ethanol oxidation over cryptomelane, particularly as it relates to acetaldehyde selectivity (Fig. 11a). There is a significant difference between cavansite and the control in acetaldehyde selectivity – it is clear that although ethanol was degraded by cavansite, the majority of it did not transform into acetaldehyde. This is in contrast to cryptomelane, which has high selectivity to acetaldehyde at low temperatures and high selectivity to CO_2 at higher temperatures with clear product summation at 150 °C (Fig. 11b).

The poor selectivity to acetaldehyde by cavansite is highly similar to the behavior of V-doped zeolites as ethanol oxidation catalysts. Gucbilmez et al. (2006, 2009) found that when V was introduced into the framework of MCM-41 (Mobil Composition of Matter No. 41), ethylene is favored over acetaldehyde due to the catalyst adsorbing excess gaseous oxygen which reacted with adsorbed ethoxides to form ethylene, rather than the catalyst performing a redox mechanism using the catalyst's lattice oxygen. Ramaswamy et al. (1994) found V-incorporated ZSM-11 (Zeolite Socony Mobil No. 11) had higher selectivity to acetic acid and ethyl acetate than acetaldehyde. Kannan et al. (1997) performed a study in which they carried out ethanol oxidation over ZSM-11 in which V was doped into the framework (VS2-E) and one in which V was doped into extra-framework positions (VS2-A-Cal) and found that VS2-E had high selectivity for diethyl ether and VS2-A-Cal had high selectivity for acetaldehyde. They attribute the formation of diethyl ether to contributions of both the V=O and V-O-Si bonds (two active sites) present in the framework-incorporated vanadium and the formation of acetaldehyde to V=O bonds (single

active site) present in the extra-framework-incorporated vanadium; the latter being more geared toward redox activity.

With respect to the relationship between the dehydration stage of cavansite and its catalytic behavior, the data are inconclusive (Fig. 12). Cavansite began to convert ethanol at a temperature between 150 and 200 °C, which coincides with the removal of the second water molecule and conversion increased significantly between 200 and 300 °C, which coincides with the removal of the third water molecule; however, a simple relationship is unlikely. A potential mechanism that may be occurring that echoes that observed by Gucbilmez et al. (2006, 2009) is that cavansite may become oxophilic at elevated temperatures and scavenge oxygen to maintain 6-fold coordination in the calcium site or in another scenario newly liberated H_2O may react with surface adsorbed ethanol to form intermediate compounds. At this stage, only hypotheticals exist – because this is the first foray into vanadosilicate catalytic evaluation, continual efforts will be required in order to fully understand what seems to be a complex interaction mechanism.

5.   Conclusions

In this investigation, the mineral cavansite is investigated for the first time as a catalytic material and the model reaction used was the gas phase oxidation of ethanol. It was suspected by past cavansite researchers that in the dehydrated state, cavansite may possess catalytic properties associated with exposure of the apical oxygen of $V^{4+}O_5$ square pyramidal sites and potential redox capabilities. Our results show that cavansite is active for partial oxidation; approximately 80% of ethanol was removed from the effluent at 350 °C with acetaldehyde and carbon dioxide reaction products detected. However, owing to low acetaldehyde selectivity, it is suspected that partial oxidation into compounds such as ethylene, diethyl ether, acetic acid, and ethyl acetate is the more favored reaction pathway over cavansite. This is potentially due to interactions between the cavansite surface V=O and V-O-Si bonds and gaseous oxygen species, a phenomenon recognized in framework-doped vanadium zeolites. In addition to catalytic activity, scanning and transmission electron microscopic images of cavansite reveal the existence of a previously unrecognized set of cleavage planes in (100) which reflect reduced bond density in planes oriented parallel to the direction of tunnel propagation along the c-axis.

References

Almquist, C., Krekeler, M., & Jiang, L. (2014). An investigation on the structure and catalytic activity of cryptomelane-type manganese oxide materials prepared by different synthesis routes. Chemical Engineering Journal, 252, 249-262.

Blasco, T., Concepcion, P., Nieto, J.L., Perezpariente, J. (1995). Preparation, characterization, and catalytic properties of VAPO-5 for the oxydehydrogenation of propane. Journal of Catalysis, 152(1), 1-17.

Brandão, P., Philippou, A., Hanif, N., Ribeiro-Claro, P., Ferreira, A., Anderson, M. W., Rocha, J. (2002). Synthesis and characterization of two novel large-pore crystalline vanadosilicates. Chemistry of Materials, 14(3), 1053–1057. https://doi.org/10.1021/cm010613q

Brandão, P., Valente, A., Philippou, A., Ferreira, A., Anderson, M. W., Rocha, J. (2003). Hydrothermal synthesis and characterisation of two novel large-pore framework vanadium silicates. European Journal of Inorganic Chemistry, (6), 1175–1180. https://doi.org/10.1002/ejic.200390151

Cruciani, G. (2006) Zeolites upon heating: factors governing their thermal stability and structural changes. Journal of Physics and Chemistry of Solids, 67(9-10), 1973-1994.

Cymes, B. A., Krekeler, M. P., & Almquist, C. B. (2017). The catalytic activity of natural cavansite $(Ca(VO)Si_4O_{10} \cdot 4H_2O)$ (267-10). Geological Society of America Abstracts with Programs, 49(6), http://doi.org/10.1130/abs/2017AM-303309

Cymes, B.A., Almquist, C.B., Krekeler, M.P. (2020). Europium-doped cryptomelane: Multi-pathway synthesis, characterization, and evaluation for the gas phase catalytic oxidation of ethanol. Applied Catalysis A: General, 589, 117310.

Danisi, R.M., Armbruster, T. (2018). Dehydration of microporous vanadosilicates: the case of VSH-13Na. Acta Crystallographica Section B: Structural Science, Crystal Engineering and Materials, 74(6), 483–491. https://doi.org/10.1107/S2052520618011423

Danisi, R.M., Armbruster, T., Arletti, R., Gatta, G.D., Vezzalini, G., Quartieri, S., Dmitriev, V. (2015). Elastic behavior and pressure-induced structural modifications of the microporous

Ca(VO)Si$_4$O$_{10}$·4H$_2$O dimorphs cavansite and pentagonite. Microporous and Mesoporous Materials, 204(C), 257–268. https://doi.org/10.1016/j.micromeso.2014.11.029

Danisi, R.M., Armbruster, T., Lazic, B. (2012). In situ dehydration behavior of zeolite like cavansite: a single crystal X-ray study. American Mineralogist, 98(7), 1874–1880. https://doi.org/10.2138/am.2013.4465

Datta, S.J., Yoon, K.B. (2010). Synthesis of pure VSH-2 in large quantities and its characterization. Topics in Catalysis, 53(19–20), 1311–1318. https://doi.org/10.1007/s11244-010-9589-2

Datta, S.J.,Yoon, K.B. (2011). Large scale synthesis of pure VSH-1 and its characterization. Microporous and Mesoporous Materials, 143(1), 115–124. https://doi.org/10.1016/j.micromeso.2011.02.019

Demaiffe, D. (1994). Thermal behaviour of cavansite from Wagholi, India. Mineralogical Magazine, 58, 501–505.

Ding, Y.S., Shen, X.F., Sithambaram, S., Gomez, S., Kumar, R., Crisostomo, V.M.B., Suib, S.L., Aindow, M. (2005). Synthesis and catalytic activity of cryptomelane-type manganese dioxide nanomaterials produced by a novel solvent-free method. Chemistry of Materials, 17(21), 5382–5389. https://doi.org/10.1021/cm051294w

Evans, H.T. Jr. (1973). The crystal structures of cavansite and pentagonite. American Mineralogist, 58, 412–424. https://doi.org/10.1063/1.3204074

Fisch, M., Cametti, G., Armbruster, T., Casati, N. (2016). MS36-P2 Dynamic temperature-rate dependent in-situ dehydration of cavansite (Ca(VO)(Si$_4$O$_{10}$)·4H$_2$O). Foundations of Crystallography, 72, s391.

Frost, R.L., & Xi, Y. (2012). Vibrational spectroscopic study of the minerals cavansite and pentagonite Ca(V^{4+}O)Si$_4$O$_{10}$·4H$_2$O. Spectrochimica Acta Part A: Molecular and Biomolecular Spectroscopy, 95, 263–269. https://doi.org/10.1016/j.saa.2012.04.021

Gucbilmez, Y., Dogu, T., Balci, S. (2006) Ethylene and acetaldehyde production by selective oxidation of ethanol using mesoporous V-MCM-41 catalysts. Ind. Eng. Chem. Res. 45(10), 3496-3502.

Gucbilmez, Y., Dogu, T., Balci, S. (2009) Activity comparison of MCM-41 and V-MCM-41 catalysts for ethanol selective oxidation and DRIFTS analysis. International Journal of Chemical Reactor Engineering, 7(1), 1542-6580.

Huang, J., Wang, X., Liu, L., Jacobson, A.J. (2002). Synthesis and characterization of an open framework vanadium silicate (VSH-16Na). Solid State Sciences, 4(9), 1193-1198.

Hughes, J.M.; Derr, R.S., Cureton, F., Campana, C.F., Druschel, G. (2011). The crystal structure of cavansite: Location of the H_2O molecules and hydrogen atoms in $Ca(VO)Si_4O_{10}\cdot 4H_2O$. The Canadian Mineralogist, 49, 1267-1272. https://doi.org/10.3749/canmin.49.5.1267

Ishida, N., Kimata, M., Nishida, N., Hatta, T., Shimizu, M., Akasaka, T. (2009). Polymorphic relation between cavansite and pentagonite: Genetic implications of oxonium ion in cavansite. Journal of Mineralogical and Petrological Sciences, 104, 241–252. https://doi.org/10.2465/jmps.070724b

Ismagilov, I.Z., Michurin, E.M., Sukhova, O.B., Tsykoza, L.T., Matus, E.V., Kerzhentsev, M. A., Ismagilov, Z.R., Zagoruiko, A.N., Rebrov, E.V., de Croon, M.H.J.M., Schouten, J. C. (2008). Oxidation of organic compounds in a microstructured catalytic reactor. Chemical Engineering Journal, 135, S57-S65.

Ismail, M.N., Fraiman, N.D., Callahan Jr, D.M., Gursoy, G., Viveiros, E., Ozkanat, O., Ji, Z., Willey, R.J., Warzywoda, J., Sacco Jr, A. (2009). First unseeded hydrothermal synthesis of microporous vanadosilicate AM-6. Microporous and mesoporous materials, 120(3), 454-459.

Kannan, S., Sen, T., Sivasanker, S. (1997). Catalytic transformation of ethanol over microporous vanadium silicate molecular sieves with MEL structure (VS-2). Journal of Catalysis, 170(2), 304–310. https://doi.org/10.1006/jcat.1997.1755

Kumar, B.S., Ravikumar, H.B., Preakash, A.G., Girish, H.N., Ishigaki, T., Madhusuda, P. (2019) Room temperature X-ray and positron annihilation lifetime spectroscopic studies of cavansite crystals. Japanese Journal of Applied Physics, 58(11), 110904.

Li, C.-Y., Hsieh, C.-Y., Lin, H.-M., Kao, H.-M., Lii, K.-H. (2002). High-temperature, high-pressure hydrothermal synthesis, crystal structure, and solid state NMR spectroscopy of a new vanadium(IV) silicate: $Rb_2(VO)(Si_4O_{10})\cdot xH_2O$. Inorganic Chemistry, 41(16), 4206–4210. https://doi.org/10.1021/ic020187q

Martucci, A., Rodeghero, E., Cruciani, G. (2016). Continuous dehydration of cavansite under dynamic conditions: an in situ synchrotron powder-diffraction study. European Journal of Mineralogy, 28(1), 5–13. https://doi.org/10.1127/ejm/2015/0027-2512

Nieto, J. (2001). Microporous and mesoporous materials with isolated vanadium species as selective catalysts in the gas phase oxidation reactions. Topics in Catalysis, 15(2), 189–194. http://doi.og/10.1023/A:1016605916860

Pena, M.L., Dejoz, A., Fornes, V., Rey, F., Vazquez, M.I., Nieto, J.L. (2001). V-containing MCM-41 and MCM-48 catalysts for the selective oxidation of propane in gas phase. Applied Catalysis A: General, 209(1-2), 155-164.

Phadke, A.V., Apte, A. (1994). Thermal behaviour of cavansite from Wagholi, India. Mineralogical Magazine, 58(392), 501-505.

Powar, K.B., Byrappa, K. (2001). X-ray, thermal, and infrared studied of cavansite from Wagholi western Maharashtra, India. Journal of Mineralogical and Petrological Scicnes, 96, 1-6.

Prasad, P.S.R., Prasad, K.S. (2007). Dehydration behavior of natural cavansite: An in-situ FTIR and Raman spectroscopic study. Materials Chemistry and Physics, 105(2–3), 395–400. https://doi.org/10.1016/j.matchemphys.2007.05.005

Ramaswamy, A.V., Sivasanker, S., Ratnasamy, P. (1994). Selective oxidation reactions over metallosilicate molecular sieves: A comparison of titanium and vanadium silicates with MEL structure. Microporous Materials, 2(5), 451–458. https://doi.org/10.1016/0927-6513(94)00018-2

Ravindran, T.R., Arora, A.K., Parthasarathy, G. (2012). Raman spectroscopic study of pressure induced amorphization in Cavansite. J. Phys.: Conf. Ser, 377. https://doi.org/10.1088/1742-6596/377/1/012004

Reddy, K.R., Ramaswamy, A.V., Ratnasamy, P. (1993). Studies on crystalline microporous vanadium silicates IV: Synthesis characterization and catalytic properties of V-NCL-1, a large-pore molecular sieve. Journal of Catalysis, 143, 275-285.

Rinaldi, R., Pluth, J.J., & Smith, J.V. (1975). Crystal structure of cavansite dehydrated at 220°C. Acta Cryst. B, 31(6), 1598–1602. https://doi.org/10.1107/S0567740875005766

Rocha, J., Brandão, P., Lin, Z., Anderson, M.W., Alfredsson, V., Terasaki, O. (1997). The first large-pore vanadosilicate framework containing hexacoordinated vanadium. Angewandte Chemie International Edition in English, 36(1-2),100–102.

Rocha, J., Lin, Z. (2005). Microporous mixed octahedral-pentahedral-tetrahedral framework silicates. Reviews in Mineralogy and Geochemistry, 57, 173–201. https://doi.org/10.2138/rmg.2005.57.6

Santos, V.P., Pereira, M.F.R., Órfão, J.J.M., Figueiredo, J.L. (2010). The role of lattice oxygen on the activity of manganese oxides towards the oxidation of volatile organic compounds. Applied Catalysis B: Environmental, 99(1-2), 353-363.

Santos, V.P., Pereira, M.F.R., Órfão, J.J.M., Figueiredo, J.L. (2011). Mixture effects during the oxidation of toluene, ethyl acetate and ethanol over a cryptomelane catalyst. Journal of Hazardous materials, 185(2-3), 1236-1240.

Staples, L.W., Evans, H.T. Jr., Lindsay, J.R. (1973). Cavansite and pentagonite, new dimorphous calcium vanadium silicate minerals from Oregon. American Mineralogist, 58, 405–411.

Wang, X., Liu, L., & Jacobson, A.J. (2002). Open-framework and microporous vanadium silicates. Journal of the American Chemical Society, 124(26), 7812–7820. https://doi.org/10.1021/ja020354l

Wang, X., Liu, L., Jacobson, A.J. (2001). The novel open-framework vanadium silicates $K_2(VO)(Si_4O_{10})\cdot H_2O$ (VSH-1) and $Cs_2(VO)(Si_6O_{14})\cdot 3H_2O$ (VSH-2). Angewandte Chemie International Edition, 40(11), 2174–2176.
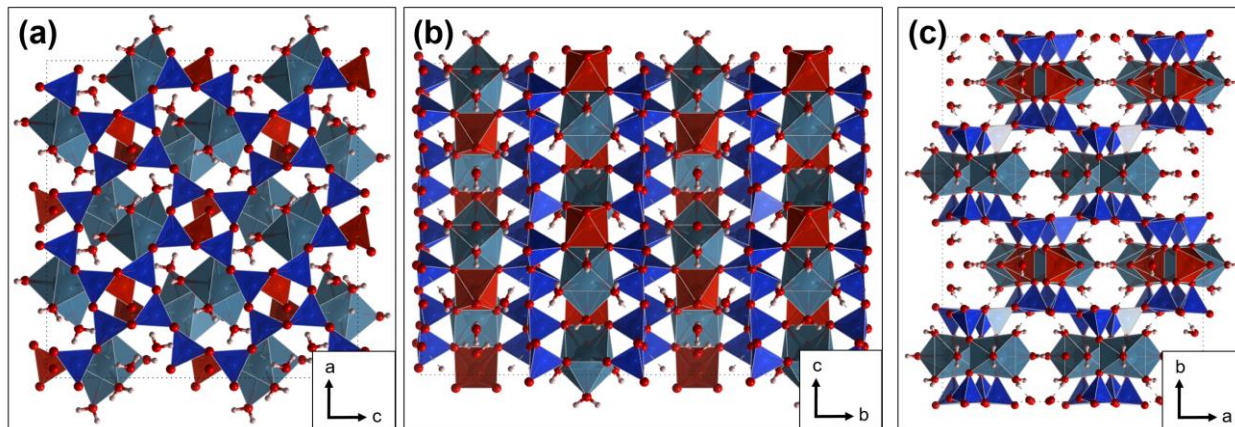
Figure 1. Polyhedral models of the cavansite crystal structure as viewed parallel to each of the major axial directions generated using VESTA. **(a)** cavansite structure viewed parallel to the b axis showing the 8- and 4-membered rings of silica tetrahedra; **(b)** cavansite structure viewed parallel to the a-axis showing the silica layers and the calcium-vanadium layers; **(c)** cavansite structure viewed parallel to the c-axis showing the largest set of channels in the structure (3.2 Å). Dark blue tetrahedra represent Si atoms, light blue polyhedral represent Ca atoms, red pyramids V atoms, red spheres represent O atoms, and white spheres represent H atoms (data used for rendering from Hughes et al. 2011.)
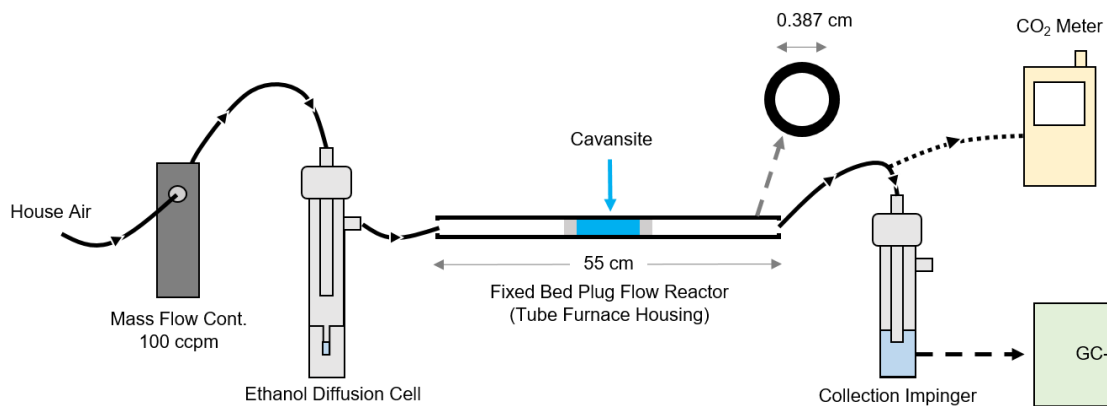
Figure 2. Schematic of the reactor set-up used in the gas-phase oxidation of ethanol experiments.
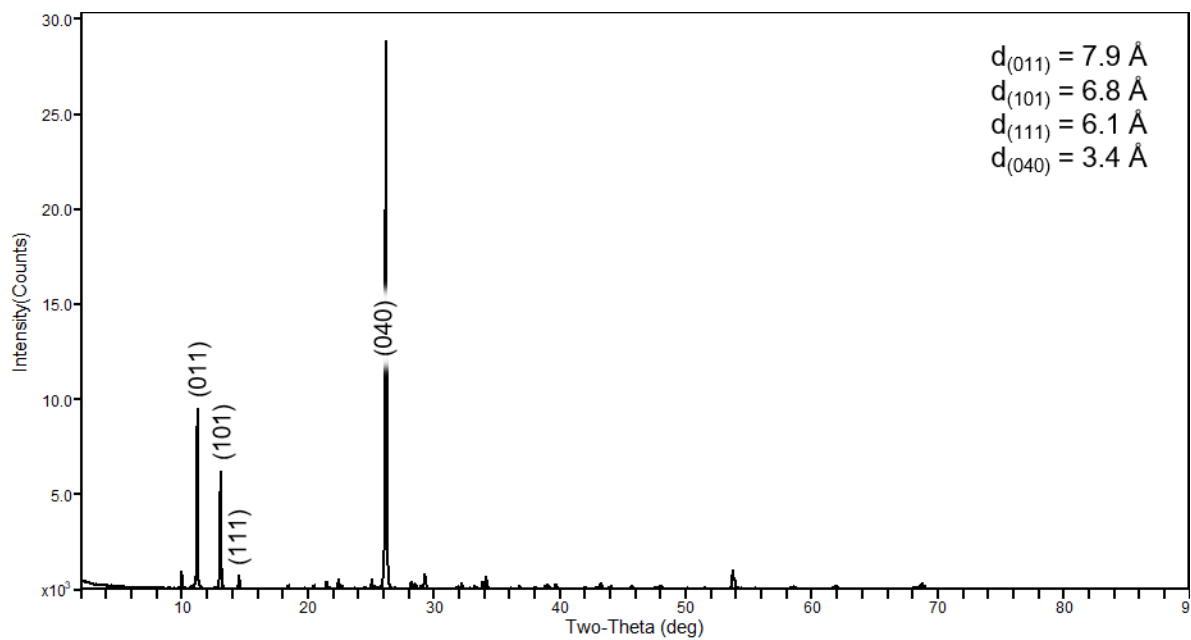
Figure 3. Powder X-ray diffraction pattern of cavansite with the Miller indices of major reflections identified and the d-spacing values for each reported in the upper right.
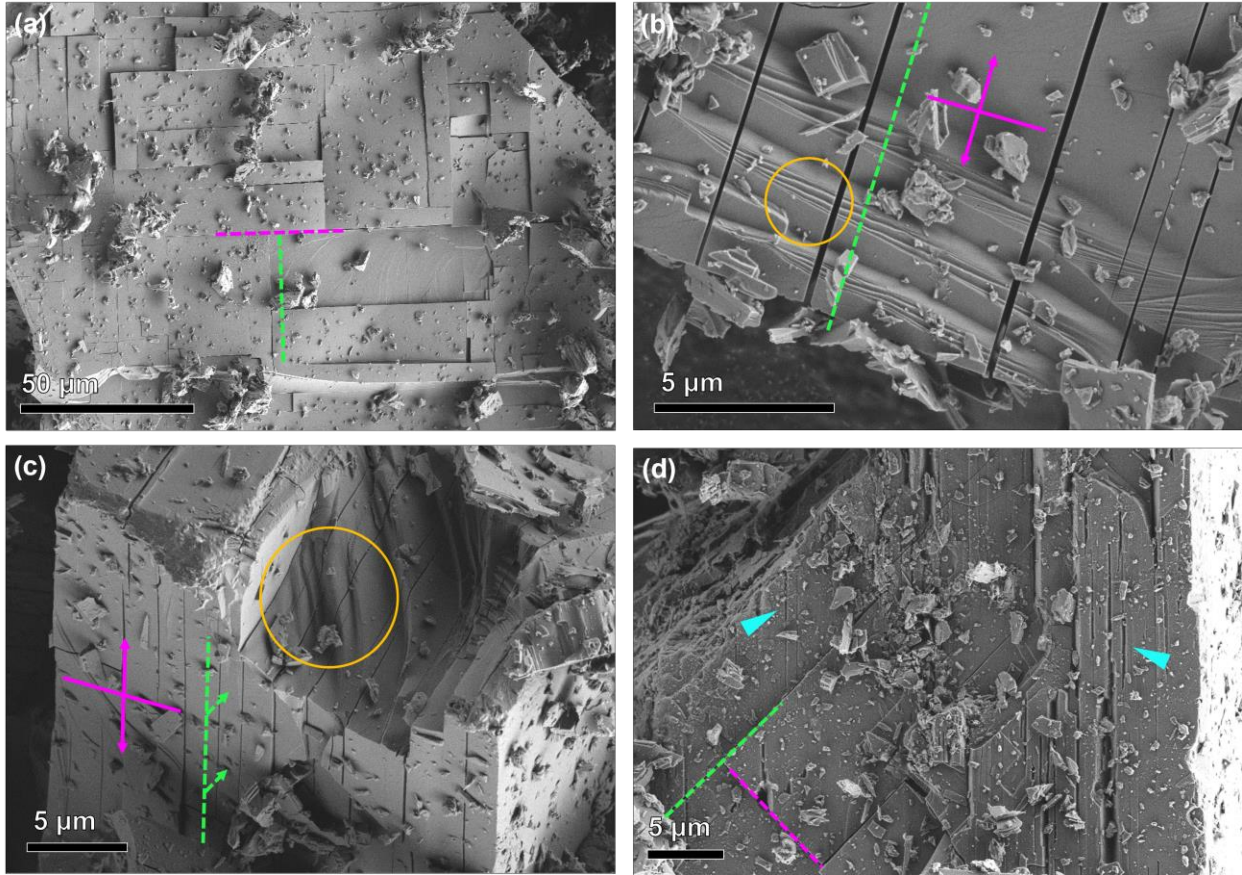
Figure 4. SEM micrographs of cavansite crystals in different orientations. **(a)** a cavansite crystal face perpendicular to the c-axis, showing the development of cleavage in two orthogonal directions indicated by pink and green dashed lines; **(b)** cavansite crystal oriented normal to one of the cleavage planes, indicated with pink solid lines, showing linear traces of another set of cleavage planes indicated by green dashed lines, as well as conchoidal fracture developing perpendicular to the cleavage planes indicated with yellow circle; **(c)** cavansite crystal showing all three planar directions; cleavage directions are indicated in green and pink and fracture development indicated with a yellow circle; **(d)** cavansite crystal showing linear etching features approximately 45° off the cleavage planes indicated with blue arrows.
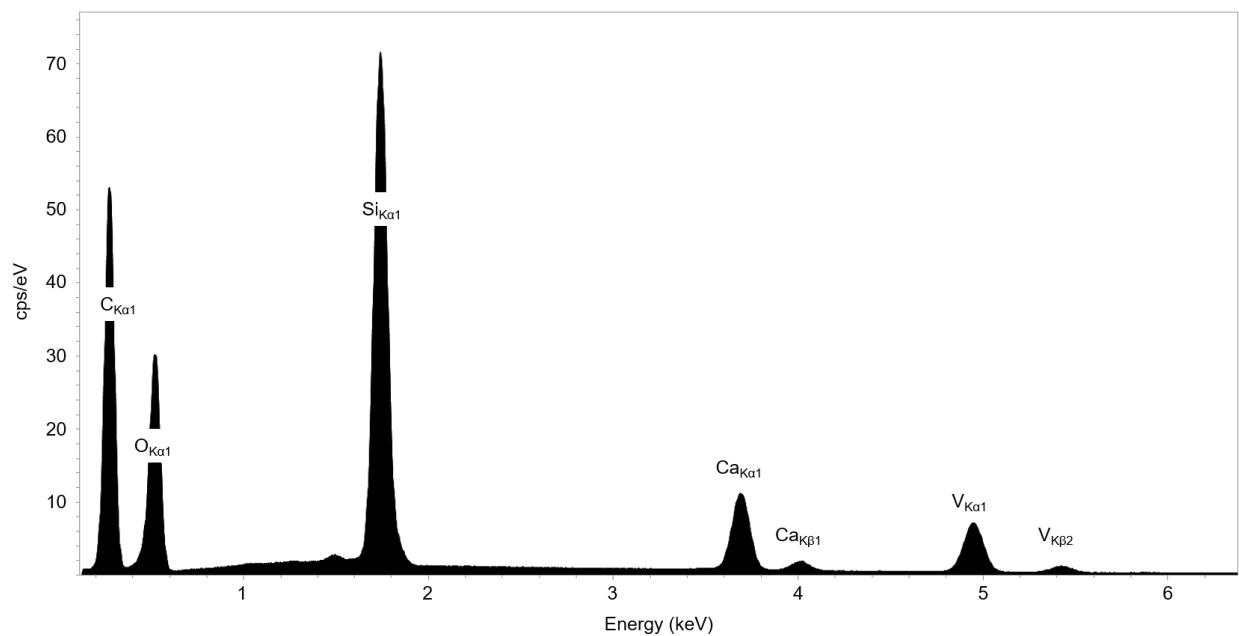
Figure 5. Energy dispersive spectrum of cavansite showing absence of impurities.
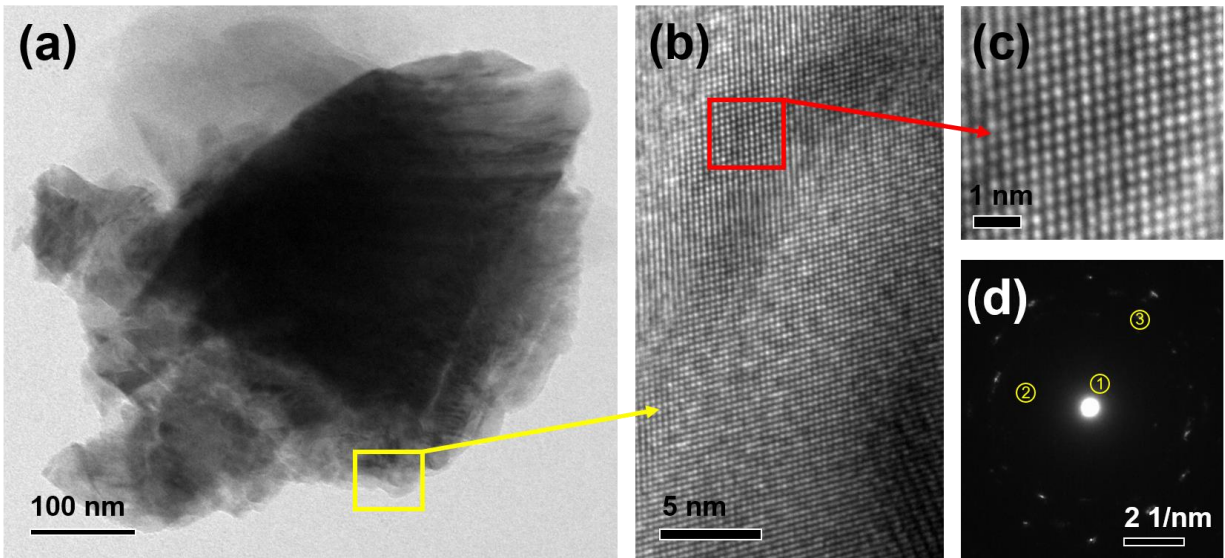
Figure 6. TEM-BF micrographs of an aggregate of cavansite crystals. **(a)** TEM brightfield image of the general texture of a cavansite crystal; **(b)** higher magnification image of region of (a) indicated in yellow showing atomic detail of cavansite; **(c)** blown-up image of region of (b) indicated in red showing finer scale details of the atoms (black) and channels (white) – interatomic distances and angular relationships indicate that the field of view is slightly off axis parallel to the c-direction with channels apparent 3.0 angstroms in diameter **(d)** SAED image of (b) with spot 1 = (020) = 6.1 Å, spot 2 = (200) = 4.5 Å, and spot 3 = (040) = 3.0 Å.
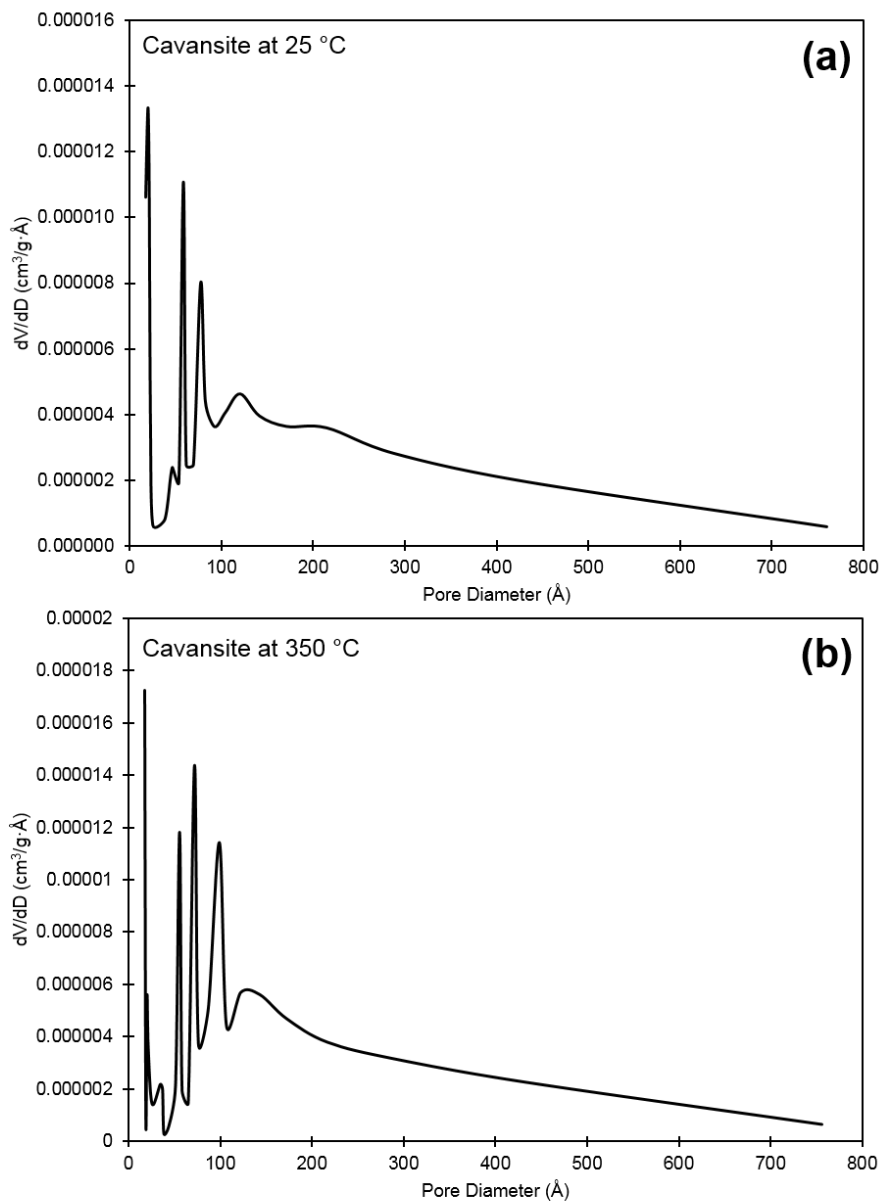
Figure 7. Pore size distribution curves as calculated from BJH adsorption dV/dD pore volumes for **(a)** cavansite at 25°C and **(b)** cavansite after heat treatment at 350 °C for one hour.
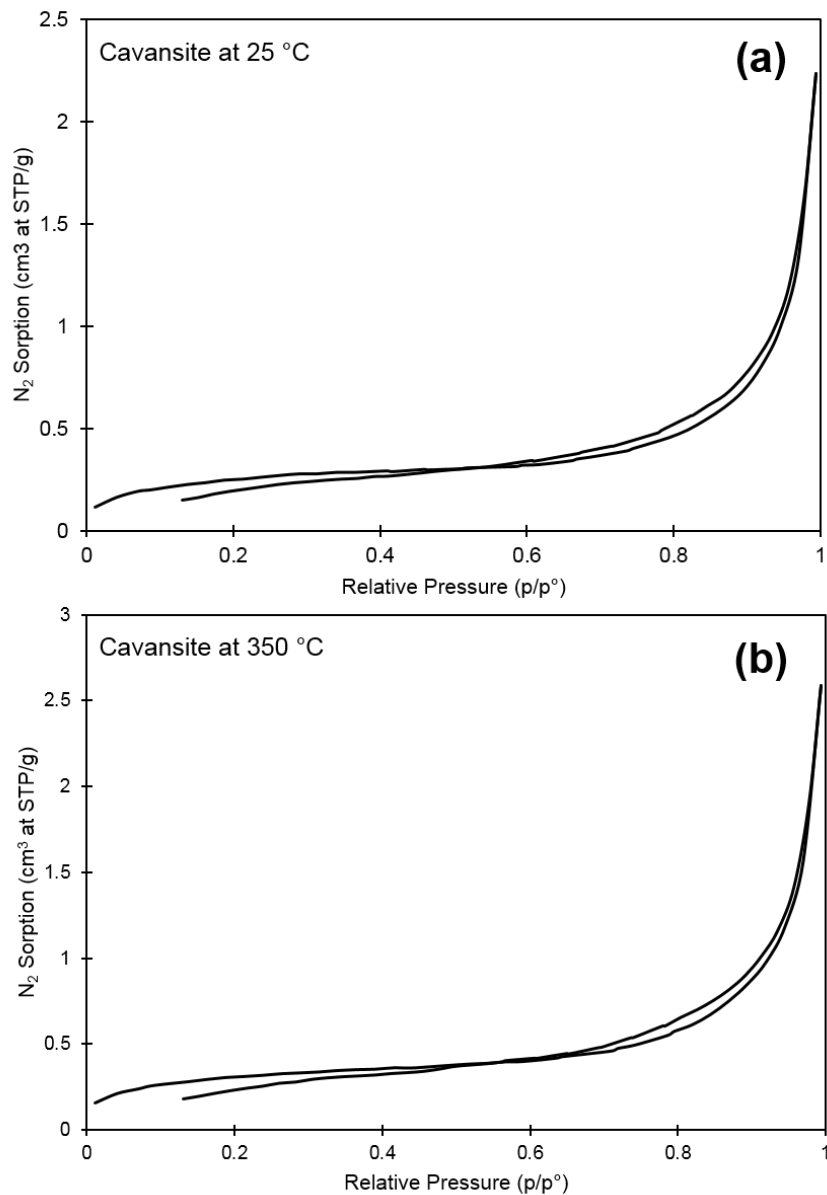
Figure 8. BJH Adsorption and desorption isotherms of cavansite, both of which are type III isotherms without hysteresis, indicating absence of bottle-necked pores. **(a)** Isotherm of cavansite at room temperature; **(b)** isotherm of cavansite after heat treatment at 350 °C for 1 hour.
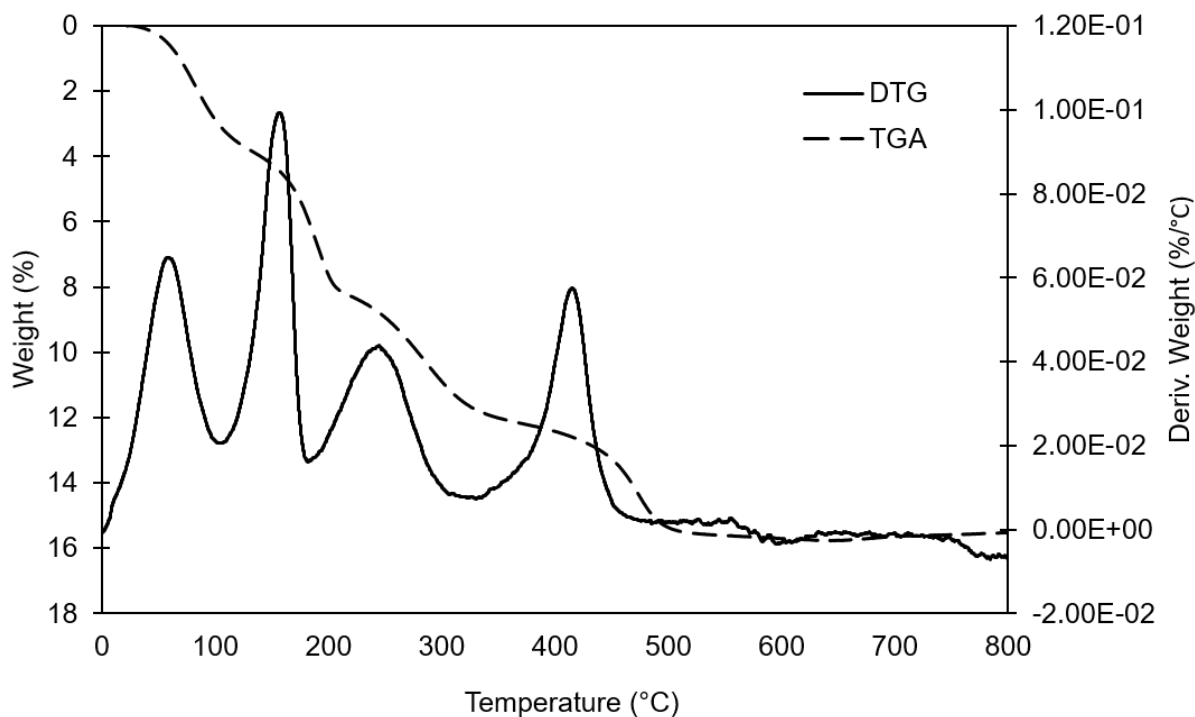
Figure 9. Thermogravimetric analysis and derivative thermogravimetry data of cavansite in the temperature range 0-800 °C. Cavansite has four distinct mass loss steps which correspond to sequential loss of three zeolitic water molecules and one structural water molecule. Loss of the final water molecule at approximately 400 °C results in loss of crystallinity and destruction of the cavansite structure. The small weight loss after 650 °C is a function of the oxidation of vanadium from tetravalent to pentavalent.
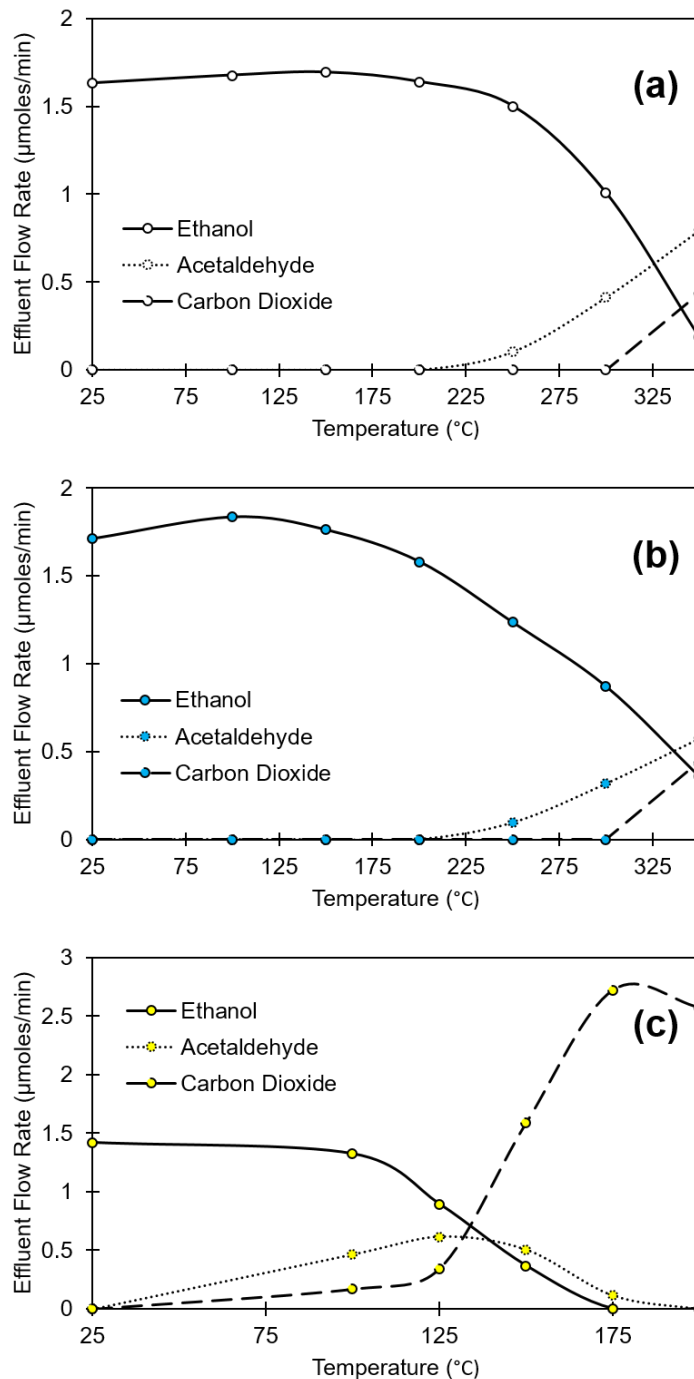
Figure 10. Flow diagrams for all ethanol oxidation runs performed in this study. **(a)** Effluent flow diagram of the quartz wool control run; **(b)** effluent flow diagram for the cavansite run; **(c)** effluent flow diagram for the cryptomelane run. Solid lines are ethanol, dotted lines are acetaldehyde, and long dashed lined are carbon dioxide.
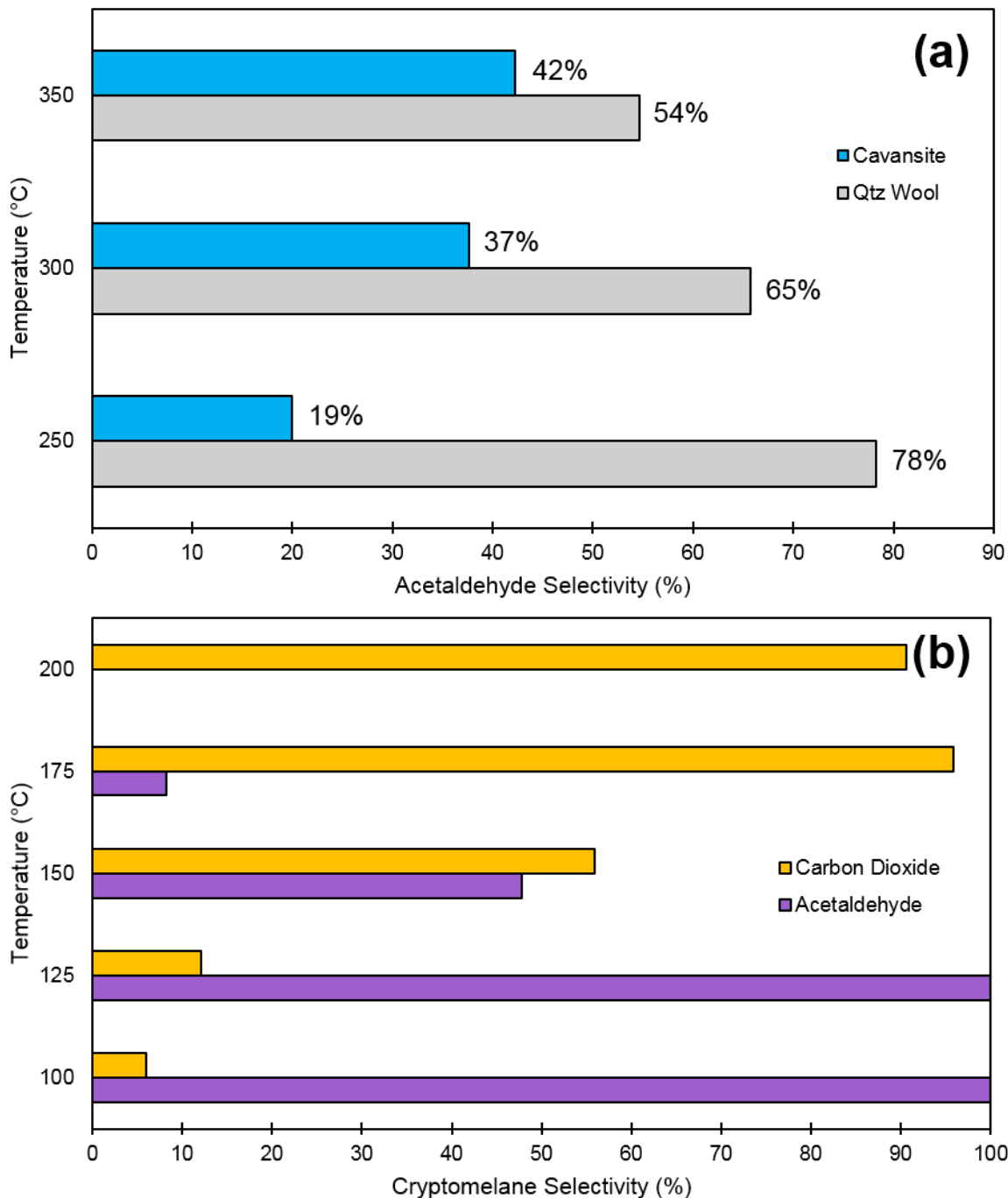
Figure 11. Selectivity graphs of the catalysts tested in this investigation. **(a)** Selectivity of acetaldehyde by quartz wool compared to cavansite showing that cavansite favors selective oxidation; **(b)** selectivity of carbon dioxide and acetaldehyde over cavansite showing that total oxidation is the favored reaction pathway.
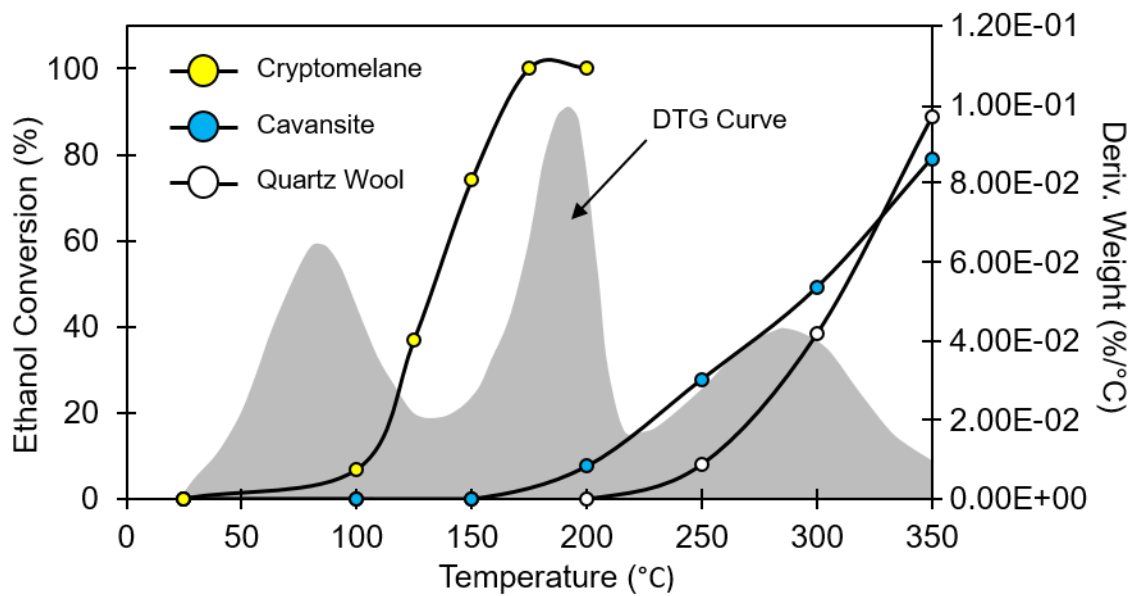
Figure 12. Light-off curves for each catalyst analyzed in this study with the DTG curve (Fig. 7) superimposed onto the data to relate activity to weight loss.
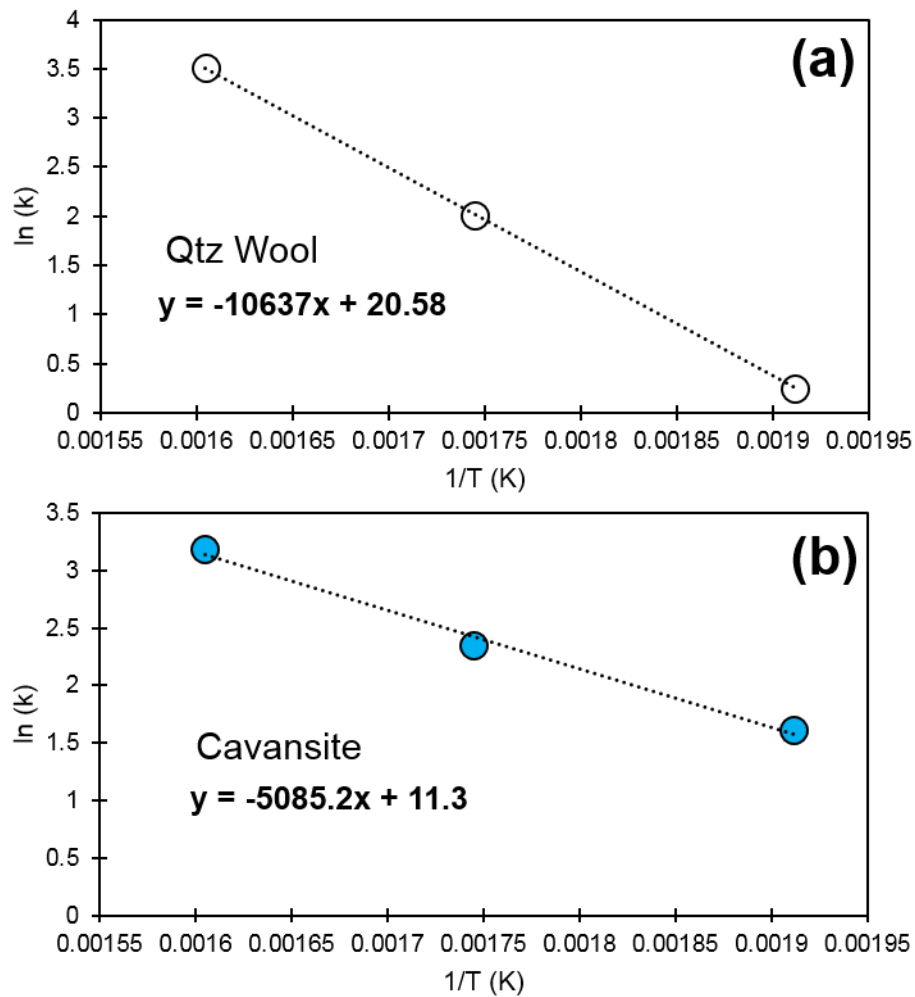
Figure 13. Plots of the natural log of the reaction rate constant (k) versus the reciprocal of the reaction rate temperature in Kelvin for temperatures 250, 300, and 350 °C; the equation of the trend line drawn between the points is displayed on the lower left, the slope of which is equal to (-E/R), used to calculate activation energy (E_a).

Table 1. Results of N_2 porosimetry experiments on cavansite at room temperature and after heat treating at 350 °C for one hour

Sample	BET Surface Area (m^2/g)	Cumulative Pore volume $(cm^3/g)^a$	Volume in macropores $(\%)^b$	Volume in mesopores $(\%)^c$	Volume in micropores $(\%)^d$
[1]Cavansite$_{25°C}$	0.90 ± 0.01	0.003	64.2	34.0	1.8
[2]Cavansite$_{25°C}$	0.90 ± 0.01	0.003	65.4	33.6	1.0
[1]Cavansite$_{350°C}$	1.08 ± 0.01	0.004	63.3	35.0	1.7
[2]Cavansite$_{350°C}$	1.08 ± 0.01	0.004	63.6	35.6	0.8

[1] First analysis

[2] Second analysis

[a] BJH adsorption cumulative pore volume of pores between 17 Å and 3000 Å

[b,c,d] Cumulative BJH adsorption; macropores = >500 Å, mesopores = 20-500 Å, micropores = <20 Å

Table 2: Results of thermogravimetric analysis of cavansite.

Weight Loss (% of initial mass)					
Temp < 100 °C	100 °C ≤ T ≤ 200 °C	200 °C ≤ T ≤ 300 °C	300 °C ≤ T ≤ 400 °C	Temp > 400 °C	Total Temp. < 800 °C
2.9	4.7	3.3	1.5	3.1	15.5

Table 3. Observed reaction rate at 250 °C of cavansite, activation energies, and T_{50} and T_{80} values for each sample.

Sample	Reaction rate (μmoles/min·g cat) at (inlet ethanol concentration)	Reaction rate (μmoles/min·m^2 cat) at (inlet ethanol concentration)	†E_a (kJ/mol)	T_{50} (K)	T_{80} (K)
Quartz Wool	-	-	88.4	583.15	613.15
Cavansite	18.1 (420 ppm)	20.1 (420 ppm)	42.3	573.15	623.15

† Calculated between 250 and 350 °C